Advances in Geochemical Testing of Key Contaminants in Residual Hanford Tank Waste

November 2005

The cover shows a scanning electron microscope image of aluminum (red) and iron (green) in a particle aggregate of residual waste from tank C-106 at the C Tank Farm on the Hanford Site. Cover design by S. B. Neely, Pacific Northwest National Laboratory.

This document was printed on recycled paper.

Advances in Geochemical Testing of Key Contaminants in Residual Hanford Tank Waste

W. J. Deutsch   H. T. Schaef
K. M. Krupka   S. M. Heald
K. J. Cantrell   B. W. Arey
C. F. Brown   R. K. Kukkadapu
M. Lindberg

November 2005

Pacific Northwest National Laboratory
Richland, Washington 99352

Summary

This report describes the advances that have been made over the past two years in testing and characterizing waste material in Hanford tanks. This waste is being studied because it will remain in the tanks after closure and represents a potential source of contamination to the environment. The development of a contaminant release model for the residual waste in a tank requires detailed knowledge of the composition of the waste and the phases (liquid and solids) in the waste that contain the contaminant. The contaminant release models developed for the tanks will be used as a component in the performance assessments for tank closures being conducted by CH2M HILL Hanford Group Inc. for the U.S. Department of Energy.

The primary contaminants in tank waste that are a long-term risk to groundwater are U, ^{99}Tc, ^{129}I, and Cr. Uranium is a major constituent of waste in many tanks, and its concentration can be readily measured; however, more than one U solid phase is generally present in the waste, and the identity and solubility of the minor minerals may be unknown and difficult to measure. Chromium is present at much lower concentrations than U and appears to rarely form minerals with Cr as a primary constituent. Most of the Cr is present as a trace constituent in other solids, which complicates developing a source term for this metal. Technetium-99 and ^{129}I are present in the waste at very low concentrations. If they form distinct minerals (such as TcO_2 or AgI), the amount of the mineral present is too low to detect with conventional methods. These contaminants may also be present as trace constituents in other solid phases where they are difficult to identify and quantify, and, therefore, develop a release model.

Advances are being made in testing and analytical methods to characterize tank waste material. In the past two years, these advances have been in the areas of inductively coupled plasma-mass spectrometry (ICP-MS) analysis of ^{129}I, ^{90}Sr, ^{237}Np, ^{239}Pu, and ^{241}Am; mapping of elements in waste material using scanning electron microscopy/energy dispersive spectroscopy (SEM/EDS); application of synchrotron x-ray analysis; and Mössbauer spectroscopic analysis. ICP-MS techniques have produced excellent results for solution analyses with much less complicated separations and analytical methods than conventional techniques. SEM/EDS mapping has provided a valuable tool to identify the association of elements in waste material solid phases. Synchrotron-based analyses have allowed for solid phase identification on a much smaller (micrometer) scale while also providing the ability to characterize the oxidation states and compositions of the solid phases. Mössbauer analysis has helped to determine the oxidation states of Fe in the minerals.

These advancements in techniques are being used to develop more defensible, mechanistic models of contaminant release from the residual waste material. Further advancements will be made as these methods are refined and additional methods are evaluated. Initial work has been started on testing a microwave digestion technique to quantify total metals concentrations in the material. An evaluation of the association of ^{99}Tc with Fe and Al oxide/hydroxide solids present in the waste material is being considered using single-solid phase analog systems that will not be as complex as the waste material.

Acknowledgments

Acronyms and Abbreviations

AEA	alpha energy analysis
AMU	atomic mass unit
BBI	Best Basis Inventory
BSE	backscattered electron
CCM	constant capacitance model
CH2M HILL	CH2M HILL Hanford Group, Inc.
DDLM	diffuse double layer model
DLM	diffuse layer model
DOE	U.S. Department of Energy
DRC	dynamic reaction cell
DWS	drinking water standard
EDS	energy dispersive spectroscopy
EDTA	ethylenediaminetetraacetic acid
EPA	U.S. Environmental Protection Agency
EQL	estimated quantitation limit
EDX	energy dispersive x-ray spectrometry or spectrometer
EXAFS	extended x-ray absorption fine structure
EPMA	electron probe microanalysis
HDW	Hanford Defined Waste
HEDTA	hydroxyethylethylenediaminetriacetic acid
HF	hydrofluoric
HFD	hyperfine field distribution
IC	ion chromatography
ICP-MS	inductively coupled plasma-mass spectroscopy (spectrometer)
ICP-OES	inductively coupled plasma-optical emission spectroscopy (same as ICP-AES)
ICDD	International Center for Diffraction Data, Newtown Square, Pennsylvania
JCPDS	Joint Committee on Powder Diffraction Standards
LEPS	low energy photon spectrometry
LSC	liquid scintillation counting
MCL	maximum contaminant level
MCS	multi-channel scalar
NEXAFS	near edge x-ray absorption fine structure
NIST	National Institute of Standards and Technology
NSERC	National Sciences and Engineering Research Council
NTA	nitrilotriacetic acid

PNC-CAT	Pacific Northwest Consortium Collaborative Access Team
PNNL	Pacific Northwest National Laboratory
QSD	quadrupole splitting distribution
RT	room temperature
SCM	surface complexation model
SEM	scanning electron microscopy (or microscope)
SRM	Standard Reference Material
TBP	tributyl phosphate
TEM	transmission electron microscopy (or microscope)
TLM	triple layer model
TRU	transuranic
TWINS	Tank Waste Information Network System
WDS	wavelength dispersive spectroscopy
XANES	x-ray absorption near edge structure
XAS	x-ray absorption spectroscopy
XPS	x-ray photoelectron spectroscopy
XRD	x-ray diffraction
μSXRF	microscanning x-ray fluorescence
μXRF	micro x-ray fluorescence
μXRD	micro x-ray diffraction

Contents

Figures

Tables

1.0   Introduction

The underground storage tanks at Hanford contain waste liquids and solids from the reprocessing of fuel rods from nuclear reactors to obtain plutonium. The U.S. Department of Energy (DOE) and its contractor CH2M HILL Hanford Group, Inc. (CH2M HILL) are closing these tanks by removing as much of the waste material as possible, then filling the tanks to prevent collapse, and covering them to minimize contact and infiltration of water. The residual waste that cannot be removed from the tanks represents a potential future risk to groundwater if infiltration mobilizes contaminants in the waste and transports them to the water table. Water leaching of contaminants from the waste is a response to geochemical inter-actions between the solution and the solids comprising the waste material. The leaching process is the release mechanism of contaminants to the environment after the Hanford tanks are closed. CH2M HILL is conducting the performance assessments for the closed tanks to evaluate whether they represent a long-term risk to the environment. Pacific Northwest National Laboratory (PNNL) is testing the residual waste and developing source release models to use in the performance assessments.

To estimate future leaching of contaminants from the tanks requires detailed knowledge of the types of solids present in the waste, their major and trace element composition, and their solubility in the tank environment. Developing this knowledge is a challenge because a wide variety of waste was added to the tanks over several decades, relatively unique elements (transuranics [TRUs], fission products) are included in the material, the highly radioactive nature of the waste makes it difficult to work with, and the tank chemical environment (high pH, temperature, and ionic strength) may have produced uncommon solid phases. Initial testing of the waste material used standard methods to measure total elemental concentration (acid extraction and fusion methods), mineralogy (x-ray diffraction [XRD]), and mineral composition and texture (scanning electron microscopy/energy dispersive spectroscopy [SEM/EDS]). The results of this work and the development of contaminant source terms have been documented for tanks AY-102, BX-101, C-203, C-204, and C-106 (Lindberg and Deutsch 2003; Deutsch et al. 2004, 2005; Krupka et al. 2004).

This initial work disclosed the need to develop additional methods of characterizing and testing the complex waste material. In the past year, the following methods and tools have been evaluated on tank waste samples and reference materials:

- Iodine-129 extraction methods and measurement using inductively coupled plasma-mass spectroscopy (ICP-MS)
- Strontium-90 and TRU element analysis using ICP-MS
- Element distribution mapping on solids using SEM/EDS
- Synchrotron-based x-ray analysis
- Mössbauer spectroscopic analysis

This report discusses the application of these techniques to the study of tank waste. Also provided in this report, is a discussion of the physical, chemical, and mineralogic characteristics of the Hanford tank waste, the geochemistry of the key contaminants of concern from a groundwater risk standpoint (^{238}U, ^{99}Tc, ^{129}I, and Cr), and ideas for continued advancement in the study of these materials to generate reliable source release models.

2.0   Tank Waste Characteristics

According to the Tank Waste Information Network System (TWINS) Best Basis Inventory (BBI) (as of 07/20/05), sludge is present in 135 of the 149 single-shell tanks (Table 1). Many of the tanks also contain large amounts of saltcake (primarily $NaNO_3$), which was produced by neutralizing nitric acid in the waste stream with NaOH. The majority of the saltcake is relatively soluble in water compared to the sludge, and most of the saltcake will likely be dissolved and removed from the tanks during retrieval operations. For this reason, the geochemical focus on residual tank waste to date has been on the less soluble sludge that will remain in the tanks after closure.

The current amount of pre-retrieval sludge in the tanks varies from less than 10,000 liters in 11 tanks to over 1,000,000 liters in 7 tanks. Tank T-111 is reported to have the largest amount of sludge at 1,691,000 liters. The physical, chemical, and solid phase makeup of this sludge are discussed in this section.

2.1   Physical Properties

TWINS provides a variety of information on physical properties of tank sludge. The data include volume, temperature, moisture content, density, and rheology (flow and deformation). Table 2 provides summary data on tank sludge densities and percent water content. Data on temperature and rheology must be obtained from each tank report available on the TWINS database.

Physical descriptions of the tank interior and solid material obtained from sampling are compiled in Tank Interpretive Reports that can be accessed through the TWINS. These reports include information on the color of the sludge from photographs of the tank interior and the colors of the solid material and presence of liquids and organic layers in collected sludge samples.

2.2   Chemical Composition

Sludge from two tanks (C-106 and C-203) has been retrieved at this time and the compositions of the residual waste are documented in TWINS. The compositions of the pre-retrieved sludge in the remaining tanks are available in TWINS and can be used as a rough approximation of the makeup of the residual material that will be left after retrieval. The composition of the sludge will likely change during retrieval because more soluble minerals and their constituents will be selectively removed from the sludge and the composition of the retrieval solution may add constituents of increase their concentration in the final waste.

TWINS provides an estimate of the volume of sludge in each single-shell tank separated into 32 waste types. Table 1 provides the data as of July 20, 2005. Thirty-two waste types are represented in the sludge. Table 3 describes each waste type. Most tanks contain only one or two waste types in the sludge, although a few tanks contain as many as four (S-107), five (C-104), or six (C-102) waste types. The BBI in TWINS for each tank provides as estimate of sludge chemical/radiological composition based on sampling results, engineering estimates, and/or Hanford Defined Waste Model estimates using the waste

Table 1. Best Basis Inventory in Single-Shell Tank Sludge Waste Types/Volumes Expressed in Thousands of Gallons (as of 7/20/2005)

Waste Type	241-A-101	241-A-103	241-A-104	241-A-105	241-A-106	241-AX-101	241-AX-102	241-AX-103	241-AX-104	241-B-101	241-B-103
1C (Solid)											
1CFeCN (Solid)											
224-1 (Solid)											
224-2 (Solid)											
2C (Solid)											
AR (Solid)		8	102		79						
B (Solid)							23			19	
BL (Solid)										76	
BL (Solids)											
CWP1 (Solid)											
CWP2 (Solid)											
CWR1 (Solid)											
CWR2 (Solid)											
CWZr1 (Solid)											
DE (Solid)											
HS (Solid)											
MW1 (Solid)										11	4
MW2 (Solid)											
NA											
OWW3 (Solid)											
P1 (Solid)			4								
P2 (Solid)	11			139				30	28		
PFeCN (Solid)											
Portland Cement (Solid)											
R1 (Solid)											
R2 (Solid)											
SRR (Solid)					110	11					
TBP (Solid)											
TFeCN (Solid)											
TH1 (Solid)											
TH2 (Solid)											
Z (Solid)											
	11	8	106	139	189	11	23	30	28	106	4

4

Table 1. (contd)

Waste Type	241-B-104	241-B-105	241-B-106	241-B-107	241-B-108	241-B-109	241-B-110	241-B-111	241-B-112	241-B-201	241-B-202
1C (Solid)	473	45	163	285							
1CFeCN (Solid)											
224-1 (Solid)										111	
224-2 (Solid)											108
2C (Solid)	697	61					914	809	56		
AR (Solid)											
B (Solid)							11	101			
BL (Solid)											
BL (Solids)											
CWP1 (Solid)											
CWP2 (Solid)				42	104	189					
CWR1 (Solid)											
CWR2 (Solid)											
CWZr1 (Solid)											
DE (Solid)											
HS (Solid)											
MW1 (Solid)											
MW2 (Solid)											
NA											
OWW3 (Solid)											
P1 (Solid)											
P2 (Solid)											
PFeCN (Solid)											
Portland Cement (Solid)											
R1 (Solid)											
R2 (Solid)											
SRR (Solid)											
TBP (Solid)			297								
TFeCN (Solid)											
TH1 (Solid)											
TH2 (Solid)											
Z (Solid)											
	1,170	106	460	327	104	189	925	910	56	111	108

Table 1. (contd)

Waste Type	241-B-203	241-B-204	241-BX-101	241-BX-102	241-BX-103	241-BX-104	241-BX-105	241-BX-106	241-BX-107	241-BX-108
1C (Solid)									1,313	38
1CFeCN (Solid)										
224-1 (Solid)										
224-2 (Solid)	188	184								
2C (Solid)										
AR (Solid)										
B (Solid)										
BL (Solid)										
BL (Solids)			74							
CWP1 (Solid)										
CWP2 (Solid)			47	81	214	51	96	18		
CWR1 (Solid)						110				
CWR2 (Solid)										
CWZr1 (Solid)										
DE (Solid)				147						
HS (Solid)										
MW1 (Solid)						155	9			
MW2 (Solid)										
NA										
OWW3 (Solid)										
P1 (Solid)										
P2 (Solid)										
PFeCN (Solid)										
Portland Cement (Solid)										
R1 (Solid)										
R2 (Solid)										
SRR (Solid)										
TBP (Solid)			59	70	21	53	55	20		81
TFeCN (Solid)										
TH1 (Solid)										
TH2 (Solid)										
Z (Solid)										
	188	184	180	298	235	369	160	38	1,313	119

Table 1. (contd)

Waste Type	241-BX-109	241-BX-110	241-BX-111	241-BX-112	241-BY-101	241-BY-103	241-BY-104	241-BY-105	241-BY-106	241-BY-107
1C (Solid)		151	121	617						
1CFeCN (Solid)										
224-1 (Solid)										
224-2 (Solid)										
2C (Solid)										
AR (Solid)										
B (Solid)										
BL (Solid)										
BL (Solids)										
CWP1 (Solid)										
CWP2 (Solid)							34			
CWR1 (Solid)										
CWR2 (Solid)										
CWZr1 (Solid)										
DE (Solid)										
HS (Solid)										
MW1 (Solid)										
MW2 (Solid)										
NA		94								
OWW3 (Solid)										
P1 (Solid)										
P2 (Solid)										
PFeCN (Solid)								172	151	120	58
Portland Cement (Solid)									30	
R1 (Solid)										
R2 (Solid)										
SRR (Solid)										
TBP (Solid)	730									
TFeCN (Solid)						140				
TH1 (Solid)										
TH2 (Solid)										
Z (Solid)										
	730	245	121	617	140	34	172	181	120	58

7

Table 1. (contd)

Waste Type	241-BY-108	241-BY-109	241-BY-110	241-BY-112	241-C-101	241-C-102	241-C-103	241-C-104	241-C-105	241-C-106
1C (Solid)										
1CFeCN (Solid)										
224-1 (Solid)										
224-2 (Solid)										
2C (Solid)										
AR (Solid)							108			
B (Solid)										
BL (Solid)										
BL (Solids)										
CWP1 (Solid)					208	125	163	326	450	
CWP2 (Solid)		89				855		229		
CWR1 (Solid)										
CWR2 (Solid)										
CWZr1 (Solid)						38		90		
DE (Solid)										
HS (Solid)										
MW1 (Solid)						19				
MW2 (Solid)				8						
NA								152		10.166
OWW3 (Solid)								103		
P1 (Solid)										
P2 (Solid)										
PFeCN (Solid)	151		162							
Portland Cement (Solid)										
R1 (Solid)										
R2 (Solid)										
SRR (Solid)										
TBP (Solid)					125	61			50	
TFeCN (Solid)										
TH1 (Solid)						98				
TH2 (Solid)								80		
Z (Solid)										
	151	89	162	8	333	1,196	271	980	500	10

Table 1. (contd)

Waste Type	241-C-107	241-C-108	241-C-109	241-C-110	241-C-111	241-C-112	241-C-201	241-C-202	241-C-203	241-C-204
1C (Solid)	507	110	38	670	49	57				
1CFeCN (Solid)										
224-1 (Solid)										
224-2 (Solid)										
2C (Solid)										
AR (Solid)										
B (Solid)										
BL (Solid)										
BL (Solids)										
CWP1 (Solid)			55		60	60				
CWP2 (Solid)	89									
CWR1 (Solid)										
CWR2 (Solid)										
CWZr1 (Solid)										
DE (Solid)										
HS (Solid)			26		17	4	2.2	5.03	0.476	6.4
MW1 (Solid)										
MW2 (Solid)										
NA										
OWW3 (Solid)										
P1 (Solid)										
P2 (Solid)										
PFeCN (Solid)										
Portland Cement (Solid)										
R1 (Solid)										
R2 (Solid)										
SRR (Solid)	339									
TBP (Solid)		95								
TFeCN (Solid)		45	121		91	272				
TH1 (Solid)										
TH2 (Solid)										
Z (Solid)										
	935	250	240	670	217	393	2	5	0.5	6

Table 1. (contd)

Waste Type	241-S-101	241-S-102	241-S-103	241-S-104	241-S-105	241-S-107	241-S-108	241-S-109	241-S-110	241-S-111	241-S-112
1C (Solid)											
1CFeCN (Solid)											
224-1 (Solid)											
224-2 (Solid)											
2C (Solid)											
AR (Solid)											
B (Solid)											
BL (Solid)											
BL (Solids)											
CWP1 (Solid)											
CWP2 (Solid)											
CWR1 (Solid)				91		447			76	38	
CWR2 (Solid)						211					
CWZr1 (Solid)						91					
DE (Solid)											
HS (Solid)											
MW1 (Solid)											
MW2 (Solid)											
NA	890										
OWW3 (Solid)											
P1 (Solid)											
P2 (Solid)											
PFeCN (Solid)											
Portland Cement (Solid)											
R1 (Solid)		71	34	409	8	462	19	49	288	207	23
R2 (Solid)											
SRR (Solid)											
TBP (Solid)											
TFeCN (Solid)											
TH1 (Solid)											
TH2 (Solid)											
Z (Solid)											
	890	71	34	500	8	1,211	19	49	364	245	23

Table 1. (contd)

Waste Type	241-SX-101	241-SX-102	241-SX-103	241-SX-104	241-SX-105	241-SX-107	241-SX-108	241-SX-109	241-SX-110	241-SX-111
1C (Solid)										
1CFeCN (Solid)										
224-1 (Solid)										
224-2 (Solid)										
2C (Solid)										
AR (Solid)										
B (Solid)										
BL (Solid)										
BL (Solids)										
CWP1 (Solid)										
CWP2 (Solid)										
CWR1 (Solid)										
CWR2 (Solid)										
CWZr1 (Solid)										
DE (Solid)										
HS (Solid)										
MW1 (Solid)										
MW2 (Solid)										
NA										
OWW3 (Solid)										
P1 (Solid)										
P2 (Solid)										
PFeCN (Solid)										
Portland Cement (Solid)										
R1 (Solid)	545	209	294	515	189	239	186	170		164
R2 (Solid)					49	117	94	81	184	205
SRR (Solid)										
TBP (Solid)										
TFeCN (Solid)										
TH1 (Solid)										
TH2 (Solid)										
Z (Solid)										
	545	209	294	515	238	356	280	251	184	369

11

Table 1. (contd)

Waste Type	241-SX-112	241-SX-113	241-SX-114	241-SX-115	241-T-101	241-T-102	241-T-103	241-T-104	241-T-105	241-T-106
1C (Solid)								1199	9	38
1CFeCN (Solid)										
224-1 (Solid)										
224-2 (Solid)										
2C (Solid)									273	
AR (Solid)										
B (Solid)										
BL (Solid)										
BL (Solids)										
CWP1 (Solid)										
CWP2 (Solid)						64	64			
CWR1 (Solid)							19		89	34
CWR2 (Solid)					140					10
CWZr1 (Solid)										
DE (Solid)		64								
HS (Solid)										
MW1 (Solid)										
MW2 (Solid)						8	4			
NA										
OWW3 (Solid)										
P1 (Solid)										
P2 (Solid)										
PFeCN (Solid)										
Portland Cement (Solid)										
R1 (Solid)	144	8	298							
R2 (Solid)	139		180	16						
SRR (Solid)										
TBP (Solid)										
TFeCN (Solid)										
TH1 (Solid)										
TH2 (Solid)										
Z (Solid)										
	283	72	478	16	140	72	87	1,199	371	82

12

Table 1. (contd)

Waste Type	241-T-107	241-T-108	241-T-110	241-T-111	241-T-112	241-T-201	241-T-202	241-T-203	241-T-204	241-TX-101	241-TX-102
1C (Solid)	559	20									
1CFeCN (Solid)											
224-1 (Solid)						107					
224-2 (Solid)			37	904	91		77	136	136		
2C (Solid)			1360	787	135						
AR (Solid)											
B (Solid)											
BL (Solid)											
BL (Solids)											
CWP1 (Solid)											
CWP2 (Solid)	32										
CWR1 (Solid)											
CWR2 (Solid)											
CWZr1 (Solid)											
DE (Solid)											
HS (Solid)											
MW1 (Solid)											
MW2 (Solid)										11	8
NA											
OWW3 (Solid)											
P1 (Solid)											
P2 (Solid)											
PFeCN (Solid)											
Portland Cement (Solid)											
R1 (Solid)										265	
R2 (Solid)											
SRR (Solid)											
TBP (Solid)	64										
TFeCN (Solid)											
TH1 (Solid)											
TH2 (Solid)											
Z (Solid)										4	
	655	20	1,397	1,691	226	107	77	136	136	280	8

Table 1. (contd)

Waste Type	241-TX-104	241-TX-105	241-TX-106	241-TX-108	241-TX-109	241-TX-110	241-TX-111	241-TX-113	241-TX-114	241-TX-115
1C (Solid)					1,375	140	163	351	15	
1CFeCN (Solid)										
224-1 (Solid)										
224-2 (Solid)										
2C (Solid)										
AR (Solid)										
B (Solid)										
BL (Solid)										
BL (Solids)										
CWP1 (Solid)										
CWP2 (Solid)										
CWR1 (Solid)										
CWR2 (Solid)										
CWZr1 (Solid)										
DE (Solid)										
HS (Solid)										
MW1 (Solid)										
MW2 (Solid)		31	4	8						
NA										
OWW3 (Solid)										
P1 (Solid)										
P2 (Solid)										
PFeCN (Solid)										
Portland Cement (Solid)										
R1 (Solid)	130		15							
R2 (Solid)										
SRR (Solid)										
TBP (Solid)				15						30
TFeCN (Solid)										
TH1 (Solid)										
TH2 (Solid)										
Z (Solid)										
	130	31	19	23	1,375	140	163	351	15	30

14

Table 1. (contd)

Waste Type	241-TX-116	241-TX-117	241-TY-101	241-TY-103	241-TY-104	241-TY-105	241-TY-106	241-U-101
1C (Solid)								
1CFeCN (Solid)			273	170	114			
224-1 (Solid)								
224-2 (Solid)								
2C (Solid)								
AR (Solid)								
B (Solid)								
BL (Solid)								
BL (Solids)								
CWP1 (Solid)								
CWP2 (Solid)								
CWR1 (Solid)								
CWR2 (Solid)								
CWZr1 (Solid)								
DE (Solid)	248	110					47	
HS (Solid)								
MW1 (Solid)								
MW2 (Solid)								
NA								
OWW3 (Solid)								
P1 (Solid)								
P2 (Solid)								
PFeCN (Solid)								
Portland Cement (Solid)								
R1 (Solid)								87
R2 (Solid)								
SRR (Solid)								
TBP (Solid)				220	49	874	15	
TFeCN (Solid)								
TH1 (Solid)								
TH2 (Solid)								
Z (Solid)								
	248	110	273	390	163	874	62	87

15

Table 1. (contd)

Waste Type	241-U-102	241-U-103	241-U-104	241-U-105	241-U-107	241-U-108	241-U-109	241-U-110
1C (Solid)								120
1CFeCN (Solid)								
224-1 (Solid)								
224-2 (Solid)								
2C (Solid)								
AR (Solid)								
B (Solid)								
BL (Solid)								
BL (Solids)								
CWP1 (Solid)								
CWP2 (Solid)								
CWR1 (Solid)				121	57		103	149
CWR2 (Solid)						110		
CWZr1 (Solid)								
DE (Solid)			311					
HS (Solid)								
MW1 (Solid)								
MW2 (Solid)								
NA								
OWW3 (Solid)								
P1 (Solid)								
P2 (Solid)								
PFeCN (Solid)								
Portland Cement (Solid)								
R1 (Solid)	163	42	151					396
R2 (Solid)								
SRR (Solid)								
TBP (Solid)								
TFeCN (Solid)								
TH1 (Solid)								
TH2 (Solid)								
Z (Solid)								
	163	42	462	121	57	110	103	665

Table 1. (contd)

Waste Type	241-U-111	241-U-112	241-U-202	241-U-203	241-U-204	Sum
1C (Solid)	49	47				8,722
1CFeCN (Solid)						557
224-1 (Solid)						218
224-2 (Solid)						1,861
2C (Solid)						5,092
AR (Solid)						297
B (Solid)						154
BL (Solid)						76
BL (Solids)						74
CWP1 (Solid)						1,447
CWP2 (Solid)						2,298
CWR1 (Solid)		58	10	9	7	1,418
CWR2 (Solid)						471
CWZr1 (Solid)						219
DE (Solid)						927
HS (Solid)						61
MW1 (Solid)						198
MW2 (Solid)						82
NA						1,146
OWW3 (Solid)						103
P1 (Solid)						4
P2 (Solid)						208
PFeCN (Solid)						814
Portland Cement (Solid)						30
R1 (Solid)	49	67				5,896
R2 (Solid)						1,065
SRR (Solid)						460
TBP (Solid)						2,984
TFeCN (Solid)						669
TH1 (Solid)						98
TH2 (Solid)						80
Z (Solid)						4
	98	172	10	9	7	

Table 2. Tank Sludge Densities and Percent Water

Tank Name	Density (g/mL)	Wt% Water	Tank Name	Density (g/mL)	Wt% Water
241-A-101	1.36	9.1	241-B-109	1.85	36.2
241-A-103	1.34	68.6	241-B-110	1.36	58.3
241-A-104	1.64	0	241-B-110	1.36	58.3
241-A-104	1.64	0	241-B-111	1.27	63.1
241-A-105	1.54	0	241-B-111	1.27	63.1
241-A-106	1.7	34.3	241-B-112	1.49	40.2
241-A-106	1.7	34.3	241-B-201	1.26	64.2
241-AN-106	1.52	37	241-B-202	1.22	75.9
241-AN-106	1.62	26.5	241-B-203	1.19	75.7
241-AP-102	1.75	31.1	241-B-204	1.19	77.3
241-AW-102	1.32	33.4	241-BX-101	1.68	15.5
241-AW-103	1.47	55.8	241-BX-101	1.68	15.5
241-AW-104	1.28	65.8	241-BX-101	1.68	15.5
241-AW-105	1.47	49.7	241-BX-102	1.68	40.9
241-AW-105	1.41	37.8	241-BX-102	0.384	
241-AX-101	1.51	62.2	241-BX-102	1.47	50.5
241-AX-102	1.57	42.5	241-BX-103	1.47	49.6
241-AX-103	1.61	44.2	241-BX-103	1.68	49.6
241-AX-104	1.8	8.23	241-BX-104	1.68	26.9
241-AY-101	1.78	35.1	241-BX-104	1.68	26.9
241-AY-102	1.65	39.5	241-BX-104	1.68	26.9
241-AY-102	1.65	39.5	241-BX-104	1.68	26.9
241-AZ-101	1.61	34.3	241-BX-105	1.69	12.6
241-AZ-101	1.61	34.3	241-BX-105	1.8	43.8
241-AZ-102	1.41	54.8	241-BX-105	1.69	12.6
241-AZ-102	1.41	54.8	241-BX-106	1.64	38.7
241-AZ-102	1.41	54.8	241-BX-106	1.64	38.7
241-AZ-102	1.41	54.8	241-BX-107	1.44	50.5
241-B-101	1.48	32	241-BX-108	1.43	17.2
241-B-101	1.48	32	241-BX-108	1.47	17.2
241-B-101	1.48	32	241-BX-109	1.52	50.6
241-B-103	1.8	43.8	241-BX-110	1.79	36.6
241-B-104	1.39	46.7	241-BX-110	1.43	54.1
241-B-104	1.39	46.7	241-BX-111	1.43	54.1
241-B-105	1.28	66.6	241-BX-112	1.31	63.3
241-B-105	1.43	54.1	241-BY-101	1.6	46.8
241-B-106	1.36	61.6	241-BY-103	1.68	40.9
241-B-106	1.42	56.8	241-BY-104	1.64	29
241-B-107	1.63	42.1	241-BY-105	1.68	25.5
241-B-107	1.68	5.78	241-BY-105	1.9	8
241-B-108	1.8	27.1	241-BY-106	1.68	37.3

Table 2. (contd)

Tank Name	Density (g/mL)	Wt% Water	Tank Name	Density (g/mL)	Wt% Water
241-BY-107	1.78	37.6	241-C-112	1.6	51.5
241-BY-108	1.53	31	241-C-112	1.6	51.5
241-BY-109	2	28.4	241-C-201	1.44	13.8
241-BY-110	1.82	28.7	241-C-202	1.44	16.2
241-BY-112	1.85	41.4	241-C-203	1.62	26.5
241-C-101	1.78	23.4	241-C-204	1.62	41.2
241-C-101	1.78	23.4	241-S-101	1.7	37.5
241-C-102	1.8	43.8	241-S-102	1.88	22.2
241-C-102	1.47	50.5	241-S-103	1.77	22.7
241-C-102	1.63	33.4	241-S-104	1.77	33.5
241-C-102	1.32	63.5	241-S-104	1.8	33.5
241-C-102	1.74	65.3	241-S-105	1.77	22.7
241-C-102	1.74	40.9	241-S-107	1.8	33
241-C-103	1.63	57.8	241-S-107	1.8	33
241-C-103	1.54	61.1	241-S-107	1.8	33
241-C-104	1.68	47.9	241-S-107	1.8	33
241-C-104	1.68	47.9	241-S-108	1.77	22.7
241-C-104	1.68	47.9	241-S-109	1.77	22.7
241-C-104	1.68	47.9	241-S-110	1.77	31.5
241-C-104	1.68	47.9	241-S-110	1.77	31.5
241-C-105	1.55	25.8	241-S-111	1.67	19.4
241-C-105	1.55	50.5	241-S-111	1.67	19.4
241-C-106	1.56	41.9	241-S-112	1.77	22.7
241-C-107	1.55	47.5	241-SX-101	1.69	25.6
241-C-107	1.55	47.5	241-SX-102	1.72	38.52
241-C-107	1.55	47.5	241-SX-103	1.88	21.9
241-C-108	1.48	38.2	241-SX-104	1.77	22.7
241-C-108	1.48	38.2	241-SX-105	1.67	22.7
241-C-108	1.48	38.2	241-SX-105	1.67	22.7
241-C-109	1.57	36.1	241-SX-107	1.77	22.7
241-C-109	1.57	36.1	241-SX-107	1.77	22.7
241-C-109	1.57	36.1	241-SX-108	1.77	2.03
241-C-109	1.43	54.1	241-SX-108	1.77	2.03
241-C-110	1.34	60.2	241-SX-109	1.77	22.7
241-C-111	1.58	31.4	241-SX-109	1.77	22.7
241-C-111	1.58	31.4	241-SX-110	1.77	22.7
241-C-111	1.58	31.4	241-SX-111	1.77	22.7
241-C-111	1.43	54.1	241-SX-111	1.77	22.7
241-C-112	1.6	51.5	241-SX-112	1.77	22.7
241-C-112	1.6	51.5	241-SX-112	1.77	22.7
			241-SX-113	1.09	46

Table 2. (contd)

Tank Name	Density (g/mL)	Wt% Water	Tank Name	Density (g/mL)	Wt% Water
241-SX-113	1.09	46	241-TX-108	1.85	41.4
241-SX-114	1.77	22.7	241-TX-108	1.47	50.5
241-SX-114	1.77	22.7	241-TX-109	1.43	54.1
241-SX-115	1.77	10.1	241-TX-110	1.43	54.1
241-SY-102	1.65	41.3	241-TX-111	1.43	54.1
241-SY-102	1.65	41.3	241-TX-113	1.43	54.1
241-T-101	1.46	51.7	241-TX-114	1.43	54.1
241-T-102	1.79	28.075	241-TX-115	1.47	50.5
241-T-102	1.85	41.4	241-TX-116	1.6	38.8
241-T-103	1.8	24.5	241-TX-117	0.384	
241-T-103	1.68	40.9	241-TY-101	1.64	43.5
241-T-103	1.85	41.4	241-TY-103	1.7	51.9
241-T-104	1.29	70.525	241-TY-103	1.7	51.9
241-T-105	1.51	53.5	241-TY-104	1.65	51.9
241-T-105	1.32	61.8	241-TY-104	1.65	51.9
241-T-105	1.32	61.8	241-TY-105	1.53	39.4
241-T-106	1.43	16.7	241-TY-106	1.4	38.1
241-T-106	1.8	16.7	241-TY-106	1.4	38.1
241-T-106	1.46	16.7	241-U-101	1.77	29.8
241-T-107	1.56	45.7	241-U-102	1.77	22.7
241-T-107	1.56	45.7	241-U-103	1.9	47.4
241-T-107	1.56	45.7	241-U-104	1.77	22.7
241-T-108	1.43	54.1	241-U-104	1.26	50.7
241-T-110	1.25	75.5	241-U-105	1.7	22.4
241-T-110	1.25	75.5	241-U-107	1.8	24.5
241-T-111	1.24	75.3	241-U-108	1.46	51.7
241-T-111	1.24	75.3	241-U-109	1.71	22.7
241-T-112	1.28	73.9	241-U-110	1.8	3.08
241-T-112	1.28	73.9	241-U-110	1.77	38.8
241-T-201	1.31	67.5	241-U-110	1.43	39.7
241-T-202	1.18	75.8	241-U-111	1.77	22.7
241-T-203	1.22	76.2	241-U-111	1.43	54.1
241-T-204	1.18	75	241-U-112	1.86	26
241-TX-101	1.77	22.7	241-U-112	1.43	54.1
241-TX-101	1.85	41.4	241-U-112	1.86	26
241-TX-101	1.76	29.1	241-U-201	1.63	27.1
241-TX-102	1.85	41.4	241-U-202	1.51	27.8
241-TX-104	1.89	44.6	241-U-203	1.59	40.2
241-TX-105	1.85	41.4	241-U-204	1.47	26.2
241-TX-106	1.85	41.4	244-BX	1.68	40.9
241-TX-106	1.77	22.7	244-TX	1.11	88.9

Table 3. Tank Sludge Waste Type Definitions

Waste Type	Definition
1C (Solid)	BiPO$_4$ first cycle decontamination waste and coating waste
1CFeCN (Solid)	Ferrocyanide sludge from in-plant scavenging of T Plant 1C waste (without coating waste)
224-1 (Solid)	Lanthanide fluoride process 224 Building waste (1949-1956)
224-2 (Solid)	Lanthanide fluoride process 224 Building waste (1944-1948)
2C (Solid)	BiPO$_4$ second cycle decontamination waste and coating waste
AR (Solid)	Water-washed PUREX sludge entrained in decants of recovered sludge or the water washes of this sludge and the solids remaining after acidification (1967-1976)
B (Solid)	B Plant high-activity waste - rare earth fission products, recovered current acid waste (CAW), solvent wash waste (1963-1972)
BL (Solid)	B Plant low-activity waste - insoluble solids remaining after treatment of solids centrifuged from CAW feed (i.e., acid leached and water washed PUREX high-level waste sludge)
CWP1 (Solid)	PUREX cladding waste, aluminum clad fuel (1956-1960)
CWP2 (Solid)	PUREX cladding waste, aluminum clad fuel (1961-1972)
CWR1 (Solid)	REDOX cladding waste, aluminum clad fuel (1952-1960)
CWR2 (Solid)	REDOX cladding waste, aluminum clad fuel (1961-1966)
CWZr1 (Solid)	PUREX zirconium cladding waste (1983-1989)
DE (Solid)	Diatomaceous earth
HS (Solid)	Hot Semiworks strontium and rare earth purification waste (1961-1968)
MW1 (Solid)	BiPO$_4$ Metal Waste (1944-1949)
MW2 (Solid)	BiPO$_4$ Metal Waste (1950-1956)
NA	
OWW3 (Solid)	PUREX organic wash waste (1968-1972)
P1 (Solid)	PUREX high-level waste (1963-1967)
P2 (Solid)	PUREX high-level waste (1956-1962)
PFeCN (Solid)	Ferrocyanide sludge from TBP in-plant scavenged supernatant and co-disposed TBP sludge
Portland Cement (Solid)	
R1 (Solid)	REDOX high-level waste (1952-1958)
R2 (Solid)	REDOX high-level waste (1959-1966)
SRR (Solid)	High-activity waste from B Plant processing of PUREX acidified sludge (PAS), solids centrifuged from AR vault feed, strontium purification waste after solvent extraction (SX), rare earth carrier precipitation (RE) or ion exchange (IX) rework, and other solutions containing activity (including cask station receipts, cell drainage containing product spills, WESF returns unsuitable for rework and crude RE disposal) (1969-1985)
TBP (Solid)	Tributyl phosphate process waste (1952-1957)
TFeCN (Solid)	Ferrocyanide sludge from supernatant scavenging in 244-CR Vault (1955-1958)
TH1 (Solid)	Thoria process waste (1970)
TH2 (Solid)	Thoria process waste (1966)
Z (Solid)	Plutonium Finishing Plant waste (1974-1988)

types and volumes (Place et al. 2004). The ability of the BBI to serve as an estimator of residual tank waste composition can be evaluated as tanks are retrieved. The pre-retrieval BBI estimate of tank sludge composition can be compared to post-retrieval composition. Depending on the type of retrieval (wet versus dry, acid versus neutral, etc.), the BBI values may provide a good estimate of contaminant sludge concentrations. As more is learned about the mineralogy and solid phase composition of the tank waste (discussed below), and if a correlation can be established between chemical composition and mineral occurrence, it may be possible to use the BBI to bound future release rate estimates of contaminants from closed tanks.

2.3   Solid Phases

The release of the contaminants of concern from the sludge is controlled by the chemical interaction between the solid phases comprising the sludge and the water contacting the sludge. The mineralogy of the sludge plays a key role in contaminant release because mineral solubility limits the extent to which contaminants are released to solution and adsorption of contaminants onto mineral surfaces affects the rate of movement of the contaminant in solution relative to the velocity of water flow. For these reasons, knowledge of the solids in the tank sludge is necessary to estimate the release of contaminants from the residual tank solids.

Rapko and Lumetta (2000) summarize the available published results obtained through FY 1999 for the major solid phases identified in Hanford tank sludge. Their summary for both single-shell and double-shell tanks is included in Table 4 along with newer data from Bechtold et al. (2003), Krupka et al. (2004), and Deutsch et al. (2004, 2005). The most commonly reported solid phases grouped by element with number of times reported are:

- U – β-U_3O_8 (3); $Na_4(UO_2)(CO_3)_3$ (čejkaite) (2); $Na[(UO_2)O(OH)](H_2O)_{0-1}$ (clarkeite) (1); UO_2 or U_3O_7 (1); $Na_2U_2O_7$ (1); $UO_3 \cdot H_2O$ (1); CaU_2O_7 (1); UO_3 (1)

- Cr – $Bi_{38}CrO_{60}$ (1); $Fe(Fe,Cr)_2O_4$ (donathite)(1); $Cr(OH)_3$ (am) (1)

- Fe – $FeO(OH)$ (5); Fe_2O_3 (hematite) (3); $Fe_2Bi(SiO_4)_2(OH)$ (2); $Fe(OH)_3$ (am) (2); $Bi/FePO_4$ (1); $Fe(Fe,Cr)_2O_4$ (donathite)(1); γ-Fe_2O_3 (maghemite) (1); $Mn/FeO(OH)$ (1); Fe,Mn oxide (1); $Na_2Fe_2Al(PO_4)_3$ (1); $Fe_2Bi(SiO_4)_2(OH)$ (1); $Bi,Fe\ PO_4$ (1); Fe_2MnO_4 (jacobsite) (1)

- Al – aluminosilicate (12); $Al(OH)_3$ (gibbsite) (10); $AlO(OH)$ (böhmite) (6); $Al(OH)_3$ (am) (5); $(Al_2O_3)_x \cdot (H_2O)_y$ (3); $Na_6(Al_6Si_6O_{24})(CaCO_3)(H_2O)_2$ (cancrinite) (2); $NaAlCO_3(OH)_2$ (dawsonite) (2); $AlPO_4$ (2); $Al(OH)_3$ (nostrandite) (1); $NaAlO_2$ (1); $Al_2O_3(H_2O)_x$ (c) (1); $Na_2Fe_2Al(PO_4)_3$ (1)

- Na – $NaNO_3$ (natratine) (13); $NaNO_2$ (4); $Na_6(Al_6Si_6O_{24})(CaCO_3)(H_2O)_2$ (cancrinite) (2); $NaAlCO_3(OH)_2$ (dawsonite) (2); Na_3PO_4 (2); $Na_4(UO_2)(CO_3)_3$ (čejkaite) (2); $Na_2CO_3 \cdot H_2O$ (1); $Na_2U_2O_7$ (1); $Na_3(NO_3)(SO_4)(H_2O)$ (darapskite) (1); $Na[(UO_2)O(OH)](H_2O)_{0-1}$ (clarkeite) (1); $NaAlO_2$ (1); $Na_2Fe_2Al(PO_4)_3$ (1)

- Mn – $MnC_2O_4 \cdot 2H_2O$ (lindbergite) (1); $MnCO_3$ (rhodochrosite) (1); $Mn/FeO(OH)$ (1); Fe,Mn oxide (1); Mn_2MnO_4 (1); Fe_2MnO_4 (jacobsite) (1); $Mn/FeO(OH)$ (1)

Table 4. Solid Phases Identified in Hanford Tank Sludge

Tank	Identified Solid Phases[a]	Method of Analysis	Waste Types[b]		Source Reference for Characterization Information
			Primary	Secondary	
AN-104	aluminosilicate (am) UO_2 or U_3O_7	TEM	DSSF	-	Lumetta et al. (1997)
AW-105	$Al(OH)_3$, aluminosilicate (c)	TEM, SEM, and XRD	NCRW	-	Lafemina (1995)
AY-102	$NaAlCO_3(OH)_2$ (dawsonite) $Na_6(Al_6Si_6O_{24})(CaCO_3)(H_2O)_2$ Cancrinite Fe_2O_3 (hematite)	XRD and SEM			Bechtold et al. 2003 Krupka et al. 2004
AZ-101	$NaNO_3$, $NaNO_2$, $Na_2CO_3 \cdot (H_2O)$	SEM	NCAW	-	Uziemblo et al. (1987),[c] unpublished results), as cited in Rapko and Lumetta (2000)
AZ-102	aluminosilicate (am) $NaNO_3$, $NaNO_2$, $Na_2U_2O_7$	SEM	NCAW	-	Uziemblo et al. (1987), unpublished results), as cited in Rapko and Lumetta (2000)
B-104	$Na_3(NO_3)(SO_4)(H_2O)$ (darapskite)	XRD	2C	EB	Temer and Villarreal (1996)
B-106	No solids	XRD	1C	TBP	Temer and Villarreal (1997)
B-110	sodium aluminum silicate hydrate $BiPO_4$ $NaNO_3$	SEM and XRD	2C	5 6	Jones et al. (1992)
B-111	aluminosilicates (c) $Bi_{38}CrO_{60}$ Na_3PO_4 $Fe(OH)_3$ (am), Bi_2O_3, $Fe_2Bi(SiO_4)_2(OH)$	TEM, SEM, and XRD	2C	5 6	Rapko et al. (1996); Lafemina (1995)
B-202	$NaNO_3$ (natratine)	XRD	224	-	Temer and Villarreal (1995)
BX-101	$Na_6(Al_6Si_6O_{24})(CaCO_3)(H_2O)_2$ Cancrinite	XRD			Krupka et al. 2004

Table 4. (contd)

Tank	Identified Solid Phases[a]	Method of Analysis	Waste Types[b]		Source Reference for Characterization Information
			Primary	Secondary	
BX-103	$Al(OH)_3$ (gibbsite)	XRD	TBP	CW	Temer and Villarreal (1997)
BX-105	$Al(OH)_3$ (gibbsite)	XRD	TBP	CW	Temer and Villarreal (1995)
BX-107	$AlPO_4$, $Al(OH)_3$ (am), aluminosilicates(c,am) $AlPO_4$, $Bi/FePO_4$ $Fe_2Bi(SiO_4)_2(OH)$, Bi_2O_3	TEM, SEM, and XRD	1C	TBP	Rapko et al. (1996); Lafemina (1995)
BX-109	$Al(OH)_3$ (nordstrandite) $NaNO_3$ (natratine)	XRD	TBP	CW	Temer and Villarreal (1996)
BY-104	$(Al_2O_3)_x \cdot (H_2O)_y$, aluminosilicates (am) $Fe(Fe,Cr)_2O_4$ (donathite) (Fleischer and Mandarino – mixture of magnetite and chromite)	TEM	TBP-F	EB-ITS	Lumetta et al. (1996a)
BY-108	$Ca_xSr_{10-x}(PO_4)_6(OH)_2$ β-U_3O_8, γ-Fe_2O_3 (maghemite), $FeO(OH)$	TEM	TBP-F	EB-ITS	Lumetta et al. (1997)
BY-110	ND	TEM	TBP-F	EB-ITS	Lumetta et al. (1996a)
C-104	No solids	XRD	CW	OWW	Temer and Villarreal (1997)
C-105	$Al(OH)_3$ (gibbsite) $UO_3 \cdot (H_2O)$	XRD	TBP	SR-WASH	Temer and Villarreal (1997)

Table 4. (contd)

Tank	Identified Solid Phases[a]	Method of Analysis	Waste Types[b]		Source Reference for Characterization Information
			Primary	Secondary	
C-106	$Al(OH)_3$ (gibbsite) $NaAlCO_3(OH)_2$ (dawsonite) $AlO(OH)$ (böhmite) $Al(OH)_3$ (am), aluminosilicates (am) Fe_2O_3 (hematite) $MnC_2O_4 \cdot 2H_2O$ (lindbergite) $MnCO_3$ (rhodochrosite) $CaC_2O_4 \cdot H_2O$ (whewellite)	TEM	SRS	SR-WASH	Deutsch et al. 2005 Lumetta et al. (1996b)
C-107	No Al-containing solid. $(Al_2O_3)_x \cdot (H2O)_y$, aluminosilicates (am) Fe_2O_3 (hematite) (XRD), $FeO(OH)$, ZrO_2	XRD; TEM	1C	CW	Temer and Villarreal (1996); Lumetta et al. (1996a)
C-108	$Al(OH)_3$ (gibbsite) $Ca_3(PO_4)_2$ $NaNO_3$ (natratine)	XRD	TBP-F	1C	Temer and Villarreal (1995)
C-109	$Al(OH)_3$ (gibbsite) $NaNO_3$, $NaNO_2$, SiO_2	SEM and XRD	TBP-F	1C	Colton et al. (1993)
C-112	$Al(OH)_3$ (gibbsite) $NaNO_3$, $NaNO_2$, SiO_2, CaU_2O_7	SEM and XRD	TBP-F	1C	Colton et al. (1993); Lafemina (1995)
C-203	$Na_4(UO_2)(CO_3)_3$ (čejkaite) $NaNO_3$ (niter) $Na[(UO_2)O(OH)](H_2O)_{0-1}$ (clarkeite)	XRD and SEM			Deutsch et al. 2004
C-204	$Na_4(UO_2)(CO_3)_3$ (čejkaite)	XRD and SEM			Deutsch et al. 2004
S-101	$AlO(OH)$ (böhmite)[c] $Mn/FeO(OH)$	TEM	R	EB	Lumetta et al. (1997)

Table 4. (contd)

Tank	Identified Solid Phases[a]	Method of Analysis	Waste Types[b]		Source Reference for Characterization Information
			Primary	Secondary	
S-104	AlO(OH) (böhmite) β-U_3O_8, $NaNO_3$ (natratine)	TEM, SEM, and XRD	R	-	Lumetta et al. (1997); Rapko et al. (1996); Temer and Villarreal (1995); Lafemina (1995)
S-107	AlO(OH) (böhmite), aluminosilicates (am) ZrO_2, FeO(OH), UO_3	TEM	R	EB	Lumetta et al. (1996a)
S-111	ND (not determined)	TEM	R	EB	Lumetta et al. (1997)
SX-108	AlO(OH) (böhmite), aluminosilicate (am), $(Al_2O_3)_x$·$(H_2O)_y$ β-U_3O_8, FeO(OH)	TEM	R	-	Lumetta et al. (1996a)
SX-113	No solids	XRD	R	DIA	Temer and Villarreal (1997)
SY-101	$NaAlO_2$, $Al(OH)_3$(am)	TEM, SEM, and XRD	CC	-	Lafemina (1995)
SY-103	$Al(OH)_3$ (am), $Al_2O_3(H_2O)_x$ (c) $Cr(OH)_3$ (am) Fe,Mn oxide	TEM, SEM, and XRD	CC	-	Rapko et al. (1996); Lafemina (1995)
T-104	$AlPO_4$, $Al(OH)_3$ (am), Aluminosilicates (c,am), $Na_2Fe_2Al(PO_4)_3$ $AlPO_4$, $Na_2Fe_2Al(PO_4)_3$(XRD) $Fe_2Bi(SiO_4)_2(OH)$, Bi_2O_3	TEM, SEM, and XRD	1C	-	Rapko et al. (1996); Lafemina (1995)
T-107	$Al(OH)_3$ (gibbsite) $NaNO_3$ (natratine)	XRD	1C	CW	Temer and Villarreal (1995)

Table 4. (contd)

Tank	Identified Solid Phases[a]	Method of Analysis	Waste Types[b]		Source Reference for Characterization Information
			Primary	Secondary	
T-111	Na_3PO_4, $La_4(P_2O_7)_3$, $Ca_5(OH)(PO_4)_3$, Bi,Fe phosphate $Fe(OH)_3$ (am), Mn_2MnO_4, Fe_2MnO_4 (jacobsite), $FeO(OH)$, (goethite)	TEM, SEM, and XRD	2C	224	Rapko et al. (1996); Lafemina (1995)
TY-104	$NaNO_3$ (natratine)	XRD	TBP	1C-F	Temer and Villarreal (1996)
U-110	$Al(OH)3$ (gibbsite), $AlO(OH)$ (böhmite) $NaNO_3$	SEM and XRD	1C	CW	Jones et al. (1992)
(a) Note: (am) refers to an amorphous solid; (c) refers to crystalline solid. Böhmite is the currently accepted spelling for this mineral name. Boehmite is equivalent to böhmite, and is the older spelling for this mineral name.					
(b) Detailed descriptions of the waste types in single-shell and double-shell tanks are given in Hill et al. (1995) and Hanlon (2000). Refer to Table 3 of this report.					
(c) Unpublished results by Unziemblo et al. (1987), as cited in Rapko and Lumetta (2000).					

The most commonly reported solids phases are those of Na [natratine (13), $NaNO_2$ (4)]; Al [aluminosilicate (12), gibbsite (10), böhmite (6), $Al(OH)_3$ (am) (5)]; Fe [$FeO(OH)$ (5), hematite (3)]; and U [β-U_3O_8 (3), čejkaite (2)]. Given the large number of tanks studied so far, it is somewhat surprising that so few solids have been identified. It is possible that the majority of the sludge is composed of amorphous compounds that cannot be identified by XRD and can only be tentatively identified by SEM.

3.0   Contaminants of Interest

The contaminants of interest in tank waste from the standpoint of long-term risk to groundwater are U, ^{99}Tc, ^{129}I, and Cr. These elements are of interest because they have the potential to be released from the waste, move through the vadose zone, and impact the underlying groundwater at a concentration that might be of risk to a future groundwater user. The primary geochemical processes that affect the release of contaminants from the residual waste and contaminant migration are the dissolution/precipitation of minerals containing the contaminant and desorption/adsorption of contaminants onto the surfaces of solids in the waste or naturally occurring material in the vadose zone. The solubility of minerals and the affinity of adsorbents for contaminants are functions of a large number of geochemical variables with the primary ones being pH, redox potential, solution speciation, ionic strength, and competition for adsorption sites.

This section discusses the general geochemistry of the contaminants of interest and the available information on occurrence and mass/activity (inventory) in Hanford single-shell tanks.

Inventory values were derived from a July 18, 2005, search of the TWINS BBI. The BBI is the official database for tank waste inventory estimates at the Hanford Site. It is based on sample information (when available), process knowledge calculations, and waste type templates based on sample data and Hanford Defined Waste (HDW) Model (Higley and Place 2004) estimates. A detailed discussion of BBI uncertainties and HDW model limitations is included in DOE/ORP-2003-02, *Environmental Impact Statement for Retrieval, Treatment and Disposal of Tank Waste and Closure of Single-Shell Tanks at the Hanford Site, Richland, WA; Inventory and Source Term Data Package*. The inventories provided below with each contaminant are totals for a tank and include sludge, saltcake, and fluids in the tank.

3.1   Uranium

Uranium (U) (atomic number 92) is a member of the actinide series of elements. The uranium isotopes of primary interest to waste disposal and site remediation activities at the Hanford Site include ^{235}U and ^{238}U. The following discussion of U geochemistry has been derived primarily from Krupka and Serne (2002). Additional summary information on U can be found in Langmuir (1997) and Burns and Finch (1999).

The U inventory in the tanks that have a reported quantity of sludge varies over seven orders of magnitude from about 1 g in tanks T-201 and B-204 to 37,400 kg in tank BX-104. The next two tanks with the highest U inventory are C-104 (28,700 kg) and C-112 (24,100 kg). Eleven tanks have a U inventory in the range of 10,000 to 20,000 kg and 72 tanks have from 1,000 to 10,000 kg of U.

3.1.1   Oxidation States

Uranium can exist in the +3, +4, +5, and +6, oxidation states in aqueous environments. Dissolved U(III) easily oxidizes to U(IV) under most redox conditions found in nature. The U(V) aqueous species (UO_2^+) readily disproportionates to U(IV) and U(VI). Consequently, U(IV) and U(VI) are the most common oxidation states of U in natural environments. Uranium exists in the +6 valence state under oxidizing to mildly reducing environments. The +4 valence state of U is stable under more strongly

reducing conditions, and is considered relatively immobile because it forms sparingly soluble minerals, such as uraninite (UO_2), under these redox conditions.

3.1.2   Aqueous Speciation

Grenthe et al. (1992), and revisions in Grenthe et al. (1995), have published an extensive, critical review of the thermodynamics of U. Figure 1 is an Eh-pH diagram for the speciation of U based on the thermodynamic data from Grenthe et al. (1992, 1995). The diagram was calculated for total concentrations of dissolved U, chloride, nitrate, carbonate, and sulfate of 0.024[1] (10^{-7} mol/L), 22, 1.7, 67.5, and 108 mg/L, respectively. The concentrations selected for these ligands are based on a composition for uncontaminated groundwater from the Hanford Site listed by Kaplan et al. (1996).
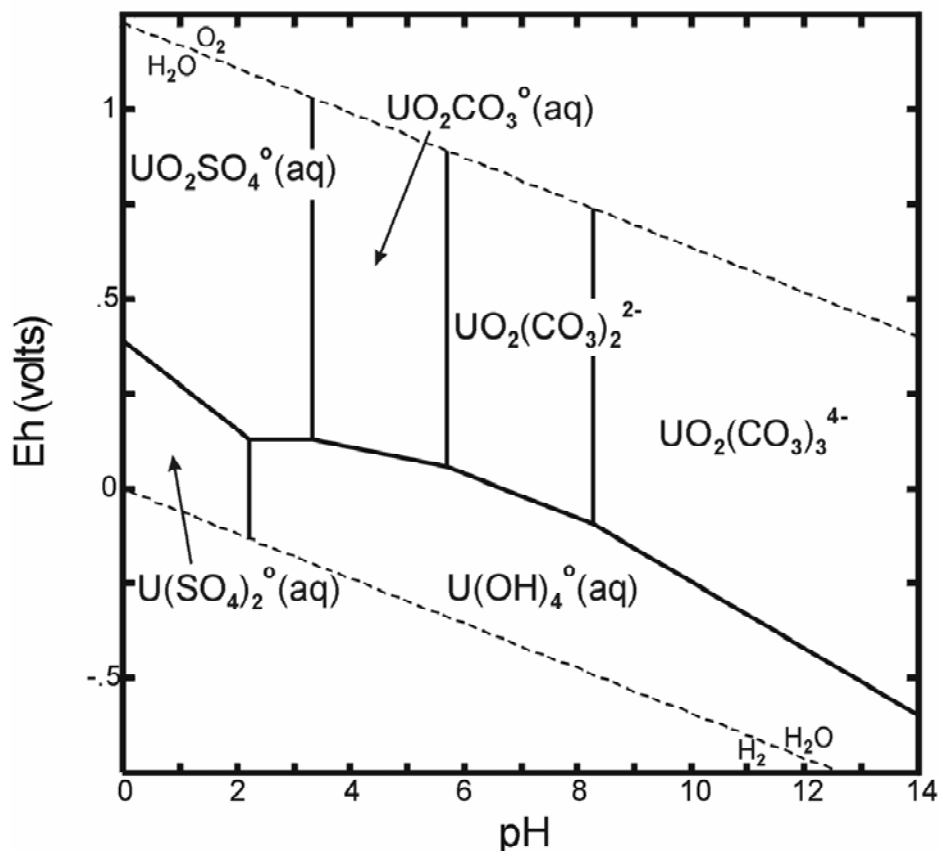
Figure 1. Eh-pH Diagram Showing the Dominant Aqueous Complexes of Uranium (Diagram was calculated at 25ºC and a concentration of 10^{-7} mol/L total dissolved uranium in the presence of dissolved chloride, nitrate, carbonate, and sulfate. Source: Krupka and Serne 2002.)

Figure 1 indicates that sulfate complexes would dominate the aqueous speciation of U at pH values less than 3. At higher pH values, the speciation of U(VI) is dominated by a series of strong aqueous carbonate complexes which increase the solubility of U at these environmental conditions (Langmuir 1997). Because anions commonly do not as readily adsorb to mineral surfaces at basic pH conditions as

---

[1] The interim drinking water standard (DWS) for U is 30 µg/L.

they do under acidic conditions (EPA 1999a), the anionic charge of the aqueous U(VI) carbonate complexes at pH values greater than 6 may result in decreased adsorption and thus increased mobility of U. The Hanford vadose zone and upper unconfined aquifer environments contain adequate carbonate concentrations to have these uranyl carbonate complexes dominate the aqueous speciation of U. Under reducing conditions, the speciation of U(IV) is dominated by $U(OH)_4^o$ (aq) at pH values greater than 2 in the presence of the dissolved chloride, nitrate, carbonate, and sulfate (Figure 1).

Although the concentrations of the ligands used to produce Figure 1 may be representative of the unsaturated and saturated zones, ligand concentrations in the Hanford tanks are quite variable and U speciation may be different than that shown in the figure. This would have an impact on U release from the residual waste that would be specific to the final liquid composition in each tank.

3.1.3   Solubility

Approximately 220 mineral species contain U as a necessary structural component (Krupka and Serne 2002). These include a diversity of simple and multiple oxides, carbonates, sulfates, molybdates, phosphates, arsenates, vanadates, and silicates that form under a variety of low and high temperature conditions. Finch and Murakami (1999) present a detailed review and extensive reference list on the structures [also see Smith (1984)] and formation conditions of U minerals. Given the omnipresence of carbonate in natural systems and the formation of aqueous U(VI) carbonate complexes (Section 3.1.2), adsorption instead of solubility will likely control the concentration of U(VI) under oxidizing conditions at dilute concentrations of dissolved U away from source terms of U contamination in the single-shell tanks.

Under reducing conditions or near a U source where elevated concentrations of U may exist, U mineral dissolution, precipitation, and coprecipitation processes become increasingly important and several U (co)precipitates may form depending on the environmental conditions (Finch and Murakami 1999; Falck 1991; Frondel 1958). These processes have a great effect on the concentrations of U(IV) in sediments, groundwaters, and geologic formations due to the low solubility of U(IV) under reducing conditions. Uraninite (compositions ranging from UO_2 to $UO_{2.25}$) and coffinite ($USiO_4$) are the two most important ore minerals of U (Langmuir 1997; Frondel 1958).

The stability diagram for U with solids (Figure 2) was calculated with total concentrations of U, chloride, nitrate, carbonate, and sulfate of 0.024, 22, 1.7, 67.5, and 108 mg/L, respectively. This figure shows the large Eh-pH region (shaded area) where the solubility of uraninite is exceeded under these conditions. Increasing the concentration of dissolved U expands the Eh-pH region of uraninite over-saturation to lower pH values and slightly higher oxidizing conditions. Thermodynamic calculations do not identify any potential solubility controls for dissolved U(VI) at the geochemical conditions used to determine Figure 2.
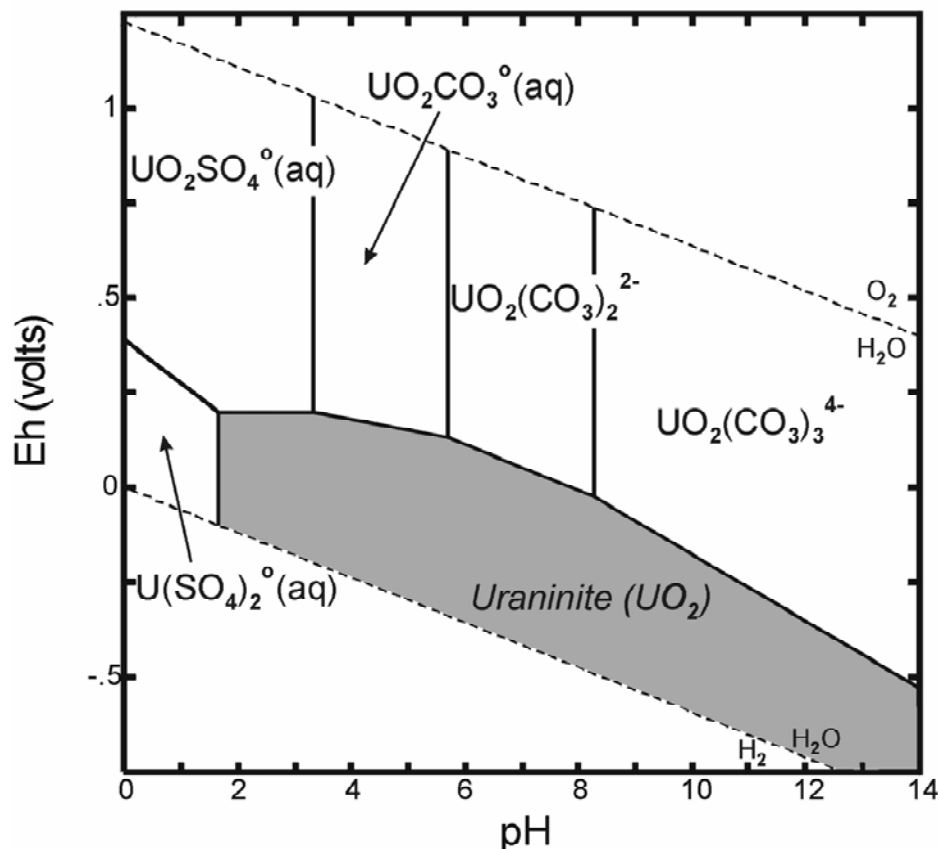
Figure 2. Eh-pH Diagram Showing Dominant Aqueous Species of Uranium and Eh-pH Region (shaded area) Where the Solubility of Uraninite Has Been Exceeded (Diagram was calculated at 25ºC and a concentration of 10^{-7} mol/L total dissolved uranium in the presence of dissolved chloride, nitrate, carbonate, and sulfate. Source: Krupka and Serne 2002.)

Mineral solubility processes are important relative to the environmental behavior of U(VI) under oxidizing conditions near U sources, where elevated concentrations of U can exist. Typical environments for Hanford include residual waste in the single-shell tanks, discharges of liquid waste from U processing facilities, and disposal sites of U-contaminated solids or soils. The U(VI) mineral čejkaite [$Na_4(UO_2)(CO_3)_3$] has been found in the waste material in Hanford tanks C-203 and C-204 and appears to control the initial release of U from these sludge (Deutsch et al. 2004). Other potentially important mineral solubility controls for U(VI) in these environments include compreignacite ($K_2U_6O_{19} \cdot 11H_2O$), uranophane [$Ca(UO_2)_2(SiO_3)_2(OH)_2 \cdot 5H_2O$], boltwoodite [$K(H_3O)UO_2(SiO_4) \cdot 1.5H_2O$], sklodowskite [$Mg(UO_2)_2(SiO_3)_2(OH)_2 \cdot 5H_2O$], becquerelite ($CaU_6O_{19} \cdot 10H_2O$), carnotite [$(K_2(UO_2)_2(VO_4)_2 \cdot 3H_2O$], schoepite ($UO_3 \cdot 2H_2O$), rutherfordine ($UO_2CO_3$), tyuyamunite [$Ca(UO_2)_2(VO_4)_2 \cdot 5\text{-}8H_2O$], autunite [$Ca(UO_2)_2(PO_4)_2 \cdot 10\text{-}12H_2O$], and potassium autunite [$K_2(UO_2)_2(PO_4)_2 \cdot 10\text{-}12H_2O$] (Langmuir 1997).

3.1.4 Adsorption

The adsorption behavior of U on geologic materials has been the subject of extensive study. The majority of these studies deal with the adsorption of U(VI). Because U(IV) is considered relatively

immobile due to its low solubility under reducing conditions (Section 3.1.3), adsorption studies of U(IV) are limited relative to those for U(VI). Uranium(VI) adsorption is the focus of the following discussion.

3.1.5   General Adsorption Behavior

An extensive review of published U adsorption studies is given in EPA (1999b). Uranium(VI) adsorbs onto a variety of minerals and related phases, including clays (e.g., Ames et al. 1982; Chisholm-Brause et al. 1994), oxides and silicates (e.g., Hsi and Langmuir 1985; Waite et al. 1994), and natural organic material (e.g., Borovec et al. 1979; Shanbhag and Choppin 1981; Read et al. 1993). Important environmental parameters affecting U migration include oxidation/reduction conditions, pH, concentrations of complexing ligands such as dissolved carbonate, ionic strength, and mineralogy.

As with the adsorption of most dissolved metals, aqueous pH has a significant effect on U(VI) adsorption due to the consequence of pH on U(VI) aqueous speciation and the number of exchange sites on variably charged surfaces of solids such as Fe-, Al-oxides, and natural organic matter. Figure 3 is a modification of Figure J.4 from the EPA (1999b) report; it shows the distribution of U(VI) K_d values reported in the literature as a function of pH. The values vary over the wide range of close to 0 to 10^6. Focusing on the open squares, which represent adsorption onto ferrihydrite, the measured adsorption
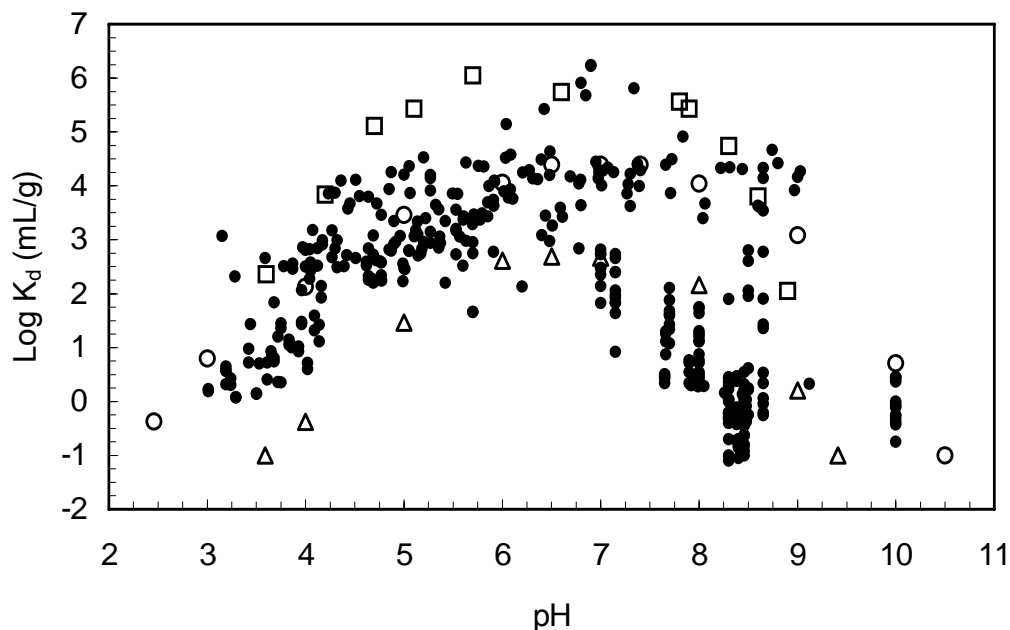
Figure 3. Distribution of U(VI) K_d Values for Sediments and Single-Mineral Phases as a Function of pH in Carbonate-Containing Aqueous Solutions. [Filled circles represent U(VI) K_d values compiled from the literature for sediments, and listed in Table J.5 in EPA (1999b). Open symbols represent K_d maximum and minimum values estimated from uranium adsorption measurements plotted by Waite et al. (1992) for ferrihydrite (open squares), kaolinite (open circles), and quartz (open triangles).]

of U(VI) in carbonate-containing aqueous solutions is relatively low (~100) at a pH value of 3.8, increases rapidly with pH to a maximum value of 10^6 at a pH of about 6, stays uniformly high to a pH of 8, and then decreases back to a value of 100 at a pH of 8.9 (Figure 3). This trend is similar to the in situ K_d values reported by Serkiz and Johnson (1994), and percent adsorption values measured for U on single mineral phases such as those reported for Fe oxides (Hsi and Langmuir 1985; Waite et al. 1992, 1994; Duff and Amrheim 1996), clays (Waite et al. 1992; McKinley et al. 1995; Turner et al. 1996), and quartz (Waite et al. 1992).

The observed low U(VI) adsorption (Figure 3) at acidic pH values is a consequence of the dominant U(VI) aqueous species being cationic and neutral (Figure 1) in this pH range where anions are preferentially adsorbed. As the pH increases to the circumneutral range, anionic U(VI) carbonate complexes become dominant and they adsorb strongly under these conditions. At pH values above 8, the adsorbents preferentially adsorb cations and the U(VI) anions are not as strongly attracted to the mineral surfaces. Surface complexation studies of U adsorption by Tripathi (1984), Hsi and Langmuir (1985), Waite et al. (1992, 1994), McKinley et al. (1995), Duff and Amrheim (1996), Turner et al. (1996), and others have shown that the formation of strong anionic U(VI) carbonate complexes decreases U(VI) adsorption at basic pH conditions. Differences in partial pressures of CO_2 can have a major affect on U adsorption at neutral pH conditions. Waite et al (1992), for example, show that the percent of U(VI) adsorbed onto ferrihydrite decreases from approximately 97% to 38% when CO_2 is increased from ambient (0.03%) to elevated (1%) partial pressures.

Kaplan et al. (1995) notes that U(VI) adsorption typically decreases with increasing ionic strength of an oxidized aqueous solution. The presence of increasing concentrations of other dissolves ions, such as Ca^{2+}, Mg^{2+}, and K^+, will displace the U(VI) ions adsorbed onto mineral surface sites, and release U(VI) into the aqueous solution. Therefore, the mobility of U(VI) is expected to increase in high ionic-strength solutions.

A significant amount of the variation in K_d values shown in Figure 3 at a given pH value is related to heterogeneity in the mineralogy of the soils and is an important factor relative to the adsorption behavior of U(VI). Soils containing larger percentages of Fe-oxide minerals and mineral coatings and/or clay minerals will exhibit higher sorption characteristics than soils dominated by quartz and feldspar minerals, such as found in Hanford Site sediments. This variability in U adsorption with respect to mineralogy is readily apparent from adsorption measurements for ferrihydrite (open squares), kaolinite (open circles), and quartz (open triangles) by Waite et al. (1992) shown in Figure 3. However, most compilations of K_d values and sorption information in general also incorporate diverse sources of errors resulting from different laboratory methods, soil and mineral types, length of equilibration (experiments conducted from periods of hours to weeks), and other factors. These sources of possible error are discussed in detail in EPA (1999a).

3.1.6 Surface Complexation Models

Numerous laboratory and modeling studies have been conducted using surface complexation of U onto single mineral phases. Electrostatic surface complexation models (SCMs) were developed to provide a mechanistic description of the adsorption of metals onto mineral surfaces.[2] Electrostatic surface complexation models have been incorporated into several geochemical modeling/reaction codes, such as MINTEQA2 (Allison et al. 1991), and can be used to predict U(VI) adsorption behavior and K_d values for certain mineral phases as a function of key geochemical parameters such as pH and dissolved carbonate concentrations. The current state of knowledge and availability of constants for using electrostatic SCMs to calculate the adsorption of U onto important soil minerals is probably as advanced as those for any other trace metal. These include studies of U adsorption onto Fe oxides (Tripathi 1984; Hsi and Langmuir 1985; Waite et al. 1992, 1994; Duff and Amrhein 1996; and others), clays (Waite et al. 1992; McKinley et al. 1995; Turner et al. 1996; and others), and quartz (Waite et al. 1992, and others).

Barnett et al. (2002) recently used batch adsorption experiments and a SCM to study the pH-dependent adsorption of U(VI) on sediment and soil samples from the Oak Ridge, Savannah River, and Hanford Sites. The sediment sample from the Hanford Site was from the Upper Ringold Formation, and was obtained from the White Bluffs area above the Columbia River. Barnett et al. (2002) used the SCM developed for the U(VI) adsorption onto ferrihydrite by Waite et al. (1994) to predict U(VI) adsorption on these sediments as a function of pH. Application of this model necessitated that Barnett et al. (2002) assume that all of the dithionite-citrate-bicarbonate extractable Fe oxides in these sediment samples were present as ferrihydrite. The modeling results of Barnett et al. (2002) qualitatively predicted the main characteristics of the pH-dependent adsorption of U(VI) on these sediments in carbonate-containing systems. Barnett et al. (2002) suggested that this modeling approach could be used to assess the relative mobility of U(VI) in geochemical systems by indicating whether U(VI) was weakly or strongly adsorbed onto the geologic materials. SCMs will likely receive increased use in the future in developing a better understanding of surface reactions and site conceptual models and in estimating limiting K_d values for the adsorption of metals, especially for U, in the Hanford tanks and the underlying vadose zone.

3.2 Technetium-99

Technetium (Tc) (atomic number 43) is a member of Group VIIB in the periodic classification of the elements. Technetium-99 is an isotope of primary importance to waste disposal and site remediation activities at the Hanford Site. Technetium-99 is generated as a fission product during the irradiation of U-containing nuclear fuels, and has a half live ($t_{1/2}$) of 2.11×10^5 yr. The behavior of Tc in environmental systems has been reviewed extensively by Lieser (1993), Gu and Schulz (1991), Sparks and Long (1987), Meyer et al. (1985), Beasley and Lorz (1984), Coughtrey et al. (1983), Onishi et al. (1981), Wildung et al. (1979), Ames and Rai (1978), and others. Hughes and Rossotti (1987) review in detail the solution chemistry of Tc. The following discussion of ^{99}Tc geochemistry has been derived primarily from Krupka and Serne (2002).

---

[2] Detailed descriptions, comparisons, and derivations of the relevant equations and reactions associated with electrostatic SCMs are described in Westall and Hohl (1980), Morel et al. (1981), Barrow and Bowden (1987), Davis and Kent (1990), Langmuir (1997), and others. Electrostatic SCMs typically incorporated into geochemical models include the diffuse layer model (DLM) [or diffuse double layer model (DDLM)], constant capacitance model (CCM), Basic Stern model, and triple layer model (TLM).

The ^{99}Tc inventory in the tanks that have a reported quantity of sludge varies over eight orders of magnitude from about 1.7 x 10^{-6} Ci (2.9 x 10^{-8} g) in tanks T-201, T-202, and B-201 to 352 Ci (5.97 g) in S-105. The next two tanks with the highest ^{99}Tc inventory are S-108 (341 Ci) and S-109 (329 Ci). Eleven tanks have a ^{99}Tc inventory in the range of 200 to 300 Ci, 24 tanks have an inventory in the range of 100 to 200 Ci, and 45 tanks have from 10 to 100 Ci of ^{99}Tc.

3.2.1   Oxidation States

In natural environments, the most stable valence states of Tc are +7 and +4 under oxidizing and reducing conditions, respectively. Other valence states are encountered chiefly in complex compounds (Mazzi 1989). The chemical behaviors of Tc in the +7 and +4 oxidation states differ drastically. In the +7 valence state, dissolved Tc exists as the pertechnetate anion, TcO_4^-, over the complete pH range of natural waters. Because the pertechnetate anion is highly soluble and is not strongly adsorbed at neutral and basic pH conditions, it is highly mobile in most oxidizing systems. In the +4 valence state, Tc is relatively immobile in the absence of strongly complexing ligands. Technetium(IV) forms the sparingly soluble $TcO_2 \cdot nH_2O$ solid. Because it has a significant affect on the mobility of Tc in waste streams, vadose zones, sediments, and groundwaters, the reduction of Tc(VII) to Tc(IV) by abiotic and biotic processes has recently been the subject of extensive studies (Lloyd and Macaskie 1996; Lloyd et al. 1997, 1998, 1999, 2000; Wildung et al. 2000; Fredrickson et al. 2000). These reaction processes are the basis for certain remediation technologies, such as permeable barriers composed of zero-valent Fe particles (i.e., as metallic Fe) or sodium-dithionite reduced soils, which are currently being tested for immobilization of groundwater contaminants.

3.2.2   Aqueous Speciation

Rard et al. (1999) have published an extensive, critical review of the thermodynamics of Tc. It is the most detailed review completed to date of the chemistry and available thermodynamic data for inorganic Tc compounds. Figure 4 is an Eh-pH diagram that shows the dominant aqueous hydrolytic species of Tc in the absence of dissolved ligands other than hydroxide. The diagram was calculated at 25ºC using a concentration of 5.30×10^{-5} mg/L ($10^{-9.27}$ mol/L) total dissolved Tc. This concentration corresponds to 900 pCi/L ^{99}Tc.[3] Under oxidizing conditions, the speciation of dissolved Tc is dominated by the pertechnetate oxyanion TcO_4^-. This ion is stable over the complete pH range of natural waters, and is not known to form any strong aqueous complexes. Under reducing conditions in the absence of dissolved carbonate, Tc aqueous speciation is dominated at pH values greater than 2 by the neutral Tc(IV) species $TcO(OH)_2^°$ (aq). Under strongly reducing conditions, the Eh-pH diagram suggests the possible formation of Tc^{3+} at pH values less than 2.

---

[3] The concentration of 900 pCi/L is the interim drinking water standard (DWS) for ^{99}Tc. It is based on the concentration of ^{99}Tc that is assumed to yield an annual dose equivalent of 4 mrem/yr.
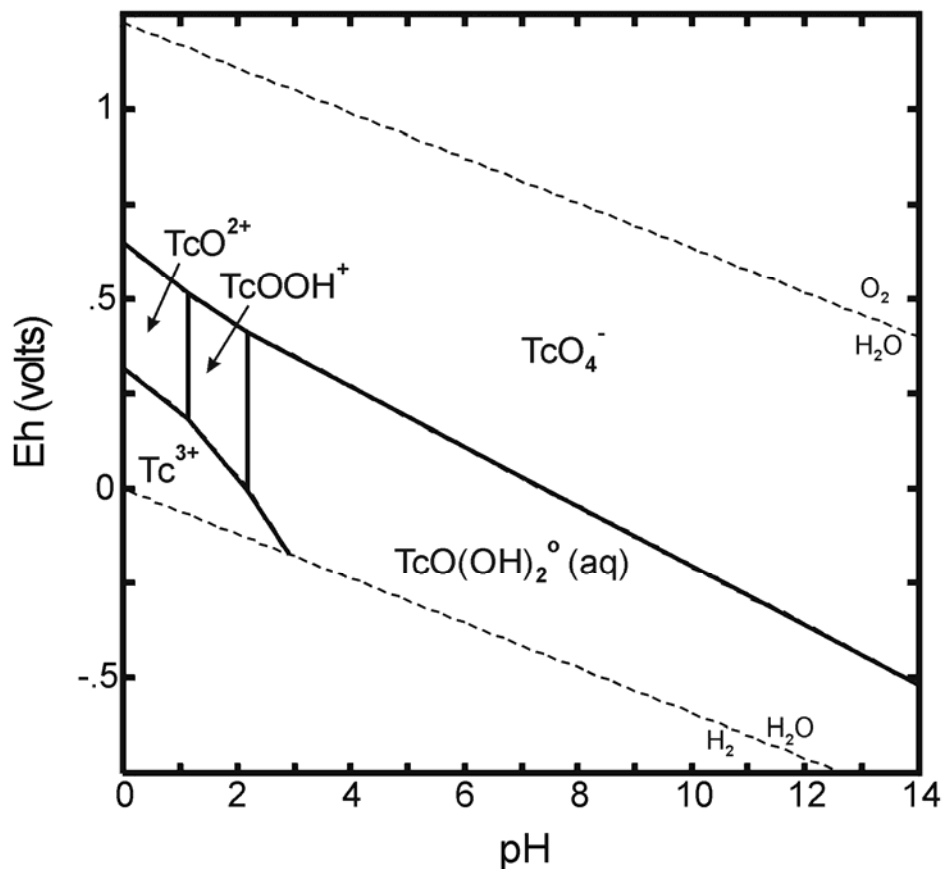
Figure 4. Eh-pH Diagram Showing Dominant Aqueous Species of Technetium in the Absence of Dissolved Carbonate [Diagram was calculated at 25ºC and a concentration of 5.30×10^5 mg/L ($10^{-9.27}$ mol/L) dissolved technetium. Source: Krupka and Serne 2002]

Although the thermodynamic stability of TcO_4^- is well established, thermodynamic data for other aqueous complexes and solids containing Tc in its various valence states are extremely limited. The absence of such data precludes the use of thermodynamic calculations to evaluate reduced species of dissolved Tc with respect to pH, Eh, and the presence of important dissolved complexing ligands such as carbonate, phosphate, sulfate, chloride, and others. The Tc(IV) carbonate complexes $TcCO_3(OH)_2^o$ (aq) and $TcCO_3(OH)_3^-$ are the only non-hydrolytic aqueous complexes of Tc for which Rard et al. (1999) list Gibbs free energy of formation ($\Delta G_{f,298}^o$) values. The thermodynamic constants listed for $TcCO_3(OH)_2^o$ (aq) and $TcCO_3(OH)_3^-$ are based on the solubility study of solid $TcO_2 \cdot xH_2O$ completed in the presence and absence of CO_2 (gas) by Eriksen et al. (1992). However, no independent measurements exist to verify the composition and thermodynamic properties of the Tc(IV) aqueous carbonate complexes.

Technetium(IV) carbonate complexes likely affect the aqueous speciation and solubility of Tc(IV) at near neutral and/or basic pH conditions. The results of other studies suggest the formation of Tc(IV) aqueous carbonate complexes. For example, Paquette and Lawrence (1985) reported spectrographic evidence for the formation of aqueous carbonate complexes with both Tc(III) and Tc(IV). Wildung et al. (2000) studied the effects of electron donor and the presence of dissolved bicarbonate on enzymatic reduction of Tc(VII) by the metal-reducing bacterium *Shewanella putrefaciens* CN32. Based on the

results of experiments conducted in bicarbonate solutions, Wildung et al. (2000) proposed the formation of a soluble, negatively-charged Tc(IV) carbonate complex that exceeds Tc(VII) in electrophoretic mobility and possibly dominates the speciation of dissolved Tc(IV) over neutral and basic pH values. Given that anionic aqueous complexes do not readily adsorb to geologic materials under near neutral and basic pH conditions, Wildung et al. (2000) suggested that the formation of anionic Tc(IV) carbonate complex(es) may represent an important mechanism for Tc migration in reducing geochemical environments. Generally, it has been assumed that Tc mobility in reducing environments is limited by the low solubility of Tc(IV) hydrous oxide (Section 3.2.3) and adsorption of aqueous Tc(IV) hydrolytic complexes. Given that dissolved carbonate is ubiquitous in surface, subsurface, and tank environments, further research is needed to determine the composition and thermodynamic properties of Tc(IV) carbonate complexes.

The potential complexation of technetium by dissolved EDTA, HEDTA, NTA, citrate, hydroacetic acid (or glycolate), TBP, and cyanide is important with respect to the chemical state of Tc in the underground storage tanks at the Hanford Site and its release to the environment (Krupka and Serne 2002). Krupka and Serne (2002) searched the stability constant database of Smith et al. (1997) to determine if data existed to calculate the thermodynamic distribution of Tc aqueous species containing any of these complexing ligands. The database by Smith et al. (1997) contains the Tc(VII) and Tc(IV) oxidation states, and does not list any stability constants for Tc(VII) and Tc(IV) aqueous complexes with EDTA, HEDTA, NTA, citrate, hydroacetic acid (or glycolate), TBP, or cyanide. It is important to keep in mind that the lack of thermodynamic data for such complexes in an extensive, well-accepted database, such as by Smith et al. (1997),[4] does not mean that such complexes are not important. The lack of tabulated thermodynamic constants may simply indicate that the formation of such complexes has not been studied from the perspective of determining their thermodynamic constants and/or that data available for such complexes are suspect and require additional study and independent determination.

Rard et al. (1999) review the available published studies for the complexation of Tc with cyanides and oxycyanides. The formation of complexes, such as $Tc^{VII}O(OH)_2(CN)_4^-$, $Tc^VO(CN)_5^{2-}$, $Tc^VO_2(CN)_4^{3-}$, $Tc^{VI}NCl_3(CN)^-$, have been suggested by these studies, but thermodynamic data are not available for such compounds (Rard et al. 1999).

Hughes and Rossotti (1987) review the literature pertaining to the solution chemistry of Tc as it relates to the reprocessing of nuclear fuels. The results of their review indicate that Tc forms stable complexes with aminopolycarboxylates, of which EDTA is the most common. Gorski and Koch (1970)[5] used an ion exchange method to study the complexation of Tc with aminopolycarboxylates. They determined a stability constant (log K) of 19.1 for the formation of $[Tc^{IV}OOH(EDTA)]^{3-}$. Later studies by Russell et al. (1980)[5] indicated that the net charge for this EDTA complex was -2, and the complex might be $[Tc^{III}OH(EDTA)]^{2-}$, $[Tc^{IV}O(EDTA)]^{2-}$, or $[Tc^VO(OH)(EDTA)]^{2-}$. Based on the relative stabilities of

---

[4] The National Institute of Standards and Technology (NIST) distributes the computerized database of critically-selected stability constants by Smith et al. (1997). This is version 4.0 of this database, and version 6.0 is currently available from NIST. The computerized database by Smith et al. (1997) supercedes the printed tabulations of stability constants published by these authors, such as Smith and Martell (1976) for stability constants for inorganic complexes.

[5] Information cited from Gorski and Koch (1970), Noll et al. (1980), and Russell et al. (1980) taken as given from Hughes and Rossotti (1987). Copies of original references were not available for this review.

the Tc oxidation states, Russell et al. (1980) proposed that the complex was most likely a Tc(III)-EDTA complex. Gorski and Koch (1970) also determined stability constants for the formation of Tc(IV)-NTA complexes. These constants included log K_1 of 13.8 for $[Tc^{IV}OOH(NTA)]^{2-}$ and log K_1K_2 of 28.7 for $[Tc^{IV}OOH(NTA)_2]^{5-}$, where K_1 and K_2 are the stepwise formation constants for the complexation of $TcOOH^+$ with NTA^{3-}. Hughes and Rossotti (1987) noted that the validity of these constants has been doubted by Noll et al. (1980) based on the irreversibility of the systems.

3.2.3   Solubility

Technetium(VII), TcO_4^-, is highly soluble, and does not form solubility-controlling phases in soil systems. As discussed in Section 3.2.1, Tc(VII) can be reduced to Tc(IV) by biotic and abiotic processes. This reduction results in a decrease in the dissolved concentration of Tc in the geochemical environment via the precipitation of the sparingly soluble solid $TcO_2 \cdot nH_2O$.

Numerous investigations have been conducted of the properties and hydration number of solid $TcO_2 \cdot nH_2O$ [see review of studies in Rard et al. (1999)]. Characterization data for this solid are limited, and a range of compositions, such as TcO_2 (cr), $TcO_2 \cdot nH_2O$, $TcO(OH)_2$, and $Tc(OH)_4$, have been proposed by various investigators. This solid is considered to be essentially amorphous (Rard et al. 1999). Meyer et al. (1991) studied the solubility of $TcO_2 \cdot nH_2O$ in the pH range from 1 to 10. The hydration numbers determined by Meyer et al. (1991) for their Tc solids ranged from 0.44 to 4.22 and from 1.38 to 1.81 for solids precipitated from acid and basic solution, respectively. For the formula used for $TcO_2 \cdot nH_2O$, Rard et al. (1999) selected 1.6, which corresponds to the value suggested by Meyer et al. (1991). However, as Rard et al. (1999) notes, the exact value for the hydration number has no consequence on the solution chemistry and predicted environmental mobility of dissolved Tc.

Figure 5 shows the predicted stability range (i.e., region of oversaturation) for $TcO_2 \cdot 1.6H_2O$ (am) as a function of Eh and pH calculated at 25ºC and concentration of 1×10^{-7} mg/L (1.7 pCi/L) total dissolved Tc in the absence of dissolved carbonate. The area of the diagram occupied by $TcO_2 \cdot 2H_2O$ (am) using the interim drinking water ^{99}Tc standard of 900 pCi/L ($10^{-4.3}$ mg/L) would be larger than that shown in Figure 5.

In reduced Fe-sulfide systems, Wharton et al. (2000) have shown that Tc(VII) can be reduced to Tc(IV) with coprecipitation with FeS solid (mackinawite). Due to the poorly ordered structures of the precipitates, they were not able to confirm if Tc(IV) was incorporated in the structure of the FeS solid or precipitated as a distinct Tc solid phase. Their x-ray absorption spectroscopy (XAS) results suggest that the reduction of Tc at these conditions may have precipitated a TcS_2-like phase (Wharton et al. 2000).
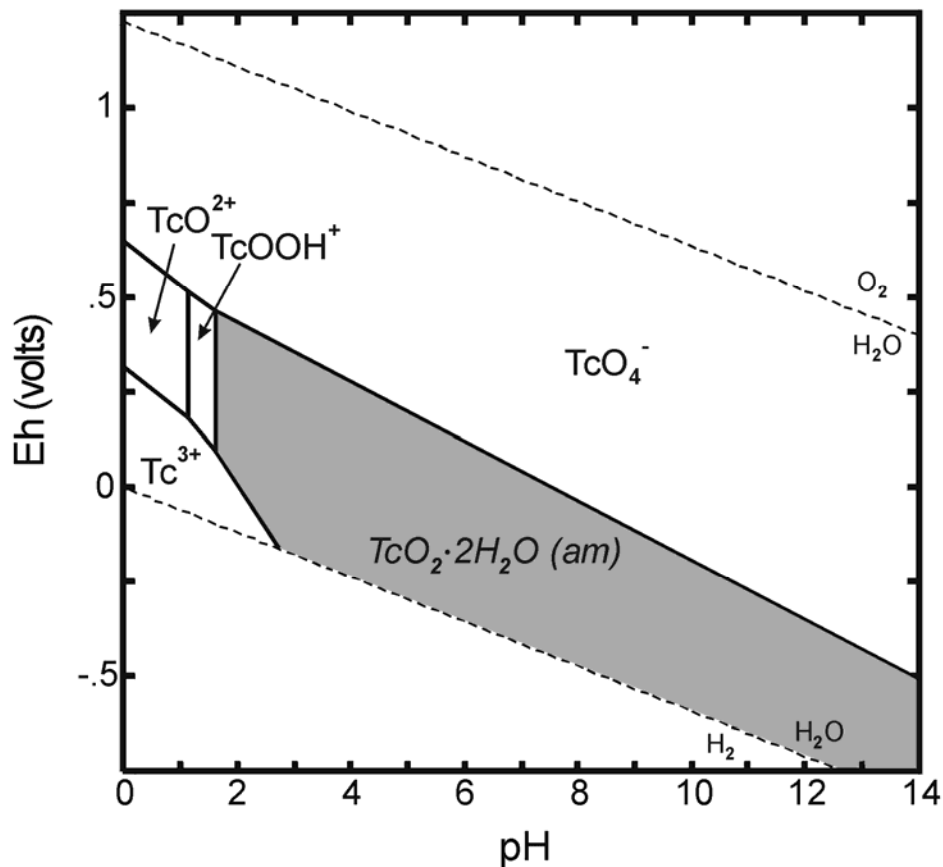
Figure 5. Eh-pH Diagram Showing Dominant Aqueous Species of Technetium and Eh-pH Regions (shaded areas) Where the Solubility of Solid Amorphous $TcO_2 \cdot 2H_2O$ Has Been Exceeded (Diagram calculated at 25ºC and a concentrations of 1×10^{-7} mg/L total dissolved Tc in the absence of dissolved carbonate. Source: Krupka and Serne 2002.)

3.2.4   Adsorption

Numerous studies of the sorption of Tc on sediments, soils, pure minerals, oxide phases, and crushed rock materials have been conducted. An extensive review of these studies is presented in EPA (2003). These studies consist of measurements of partition coefficient (K_d) values primarily for Tc(VII). No surface complexation (mechanistic) studies of the adsorption of Tc were identified during the review of Krupka and Serne (2002).

The dominant Tc aqueous species under oxidizing conditions is the Tc(VII) oxyanion TcO_4^- (Figure 4 and Figure 5), which is highly soluble. The adsorption of an anion, such as TcO_4^-, is expected to be relatively low at circumneutral and basic pH conditions, and to increase at lower pH values (EPA 1999, 2003). Technetium(IV) is considered to be essentially immobile, because it readily precipitates as sparingly soluble hydrous oxides and forms strong complexes with surface sites on Fe and Al oxides and clays (EPA 2003).

3.2.5 K_d Studies for Technetium on Sediment Materials

For soils with low contents of organic material, the reported K_d values for Tc(VII) range from 0 to approximately 0.5 ml/g, although most values are less than 0.1 ml/g (EPA 2003). The sorption of Tc(VII) has been found to be positively correlated to the organic carbon content of soils (Wildung et al. 1974). However, studies of the effect that organic material has on the sorption of Tc(VII) in soils are limited. As an extreme example, Sheppard and Thibault (1988) reported K_d values of greater than 2 ml/g based on in situ K_d values derived from analyses of the dried peat and pore water from the Precambrian Shield in Canada. Measurable adsorption of Tc(VII) observed in experiments conducted with organic material as well as with crushed rock and minerals containing reduced chemical components, such as Fe(II) and sulfide, has been attributed to the reduction of Tc(VII) to Tc(IV) and subsequent precipitation of Tc(IV) discrete and/or coprecipitated solid phases, as opposed to surface adsorption processes.

Cantrell et al. (2002) compiled the K_d values measured with Hanford sediments for radionuclides and other toxic constituents of environmental impact to the vadose zone and groundwater at the Hanford Site. Based on their review, Cantrell et al. (2002) concluded that the adsorption of Tc(VII) is low for nearly all of the geochemical conditions associated with the vadose zone and upper unconfined aquifer at the Hanford Site. In the database complied by Cantrell et al. (2002), the Tc K_d values typically ranged from zero to 0.1 ml/g, and were in a few studies as large as approximately 1 ml/g. Cantrell et al. (2002) noted that high standard deviations were associated with the highest K_d values reported for Hanford sediments.

3.2.6 K_d Studies for Technetium on Other Geologic Materials

Numerous technetium adsorption studies have been conducted of Tc on pure mineral, oxide phases, and crushed rock materials. The reader is referred to the studies tabulated in EPA (2003). High sorption of Tc is typically observed for minerals, such as sulfide minerals (e.g., chalcopyrite, pyrite), that have the capacity to reduce Tc(VII) to Tc(IV). For example, Strickert et al. (1980) measured K_d values in the range 100 to 2,000 ml/g for sorption of Tc on sulfide minerals such as bournonite ($PbCuSbS_3$), chalcopyrite ($CuFeS_2$), pyrite (FeS_2), tennantite ($(Cu,Fe)_{12}As_4S_{13}$), and tetrahedrite ($(Cu,Fe)_{12}Sb_4S_{13}$). Technetium K_d values were however less than 1 ml/g for non-sulfide materials, such as anhydrite, basalt, granite, and tuff. As noted previously, large K_d values measured for Tc(VII) in experiments conducted under oxic conditions and with geologic materials containing reduced chemical components, such as Fe(II) and sulfide, are likely the result of the reduction of Tc(VII) to Tc(IV) and subsequent precipitation of Tc(IV) as discrete and/or coprecipitated solid phases.

3.3   Iodine-129

Iodine (I) (atomic number 53) is a member of the halogen group and can exist in six oxidation states. There are thirty recognized isotopes of I; however, [127]I is the only stable isotope. Iodine-129, with a fission yield of 0.43% (Barton and McClanahan 1956), was created as a byproduct of Pu production in Hanford's nine production reactors. Due to its long half-life (15.7 million years) and relatively unencumbered migration in subsurface environments (Cantrell et al. 2003; Um et al. 2004), [129]I is a long-term risk driver in Hanford tank waste. The following discussion of I geochemistry has been derived primarily from EPA (2004). Additional summary geochemical information on I can be found in Langmuir (1997).

The [129]I inventory in the tanks that have a reported quantity of sludge varies over eleven orders of magnitude from about 2.92×10^{-11} Ci (5.17×10^{-15} g) in tanks B-204 to 2.18 Ci (3.86×10^{-4} g) in BY-105.

The three additional tanks that have a [129]I inventory greater than 1 Ci are BY-103 (1.65 Ci), BY-101 (1.63 Ci), and BY-112 (1.15 Ci). Forty-four tanks have a [129]I inventory in the range of 0.1 to 1.0 Ci and 37 tanks have a [129]I inventory in the range of 0.01 to 0.1 Ci. The 200-series tanks in B, C, T, and U Tank Farms generally have the lowest reported [129]I inventories.

3.3.1 Oxidation States and Speciation

Although I can exist in the -1, 0, +1, +3, +5, and +7 oxidation states, with -1, +5, and molecular I_2 oxidation states being the most commonly observed in aqueous/environmental samples. Iodine is typically present in the +5 oxidation state (iodate ion: IO_3^-) in highly oxidizing environments, such as surface waters and some oxygenated shallow groundwaters. In low pH oxidizing environments, molecular I_2 (aq) may form from the reduction of IO_3^- or oxidation of iodide (I^-). However, in most aqueous environments, I is present in the -1 valence state as I^-. As seen in Figure 6, I^- is the preferred species over nearly the entire pH/Eh stability range of water.
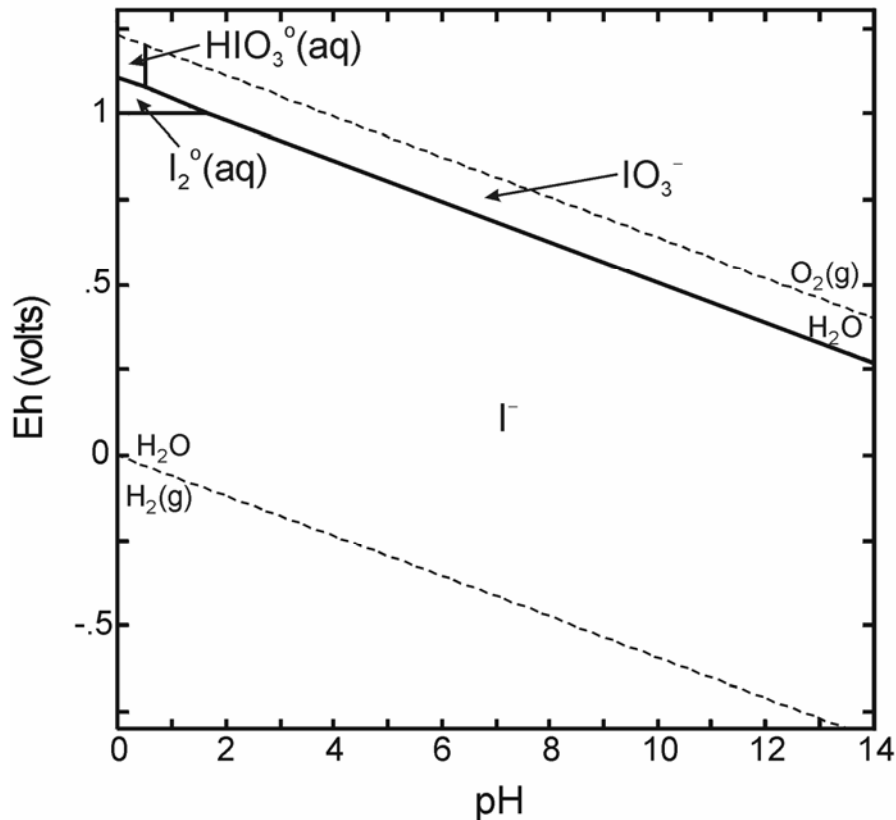
Figure 6. Eh-pH Diagram Showing the Dominant Aqueous Complexes of Iodine (Diagram was calculated at 25°C and a concentration of 10^{-8} mol/L total dissolved I. Source: Um et al. 2004.)

Little information exists on the speciation of I in tank waste, although it has been assumed that I exists predominantly in the relatively stable iodide form. The foundation of this assumption is based on the chemistry of Hanford tank waste, which can typically be characterized as high pH, high ionic strength, with a moderately reduced oxidation-reduction potential (Eh).

3.3.2   Solubility

Iodine is present as a trace constituent (1.4 µg/g) in the earth's crust (Wedepohl 1995). There are 24 recognized, naturally occurring minerals that contain I as an elemental component. For some of these minerals, I is present in substitution for other halogen elements, such as chloride and bromide. Minerals containing I in the +5 oxidation state (IO_3^-) are typically associated with calcium-bearing minerals found in sulfate- or nitrate-type minerals/deposits. For example, several I-containing minerals, including bruggenite [$Ca(IO_3)_2 \cdot H_2O$], lautarite [$Ca(IO_3)_2$], and dietzeite [$Ca_2H_2O(IO_3)_2(CrO_4)$], have been found in the northern Chilean nitrate deposits (Johnson 1994). With the exception of a few minerals [such as iodargyrite (AgI)], most of the I-containing minerals are expected to be highly soluble in natural systems. The formation of I-containing minerals is not likely to be important in most soil systems, although the precipitation of AgI could be a major sequestration mechanism for I in tank waste material.

3.3.3   Adsorption

As previously mentioned, I is typically present as an anion (either I^- or IO_3^-) in environmental samples. Therefore, conventional wisdom suggests that their adsorption on soils and most individual mineral phases will be negligible at near neutral and alkaline pH conditions, and increase as pH values become more acidic. Recent studies by Cantrell et al. (2003) and Um et al. (2004) have shown the potential range of K_d values for I under typical Hanford Site groundwater conditions to extend from 0 to 2 ml/g. The anticipated range of I K_d values at the Hanford Site is primarily constrained by the neutral to slightly basic groundwater present at the site, which is a result of the pervasive occurrence of carbonate minerals in Hanford sediments coupled with the discharge of predominantly alkaline waste streams to the environment from plant operations.

3.4   Chromium

Chromium (Cr) (atomic number 24) is a member of Group VIB in the periodic classification of the elements. The sources of Cr in the single-shell tanks are believed to be reprocessing waste (Anderson 1990) and corrosion of stainless steel process vessels and lines primarily within each plant (Agnew et al. 1997). The behavior of Cr in environmental systems has been reviewed extensively by Bartlett and Kimble (1976a, b), Bartlett and James (1979), James and Bartlett (1983a, b, c), Richard and Bourg (1991), Rai et al. (1988), Davis and Olsen (1995), and Zachara et al. (2004).

The Cr inventory in the tanks that have a reported quantity of sludge varies over four orders of magnitude from about 3.23 kg in tank U-204 to 1,130 kg in tank TX-108. The next two tanks with the highest Cr inventory are TX-104 (1,070 kg) and B-110 (1,030 kg). Forty-four tanks have a Cr inventory in the range of 100 to 1,000 kg and 12 tanks have from 10 to 100 kg of Cr.

3.4.1   Oxidation States

Chromium occurs under natural conditions in the +3 and +6 oxidation states. Trivalent Cr and its hydrolysis products are stable under reducing and moderately oxidizing conditions, and hexavalent Cr (CrO_4^{2-}, chromate) is stable under strongly oxidizing conditions. Dichromate (Cr_2O_7, Cr (VI)) compounds are used in many industrial processes as oxidizing agents and may exist in the environment near discharge locations.

3.4.2   Aqueous Speciation

Dissolved Cr occurs naturally in the environment as the Cr(VI) anion chromate (CrO_4^{2-}) and various Cr(III) hydrolysis species [$Cr(OH)_2^+$, $Cr(OH)_3^o$ and $Cr(OH)_4^-$]. The predominant species depends on the pH/Eh of the environment (Figure 7). Chromate predominates at higher Ehs (>500 mV at pH 6 and >300 mV at pH 9). At lower Eh values, the Cr(III) species are present at higher concentration than chromate with the dominant species being dependent on pH.
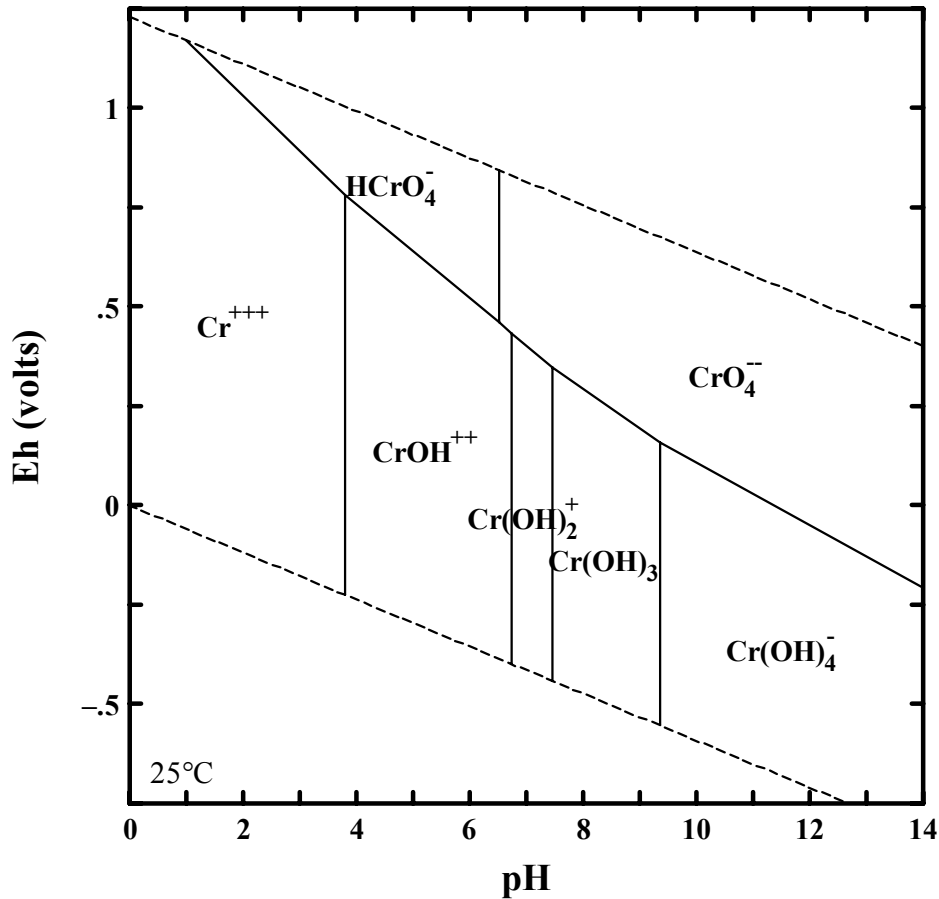
Figure 7. Aqueous Species of Chromium

3.4.3   Solubility

The dissolved Cr concentration is strongly dependent on pH and Eh because Cr(VI) minerals are relatively soluble compared to Cr(III) minerals. Under strongly oxidizing conditions where chromate is stable, total dissolved Cr concentrations can be much greater than 1 mg/L because of the high solubility of chromate minerals. Conversely, under more reducing conditions where Cr(III) species and minerals are stable, the total dissolved Cr concentration is typically much less than 1 mg/L because of the low solubility of Cr(III) minerals such as $Cr(OH)_3$ and $(Fe,Cr)(OH)_3$am. The Eh-pH diagram for this system shown in Figure 8 displays the large stability field of the amorphous $Cr(OH)_3$ solid. The contact lines between this solid and dissolved Cr species are calculated for a dissolved concentration of 10^{-6} mol/L (0.05 mg/L).
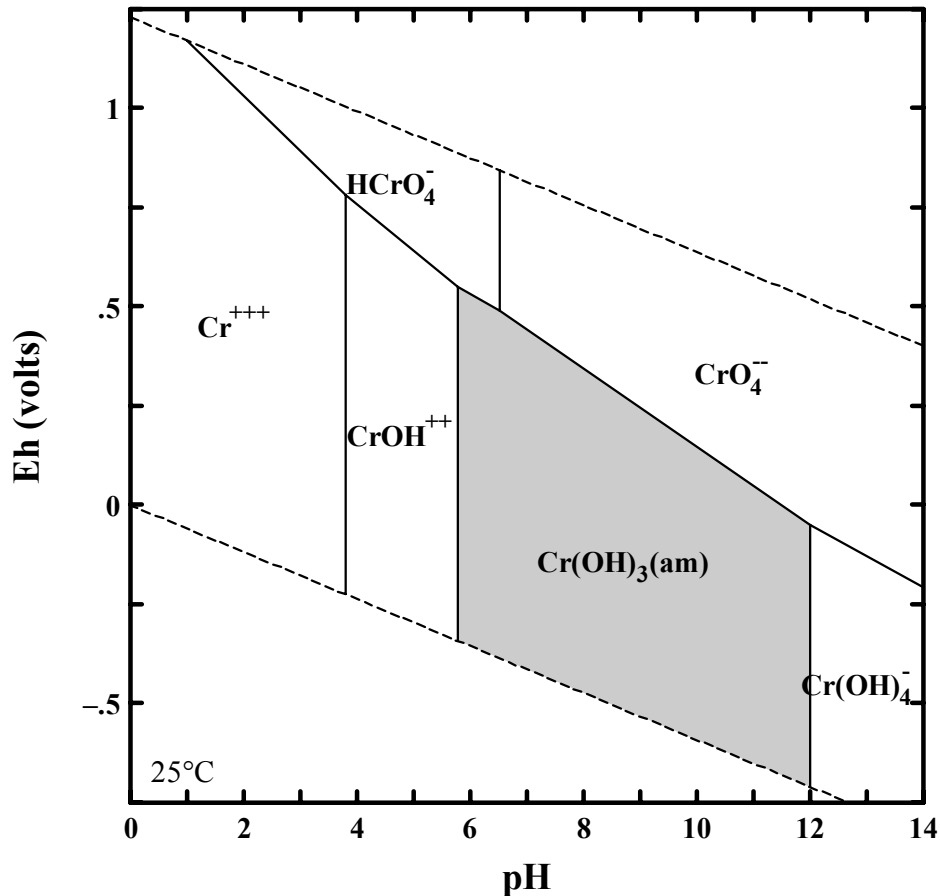
Figure 8. Dissolved Chromium Species and Stability Field of Cr(OH)$_3$ (am). (Cr$_{total}$ = 10^{-6} mol/L)

3.4.4   Adsorption

Chromium(III) and Cr(VI) have different adsorption properties because Cr(III) in the environment exists predominantly as a cation (CrOH^{++}, Cr(OH)$_2^+$) or neutral species (Cr(OH)$_3^o$) while Cr(VI) is an anion (CrO$_4^{2-}$). In the tank waste, the most likely adsorbents are oxides and hydroxides of Fe and Al. The surfaces of these solids preferentially adsorb anions below their zero points of charge, which are about pH 8 for Fe(OH)$_3$ (ferrihydrite) and pH 8.2 for Al(OH)$_3$ (gibbsite) (Langmuir 1997). Consequently, the chromate anion will be more strongly adsorbed on these solids below a pH of 8 than the cationic species of Cr(III). (Although Cr(III) may not be strongly adsorbed under these conditions, Figure 8 shows that it will precipitate and be removed from solution as the insoluble Cr(OH)$_3$ (am) mineral.) Competition for the anion adsorption sites may exist in the single-shell tanks between chromate, nitrate, nitrite, carbonate, sulfate, and other soluble anions in the waste.

Above pH values of about 8, the surfaces of the Fe and Al minerals preferentially adsorb cations. Adsorption of the chromate anion will be depressed in this pH region, and Cr(III) adsorption will also be low because it exists as the neutral species Cr(OH)$_3^o$ and the anion Cr(OH)$_4^-$ at high pH values. Total dissolved Cr will likely be low at high pH under reducing to moderately oxidizing conditions because of the low solubility of Cr(OH)$_3$ (am) under these conditions (Figure 8).

45

4.0   Test Method Advancements

This section describes the advancements that have been made in characterizing and testing sludge from the Hanford single-shell tanks. The discussion includes (1) extracting ^{129}I from the sludge and solution measurement by ICP-MS, (2) ^{90}Sr and TRU element solution measurement by ICP-MS, (3) mapping of element distribution in solids by SEM/EDS, (4) synchrotron-based x-ray analysis methods of sludge samples, and (5) Mössbauer spectroscopic analysis of Fe solids.

4.1   Iodine-129 Method Development

Iodine-129 is a long-term risk driver in Hanford tank waste. Because it decays via low-energy beta emission, ^{129}I is difficult to quantitatively measure in solid and aqueous samples. The following sections describe techniques/methods that were developed to extract ^{129}I from solid matrices and quantitatively measure the isotope using ICP-MS.

4.1.1   Iodine Extraction from Solid Matrices

Several techniques have been identified to extract iodine from solid matrices; however, all of them rely on two fundamental approaches: liquid extraction or chemical/heat facilitated volatilization. Speciation of I is important in any extraction process, and care must be taken during liquid extraction techniques not to volatilize I as HI or I_2. The majority of the liquid extraction techniques utilize either an alkaline leaching solution (typically sodium hydroxide) or fusion (sodium hydroxide or potassium hydroxide) followed by sample dissolution in deionized water to extract I from solid matrices (Nishiizumi et al. 1983). While these methods are typically chosen for their ease of implementation, they lack the ability to promote total sample dissolution. As previously mentioned, small partition coefficients have been measured for I on soil; therefore, extraction methods that do not result in total sample dissolution could underestimate the total I content of solid samples. Pyrohydrolysis techniques typically utilize temperatures in excess of 1000°C to volatilize I from the solid. A carrier gas, such as oxygen, transports the volatilized I to a trap containing an alkaline preservation solution (tetra methyl ammonium hydroxide with sodium bisulfite) (Muramatsu and Wedepohl 1998). Chemical volatilization can be performed using nitric acid and 30% hydrogen peroxide. The off-gas is then pushed into a stripping solution containing either carbon tetrachloride or sodium bisulfite (Moran et al. 1998). These techniques do not always result in total I volatilization and are, therefore, subject to the same shortcomings as the liquid extraction methods.

4.1.2   Iodine and Iodine-129 Analytical Methods

Several analytical techniques are available for the quantitative analysis of I in solution. Stable I (^{127}I) is most commonly measured using ion chromatography (IC). Ion chromatographic analysis of I is particularly useful due it its ability to discern speciation: iodide versus iodate. However, this analytical technique cannot differentiate between various isotopes of the same element. Another drawback of using IC to measure I is the inability to quantify the element at trace levels. Current I detection limits using IC are in the range of 1 mg/L. Under most circumstances, detection limits are not of great concern when analyzing solutions for stable I. For solutions containing radioactive isotopes of I, namely ^{129}I, instrument detection limits become critical. The current maximum contaminant level (MCL) for ^{129}I in

drinking water is 1 pCi/L, which equates to a solution concentration of 5.7 ng/L (parts per trillion). To achieve this concentration level, it is usually necessary to perform a series of separations followed by sample pre-concentration. This can be accomplished by performing repeated solvent extractions using carbon tetrachloride and nitric acid. The final step involves precipitation of the I using silver nitrate. At this point, the sample is ready for [129]I counting using low energy photon spectrometry (LEPS). This same technique can be utilized to pre-concentrate stable I in samples where it is present as a trace constituent. An advantage of this technique is that it allows for the pre-concentration of large quantities of sample, which can greatly improve the limit of quantification for the respective analysis. However, the multiple concentration steps are tedious and can lead to laboratory error. Furthermore, care must be taken during several steps of the procedure to ensure that volatilization of I does not occur. Finally, large masses of sample are not always available to allow significant pre-concentration.

Technological advancements in the field of ICP-MS have enabled this instrument to become a potential resource in the analysis of I. Unlike IC, ICP-MS instruments can measure multiple isotopes of the same element simultaneously. Two drawbacks of ICP-MS are that (1) it provides no information on the speciation of analytes, and (2) it cannot differentiate directly between elements with isotopes at the same mass (i.e., [238]U and [238]Pu). All shortcomings aside, ICP-MS instrumentation is capable of measuring many elements, primarily trace metals, at the part per quadrillion level (pg/L). Additionally, most samples can be analyzed without performing the specialized separations required by other techniques. However, I, being composed of anionic aqueous species, does require a special protocol in order to be analyzed via ICP-MS. Care must be taken during the analysis of samples to ensure that I does not sorb to instrument glassware, creating "memory" effects during the analytical run. This issue can be remedied by analyzing the samples in an alkaline matrix. The end result is an analytical method capable of measuring I, both [127]I and [129]I, in solution at the low nanograms per liter range.

4.1.3   Iodine Test Method Advancements

PNNL has developed a method that produces complete solid dissolution and conducted laboratory tests (using iodine salts, a standard reference material, and C-106 residual tank waste material) to assess its efficacy to completely extract I from solid matrices. Testing consisted primarily of potassium nitrate/potassium hydroxide fusion of the sample followed by sample dissolution in a mixture of sulfuric acid and sodium bisulfite. The sulfuric acid and sodium bisulfite solution was added to dissolve/reduce the residual solids and to prevent the volatilization of dissolved iodide. Once dissolved, the solution was analyzed directly on a Perkin Elmer DRC II ICP-MS using reaction cell technology. Sections 4.1.4 through 4.1.6 highlight the success of this fusion protocol as well as the accuracy and precision of this analytical technique.

4.1.4   Iodine Salt Analysis

The percent recoveries for the three replicate analyses of the I salts (KI and KIO$_3$) were all 95% or greater (Table 5). The high recoveries indicate that the extraction method had excellent reproducibility and that the form of I present does not affect extraction efficiency. Additionally, the extraction method was essentially 100% efficient, with overall average recoveries of 96.7% and 96.6% for the KI and KIO$_3$ salts, respectively. Although the average recoveries were similar, the range of percent recoveries measured during this study was more consistent than the 85% to 118% range reported by Anderson and Markowski (2000). Further, the precision of the extraction and analytical methods was superb, with standard deviations of 0.9% and 1.5% for the three replicates of KI and KIO$_3$ salts,

48

respectively. These results highlight two key points: (1) I in the form of either iodate or iodide is stable throughout the extraction process, and (2) this ICP-MS analytical method can be utilized to directly quantitate dissolved iodine in extraction solutions.

Table 5. [127]I Content of Salt Samples

Sample Identification	Weight (g)	[127]I (Recovery)
KI-1	0.0512	97.4
KI-2	0.0519	96.9
KI-3	0.0512	95.7
KIO$_3$-1	0.0668	95.0
KIO$_3$-2	0.0649	96.9
KIO$_3$-3	0.0646	97.9

4.1.5 Standard Reference Material 2709 Iodine Analysis

The total I concentration ([127]I) measured for the five replicates of San Joaquin Soil (SRM 2709) varied between 3.77 and 5.21 µg/g. (Table 6). The reported data have been blank corrected and combine results from both the liquid and solid extract fractions. The italicized data reported for samples SJS-4C and SJS-5C (both matrix spike samples) were corrected for the iodide spike contribution (the iodide spike contribution has been removed from the reported data). Overall, the data indicate that the extraction method was successful. There was excellent reproducibility in all of the replicates that contained greater than 0.1 g of solid mass. The results imply that the fusion extraction technique requires at least 0.1 g of soil when the solid contains 5 µg/g I. The average I concentration of the four samples that met this criterion was 4.9 µg/g with a relative percent standard deviation of less than 6%. Comparison of this result with the non-certified I content of the San Joaquin Soil resulted in a 98% recovery, which compared quite well with the results reported by Resano et al. (2005) and was considerably higher than the 89% recovery reported by Marchetti et al. (1994) for the same standard reference material.

Table 6. [127]I Content of San Joaquin Soil Sample SRM 2709

Sample Identification	Weight (g)	[127]I (µg/g)
SJS-1C	0.0528	3.77
SJS-2C	0.1051	4.55
SJS-3C	0.2051	5.21
SJS-4C	0.1506	*5.05*
SJS-5C	0.3152	*4.79*

4.1.6   C-106 Residual Tank Waste Iodine Analysis

Table 7 contains the blank corrected total I (^{129}I) concentration of each tank waste sample as a function of sample weight. The data reported for sample 405D-C (matrix spike) was corrected for the ^{129}I spike contribution. The duplicate tank waste samples from 404D (A and B) had an average ^{129}I concentration of 0.612 µg/g with a percent difference between the two samples of 6.6%. The three replicate aliquots from tank waste sample 405D (A, B, and C) highlight a greater degree of bulk sample heterogeneity. The three samples had an average ^{129}I concentration of 0.625 µg/g with a relative standard deviation of 17.3%. Although the measured relative standard deviation between the three replicate 405D tank waste samples was less than optimal, it was similar to that measured for other "mobile" constituents in the tank waste material using similar extraction and analytical techniques (Deutsch et al. 2005). The recovery (98.7%) of the ^{129}I blank spike sample, when coupled with the known heterogeneity associated with the respective tank samples, has made it possible to assume that the fusion was complete and quantitative for ^{129}I in the tank waste material.

Table 7. ^{129}I Content of Tank Samples

Sample Identification	Weight (g)	^{129}I (µg/g)	^{129}I (Recovery)
404D-A	0.2189	0.592	NA
404D-B	0.2053	0.632	NA
405D-A	0.2039	0.807	NA
405D-B	0.2686	0.654	NA
405D-C	0.3862	*0.416*	NA
Blank Spike	NA	NA	98.7
Shaded cell indicates that the reported value was corrected for the ^{129}I spike contribution.			

4.2   Inductively Coupled Plasma-Mass Spectrometry Method Development

Recent advances in the field of analytical chemistry have the potential to significantly change the way key tank waste radionuclides (^{90}Sr, ^{237}Np, ^{239}Pu, and ^{241}Am) are measured. Conventional techniques require multi-step "wet chemical" separation procedures utilizing commercially available exchange resins followed by analysis via radio-counting instrumentation (alpha energy analysis [AEA] and liquid scintillation counting [LSC]). Although these techniques typically provide low detection limits, their complexity can result in sample preparation errors. The state-of-the-art Perkin Elmer Elan DRC II ICP-MS, with its dynamic reaction cell (DRC) technology, has the potential to replace several radio-chemical separations and counting procedures currently being used at PNNL. Specifically, PNNL is developing analytical protocols using the Elan DRC II ICP-MS that will replace existing PNNL procedures for the analysis of ^{90}Sr (Lindberg 2004a, b) and actinides (Lindberg 2004c, d, e*).* Sections 4.2.1 through 4.2.2 provide background information on the need for these analyses and highlight test results to date.

4.2.1   Transuranic Analysis

ICP-MS is a widely accepted method to determine trace metals in solution. The instrument requires user calibration with multi-element standards in concentrations ranging from 5 pg/mL to 20 ng/mL. One area of concern in utilizing ICP-MS to measure actinide elements in tank waste extracts is the proximity in atomic mass of the elements of interest. It can be difficult to measure elements separated by only one atomic mass unit (amu) when one element is present in trace quantities (^{237}Np and ^{239}Pu) while the other element is present in macroscopic concentrations (^{238}U). Under these circumstances, peak tailing from the ^{238}U can extend into the regions corresponding to ^{237}Np and ^{239}Pu, resulting in erroneously high reporting of ^{237}Np and ^{239}Pu. A key feature of the Perkin Elmer Elan DRC II ICP-MS is the ability to inject a reaction gas, such as O_2, into the first quadrupole chamber. In the case of U, this promotes the formation of U oxide species that are filtered out prior to injection into the second (and primary) quadrapole. This creates a significant reduction in the background signal over the key actinide atomic mass range (237-241), resulting in instrument limits of quantification in the range of 7.1 pCi/L for ^{237}Np and 310 pCi/L for ^{239}Pu. Successful ICP-MS analysis of solution extracts from tank C-106 residual sludge has been documented by Deutsch et al. (2005). However, tank C-106 sludge samples contained nearly three orders of magnitude less U than sludge samples from tank C-203. PNNL is in the process of developing this methodology and plans to test its efficacy using sludge material from tanks C-203 and C-204. The following paragraph highlights the results to date.

Currently, PNNL has analyzed "surrogate" solutions of tank C-203 acid extracts containing 10 mg/L U with 0.1 µg/L of ^{237}Np, ^{239}Pu, and ^{241}Am. Using the dynamic reaction cell with O_2 as the reaction gas, the U signal was reduced from detector saturation to approximately 500,000 counts per second (equivalent to 5 µg/L solution). The three order of magnitude reduction in uranium signal was achieved with little or no loss in sensitivity for ^{237}Np, ^{239}Pu, and ^{241}Am. Although a reduction in U signal to this extent makes quantitative analysis of ^{237}Np, ^{239}Pu, and ^{241}Am possible (creates a sufficient reduction in peak tailing), the method can likely be optimized to provide an additional two orders of magnitude reduction in U signal. Therefore, analytical method testing/development is continuing by adjusting reaction gas flows and instrument power settings.

4.2.2   Strontium-90 Analysis

Typically, ICP-MS instruments can accurately quantify elements with stable isotopes and radioactive isotopes with sufficiently long half lives (greater than 400 years). PNNL is in the process of testing the ability of the Perkin Elmer Elan DRC II, with DRC technology, to quantitatively analyze ^{90}Sr (28.78 year half life) in the presence of ^{90}Y (2.67 day half life) and stable Zr by reacting and removing both Y and Zr oxides prior to injection of the sample into the second quadrupole. Although the instrument limit of quantification for ^{90}Sr may be high (5 to 100 µCi/L), most tank sludge material is expected to contain sufficiently high ^{90}Sr concentrations to make quantification feasible.

PNNL has begun developing an ICP-MS method using stable, single-element standards of Sr, Y, and Zr. Although all three elements will form oxides once ionized in a CO_2 atmosphere, Sr oxides will form slowest/last. This phenomenon is highlighted in Table 8, in which a solution containing 10 µg/L Sr, Y, and Zr was analyzed in standard analytical mode (no reaction gas) and in DRC mode with CO_2 as the reaction gas. The intensity of all three elements decreased as a result of oxide production; however, the Sr signal was only reduced by a factor of 70 while Y and Zr were reduced by factors of 3,900 and 13,700,

respectively. As seen in Table 8, the reacted Zr signal was reduced to 56 counts per second, which is essentially the background count rate for the instrument. Reacted Y counts were reduced to 476 counts per second, which is above the background count rate of the instrumentation, but is only 2% of the reacted Sr counts for the same concentration solution (10 µg/L).

Table 8. Strontium, Yttrium, and Zirconium Analysis (10 µg/L) With and Without DRC Technology

Element	Standard Intensity (counts per second)	CO_2 Reacted Intensity (counts per second)
Strontium	1,584,759	22,338
Yttrium	1,863,132	476
Zirconium	768,091	56

Additional method development testing is currently underway. Once the analytical method has been optimized (reaction gas flows/instrument settings), extracts from C-106 residual sludge samples (approximately 3,500 µCi/g ^{90}Sr) will be used to verify this new analytical technique. The ICP-MS results from this effort will be compared with the "conventionally measured" values based on ^{90}Sr wet chemical separation and LSC as reported in Deutsch et al. (2005).

4.3   SEM/EDS Mapping of Element Distributions

A JEOL JSM-840 scanning electron microscope (SEM) with an Oxford Links ISIS 300 energy dispersive spectroscopic (EDS) system was used for PNNL's studies of residual sludge samples from tanks AY-102, BX-101, C-203, C-204, and C-106 (Deutsch et al. 2004, 2005; Krupka et al. 2004). In late 2004, this instrumentation was upgraded to the INCA EDS system (Oxford Instruments, Concord, Massachusetts). In addition to allowing the operator to record EDS spectra at individual points within an SEM imaged area, this system upgrade allows automatic collection of EDS spectra over user-specified, multi-micrometer-sized areas of an SEM-imaged sample. Because this capability records the complete EDS spectrum at each point over the scanned area, the INCA software can be used with the collected matrix of EDS spectra to generate maps or line profiles of the distributions of the relative concentrations for up to three elements specified by the user.

The capability of this new system was tested by generating single and multiple element distribution maps for unleached samples of AY-102 residual waste and unleached, 82-day water-leached, and hydrofluoric (HF)-extracted C-106 residual waste samples. Although the instrument upgrade occurred after the principal studies and analyses of tank C-106 residual waste had been completed and presented in draft form for review, the element distribution maps collected for the C-106 sludge samples were inserted in the C-106 final report (Deutsch et al. 2005).

As discussed in earlier reports (Deutsch et al. 2004, 2005; Krupka et al. 2004), SEM/EDS was used for high-resolution imaging of the morphologies, sizes, surface textures, and compositions of micrometer/ submicrometer-size particles present in the unleached and various leached samples of tank residual waste. The mounts used for SEM/EDS consisted of double-sided carbon tape attached to standard Al mounting stubs. For each mount, small aliquots of each sludge sample were placed on the exposed upper surface of the carbon tape using a micro spatula. Each mount was then coated with carbon using a vacuum sputter-coater to improve the conductivity of the samples and the quality of the SEM images and EDS signals.

The operating conditions for the SEM system were 10 to 20 keV for SEM imaging and 20-30 keV, 100 live seconds for the EDS analyses. The EDS analyses of particles are limited to elements with atomic weights heavier than boron.

To help identify particles that contain elements with large atomic numbers, such as U, the SEM was typically operated in the backscattered electron (BSE) mode. BSE emission intensity is a function of the element's atomic number ─ the larger the atomic number, the brighter the signal. The entire area of each SEM mount was examined by SEM at low magnification (typically 50 to 100x) to identify those particles and surface features that were typical or unusual for the sample. During this examination, SEM micrographs were recorded at low magnification (e.g., 100x) for typically two to four areas of the mount to provide a general perspective of the sizes, types, and distributions of particles that make up the SEM mount. Within these imaged regions, additional SEM micrographs were recorded of several particles at greater magnifications to provide a more detailed representation of the particles' characteristics, and selected points on these particles then analyzed by EDS. Depending on the perceived importance of such particles, regions on these particles were sometimes analyzed by SEM and EDS at even greater magnifications.

4.3.1   Results of SEM/EDS Element Mapping

4.3.1.1   Residual Waste from Tank AY-102

In February 2005, the SEM/EDS element mapping capability of the INCA system was used to analyze a sample of unleached sludge from tank AY-102. This sample was analyzed to compare these results with similar analyses completed on unleached sludge from tank C-106. The intent was to use the results for the unleached samples of AY-102 and C-106 residual waste in a journal article under preparation, which is tentatively titled *Characterization of Solid Radioactive Waste from Hanford Tanks 241-C-106 after In Situ Treatment with Oxalic Acid*.

Figures 9 and 10 show BSE SEM images and the associated colorized, three-element distribution maps for particle aggregates present in unleached samples of AY-102 residual waste. The particle aggregates were imaged at low and high magnifications, which are shown, respectively, on the left and right sides each of these figures. The colors in the element maps denote the presence of the indicated, user-specified elements, where the red areas signify the presence of one specified element, the green areas for the presence a second element, and so forth. The INCA software has the capability to create colorized maps for up to three elements selected by the user. Figure 9 indicates those regions enriched in Fe (red); Si (green); U (blue); Fe and Si (yellow); and Fe, Si, and U (white). Figure 10 shows those areas in the sludge sample containing detectable concentrations of Fe (red), Si (green), and Ag (blue). Because this SEM/EDS element mapping capability records the complete EDS spectra at each point over the scanned area, this provides an effective means to quickly identify particles enriched with elements and contaminants of interest, and show their correlation with other elements present in the sludge materials.
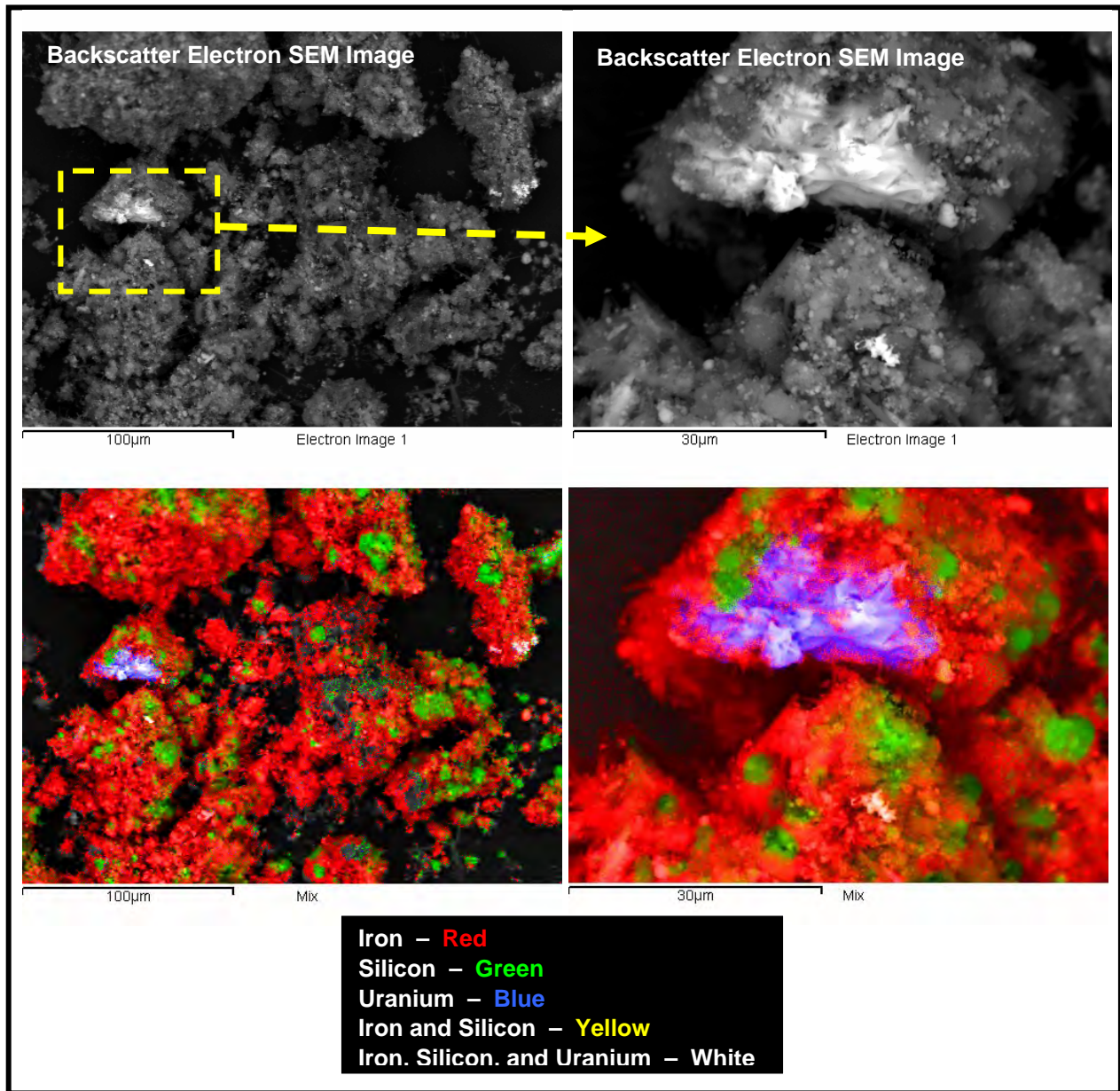
Figure 9. Backscatter-Electron SEM Image with Colorized Element Maps for Iron, Silicon, and Uranium in Particle Aggregates in Unleached Residual Waste from Tank AY-102 (Area marked by yellow-dashed rectangle in upper left figure shown at higher magnification on right side.)
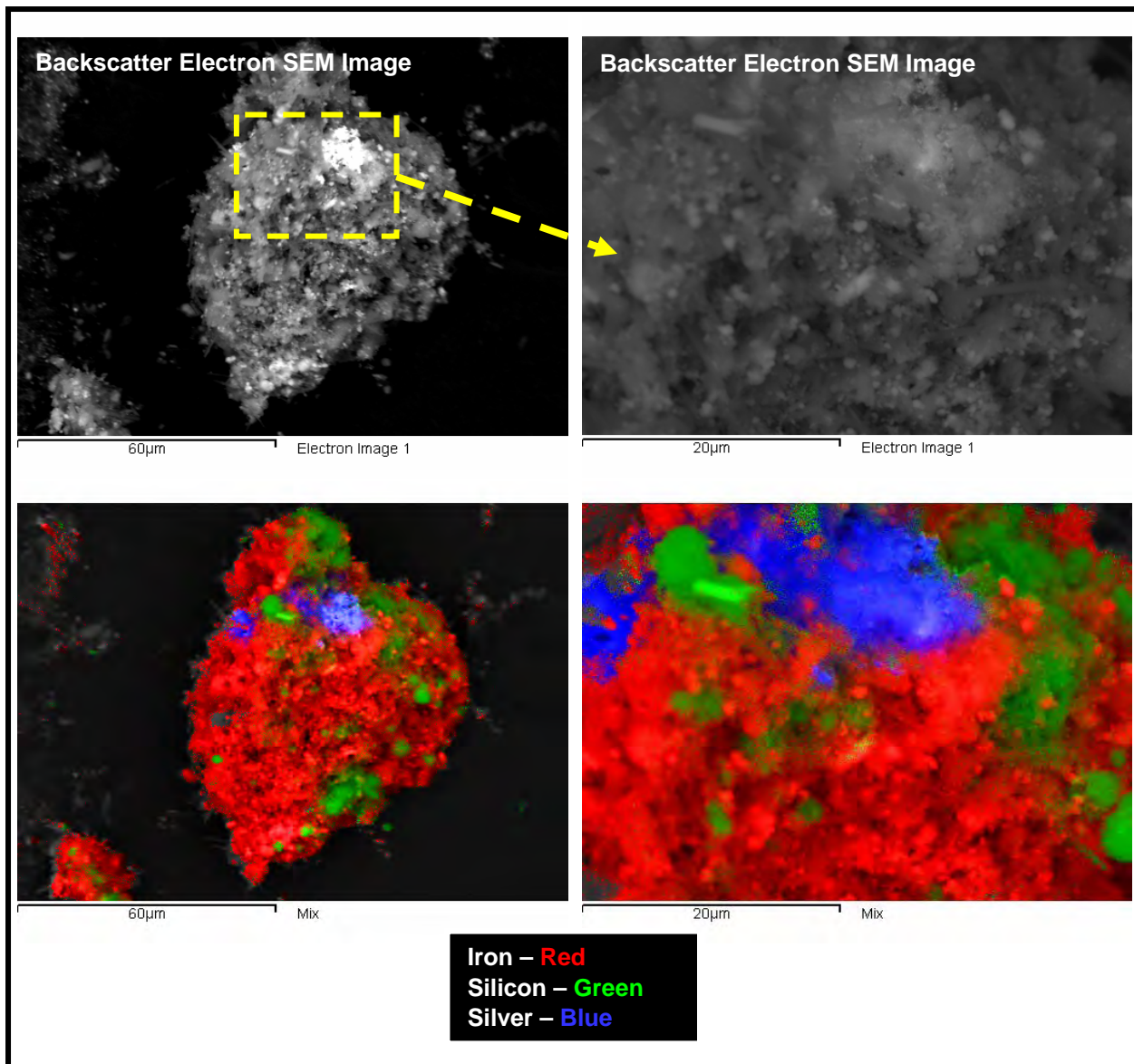
Figure 10. Backscatter-Electron SEM Image with Colorized Element Maps for Iron, Silicon, and Silver in a Particle Aggregate in Unleached Residual Waste from Tank AY-102 (Area marked by yellow-dashed rectangle in upper left figure shown at higher magnification on right side.)

Figures 11 through 14 show low and high magnification BSE SEM micrographs (top of each figure) for particle aggregates present in unleached residual waste from tank AY-102, and single-element distribution maps showing regions of this material that are enriched in the elements O, Na, Si, Fe, Mn, Al, Ca, Ni, P, and U, respectively. The top of Figures 11 through 14 includes a BSE SEM micrograph of the area of the sample mount that was scanned by EDS using the INCA system. The series of single-element distribution maps included below each BSE SEM image show the spatial distributions of the relative concentrations for the indicated elements. The concentration of each listed element is directly proportional to the regions of brightness (i.e., the brighter the area, the higher the concentration of the selected element) in the corresponding distribution map. The element associations indicated in Figures 11 through 14 are consistent with the EDS spot analyses reported in Krupka et al. (2004). However, the element distribution maps produced by the INCA system provide a more detailed and effective visualization of the spatial distributions of the selected elements within the imaged particle assemblage, which are not apparent from numerous spot EDS analyses made on different individual particles. Consistent with the results in Krupka et al. (2004), the element distribution maps prepared using the INCA system did not reveal any regions of any particles that had detectable concentrations of ^{129}I or ^{99}Tc.
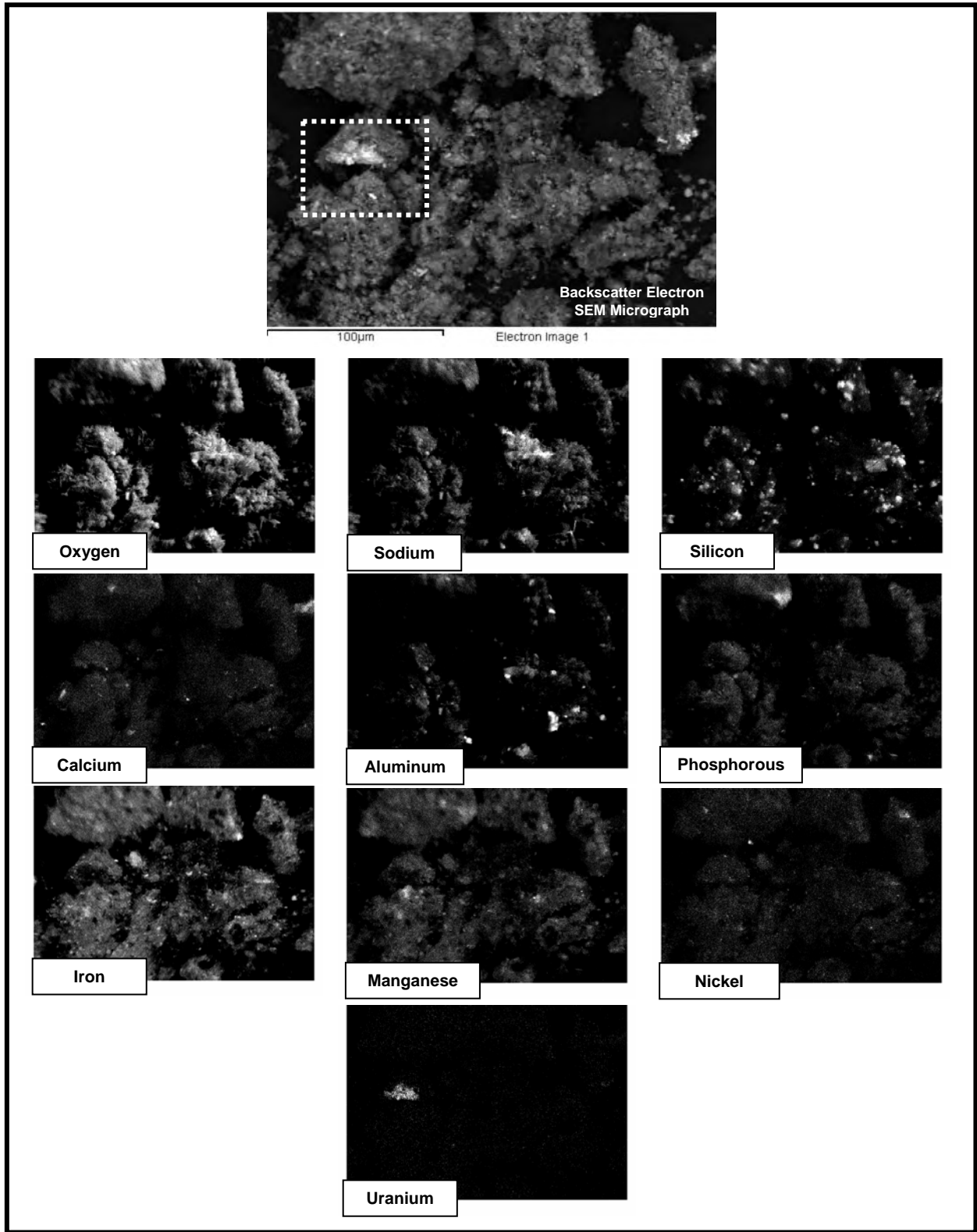
Figure 11. Low Magnification Backscatter-Electron SEM Micrograph and Element Distribution Maps for Particle Aggregates in Unleached Sludge from Tank AY-102
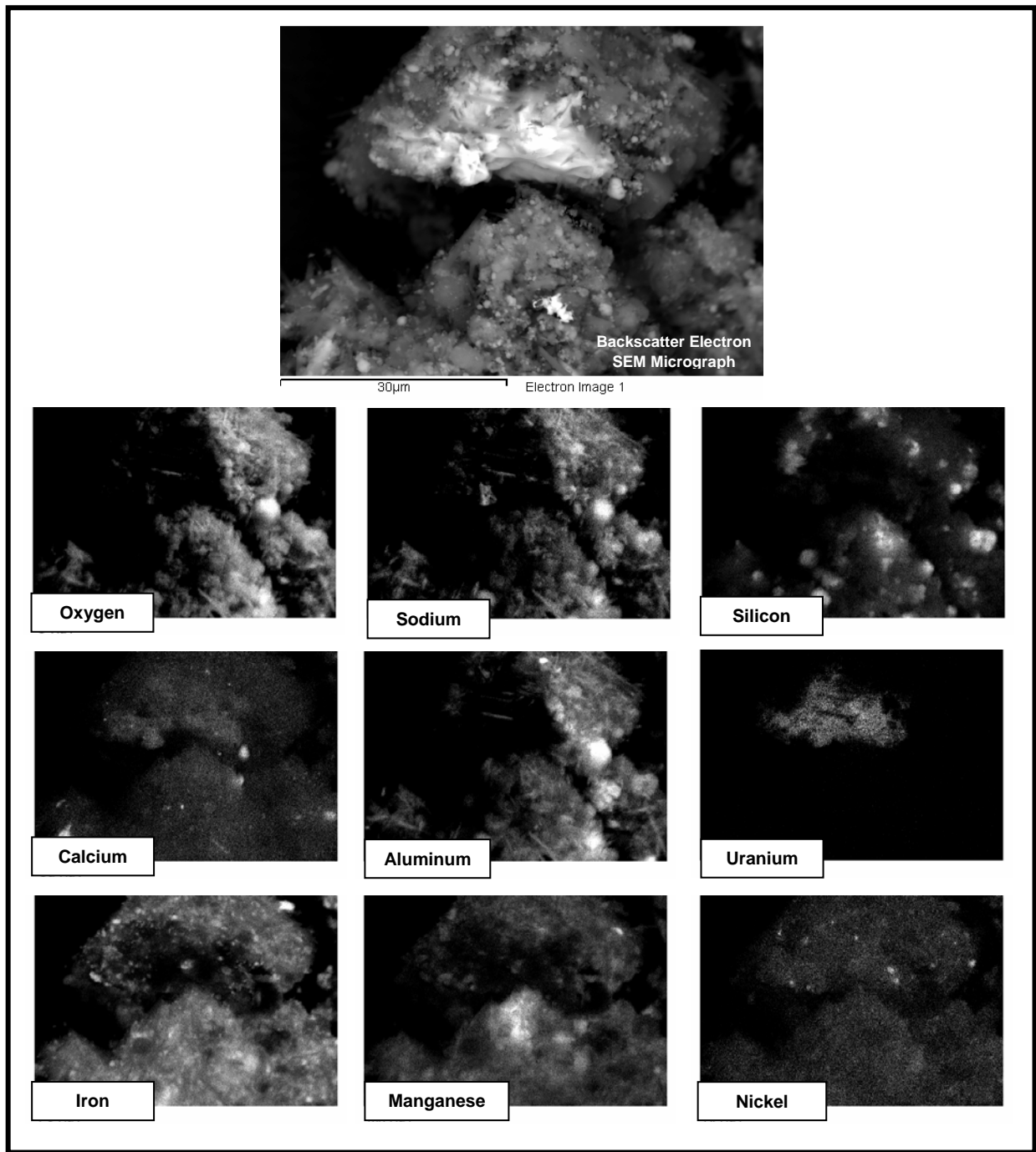
Figure 12. Higher Magnification Backscatter-Electron SEM Micrograph and Element Distribution Maps for the Area Indicated by a White Dotted-Line Rectangle in Figure 11
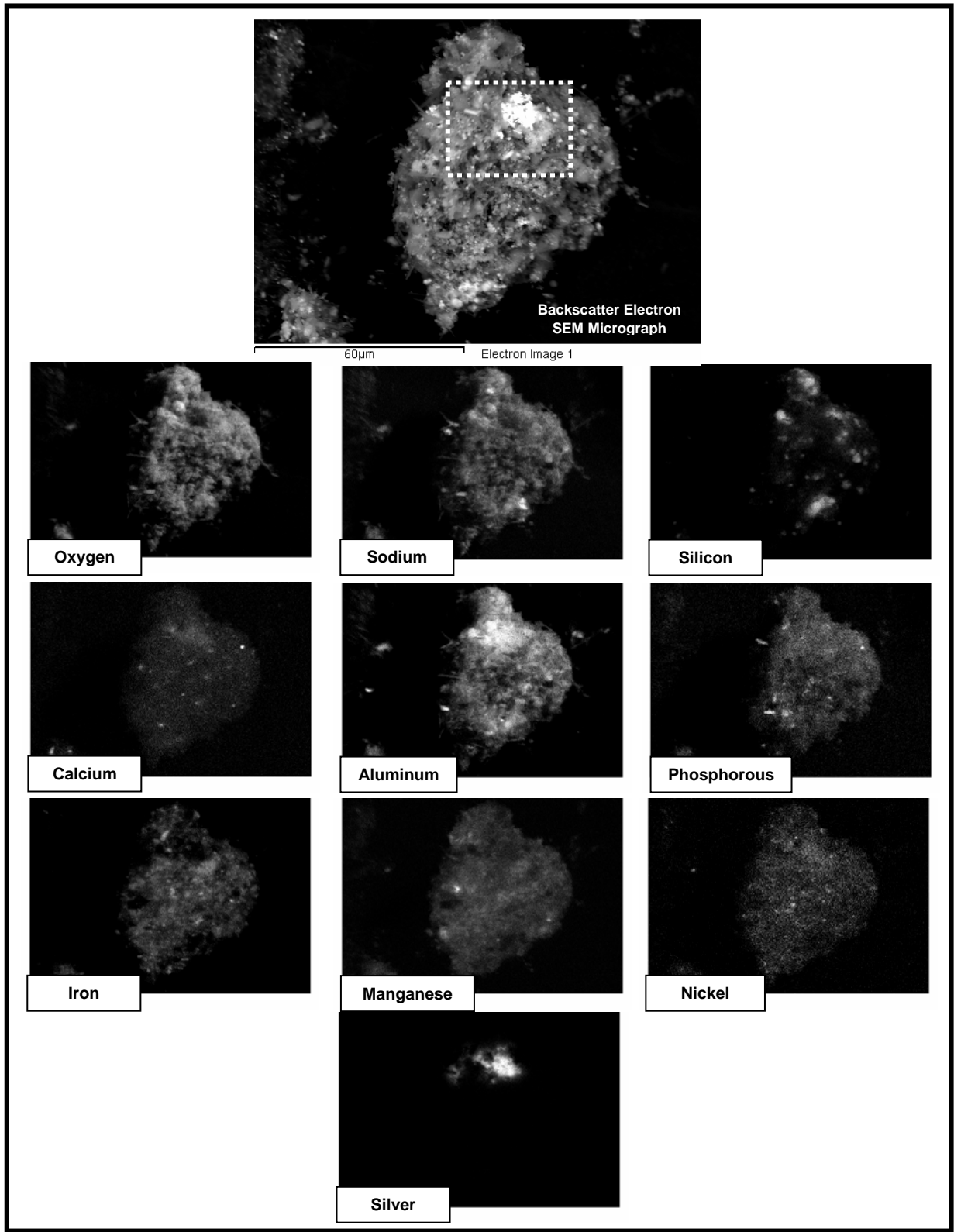
Figure 13. Low Magnification Backscatter-Electron SEM Micrograph and Element Distribution Maps for a Particle Aggregate in Unleached Sludge from Tank AY-102
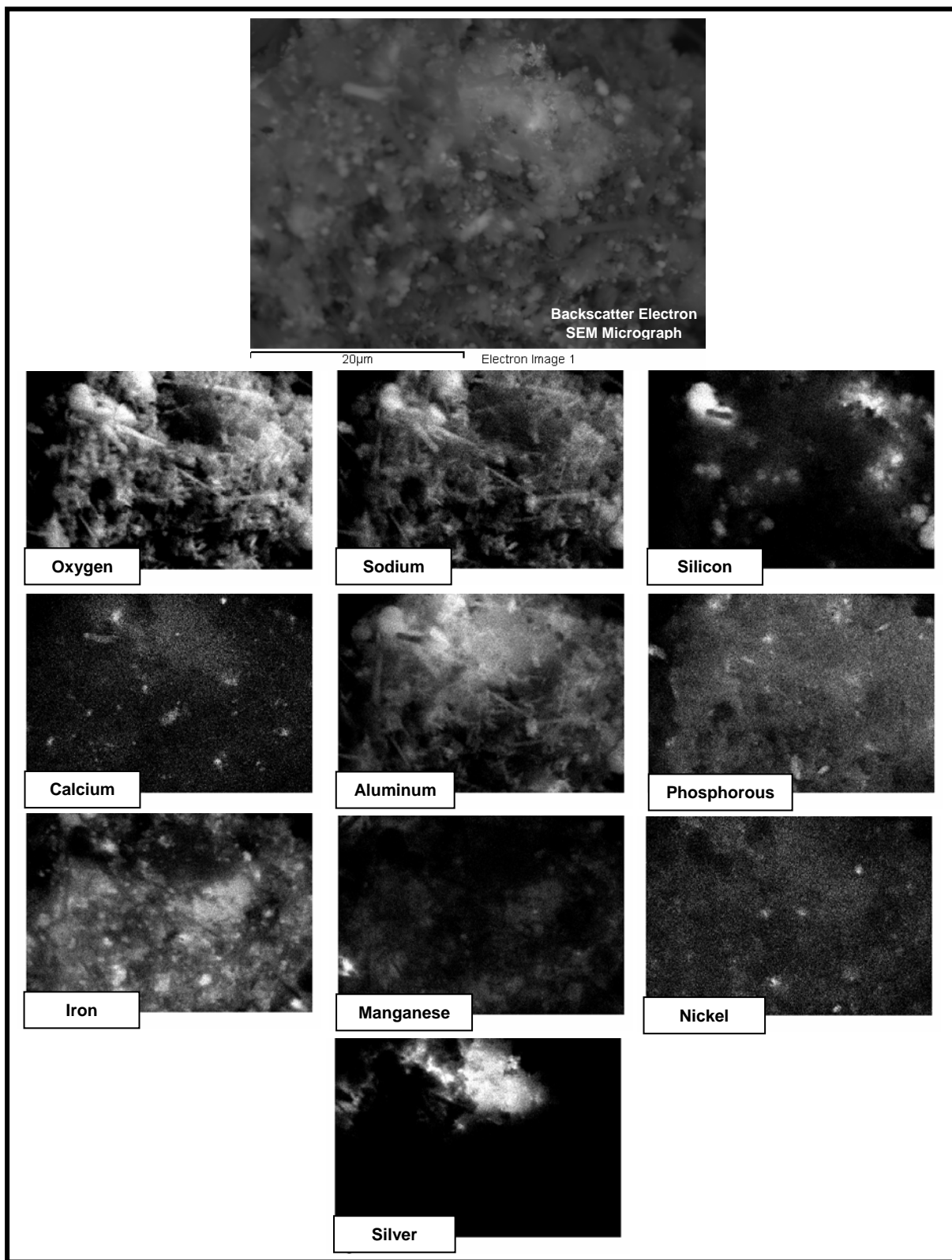
Figure 14. Higher Magnification Backscatter-Electron SEM Micrograph and Element Distribution Maps for the Area Indicated by a White Dotted-Line Rectangle in Figure 13

4.3.1.2   Residual Waste from Tank C-106

In November 2004, SEM/EDS element maps were collected for unleached, 82-day water-leached, and HF-extract samples of residual waste from tank C-106. Representative examples of these SEM/EDS element maps are presented below, but all of the recorded element maps are given in Deutsch et al. (2005). Figure 15 shows examples of colorized multi-element maps (Figure 15B to Figure 15E) for an SEM-imaged particle aggregate (Figure 15A) from an HF-extract sample of C-106 residual sludge. The maps in Figure 15 show the relationship between the presence of Ag, Hg, and Fe (Figure 15B and Figure 15D) and of Fe to Al and O (Figure 15C and Figure 15E, respectively) for this particle aggregate. These element associations are interpreted to correspond to the presence of phases (e.g., the Ag-Hg solid; hematite ─ Fe_2O_3; gibbsite ─ $Al(OH)_3$, böhmite ─ $AlO(OH)$, and/or dawsonite ─ $NaAlCO_3(OH)_2$ determined by bulk x-ray diffraction analysis (XRD) (see Deutsch et al. 2005). These results also show for the first time that there might be two Hg-containing solids where one is enriched in Ag, and the possible coexistence of Fe with the Hg-rich/Ag-poor solid. Some of the very small colored areas, such as the small green and red points in the southwest areas of Figure 15B and Figure 15D, respectively, are likely false positives resulting from overlaps in the corresponding energies of the EDS peaks.

SEM BSE micrographs and single-element distribution maps collected with the INCA system are presented in Figures 16 through 21 for SEM mounts of unleached, 82-day water-leached, and HF-extracted samples of residual waste from tank C-106. These figures include low and high magnifi-cations of particles in unleached residual waste (Figures 16 and 17, respectively), 82-day water-leached residual waste (Figures 18 and 19, respectively), and HF-extracted residual waste (Figures 20 and 21, respectively). As with the EDS element maps for the unleached AY-102 sample, the element associations indicated by the distribution maps in Figures 16 through 21 are consistent with the EDS spot analyses. The element distribution maps prepared using the INCA system did not indicate any regions in any particles in the unleached, 82 day water-leached, and HF-extracted sludge samples with detectable concentrations of [129]I, ^{99}Tc, or [238]U. The element distribution maps, however, do indicate the presence of some particles that contained Ag and Hg with detectable quantities of Cu and/or Pb. Although these two metals were sporadically detected in a few particles of tank C-106 sludge by spot EDS analyses, particles enriched in these metals had not been previously identified.
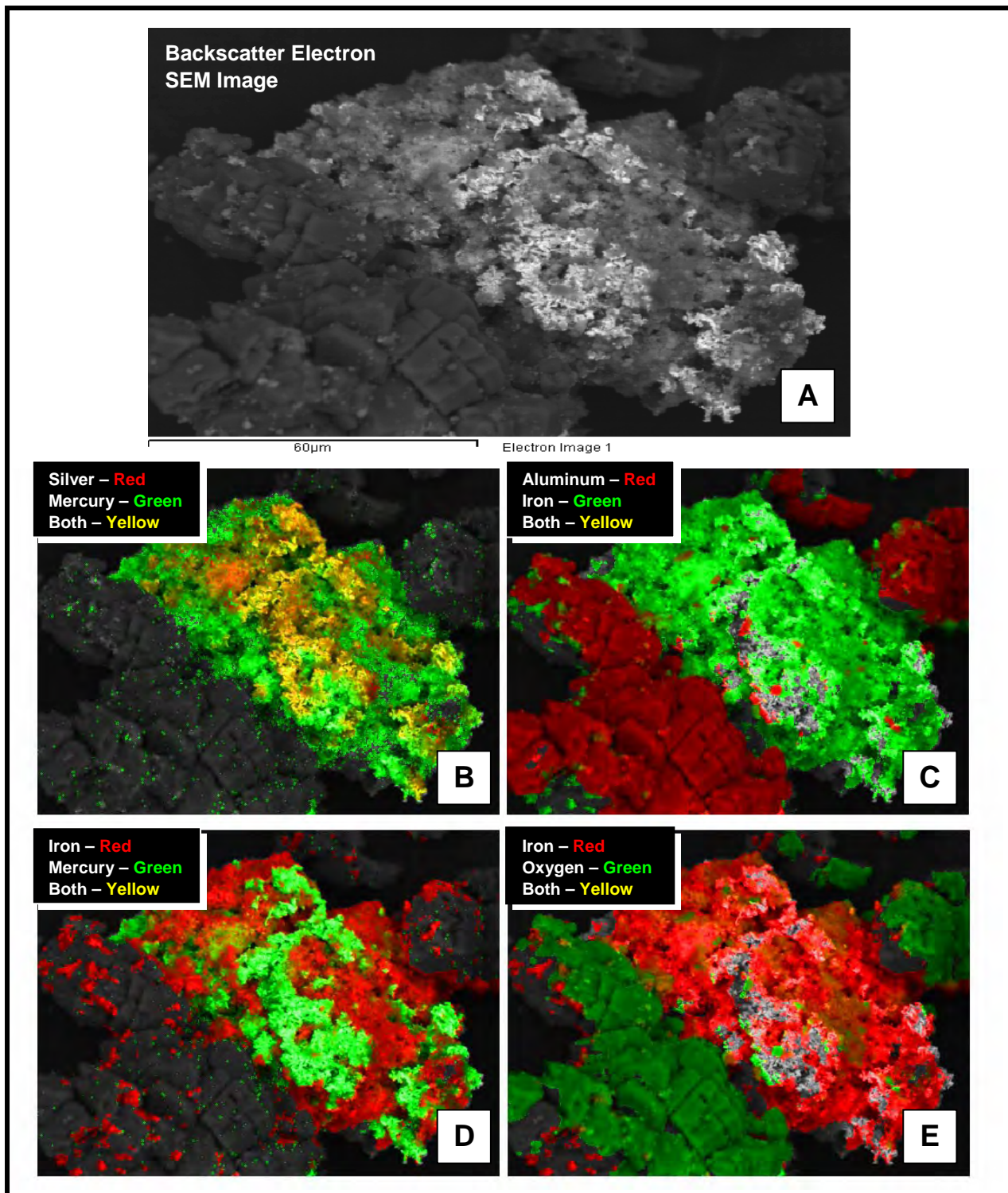
Figure 15. Backscatter-Electron SEM Image (A) and Colorized Element Maps (B through E) for a Particle Aggregate from HF Extract of C-106 Residual Waste
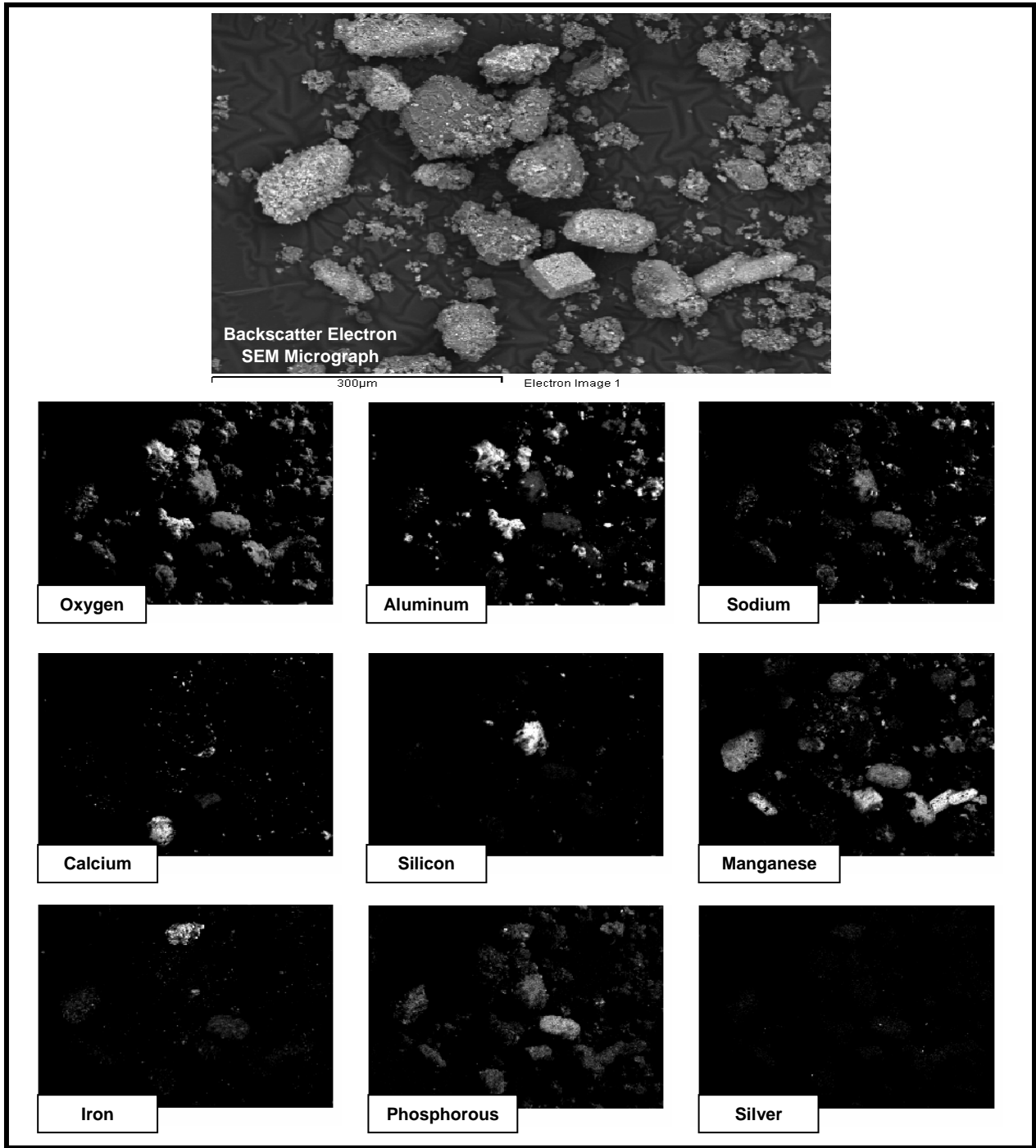
Figure 16. Low Magnification SEM BSE Micrograph and Element Distribution Maps for Particles in Unleached Residual Waste from Tank C-106
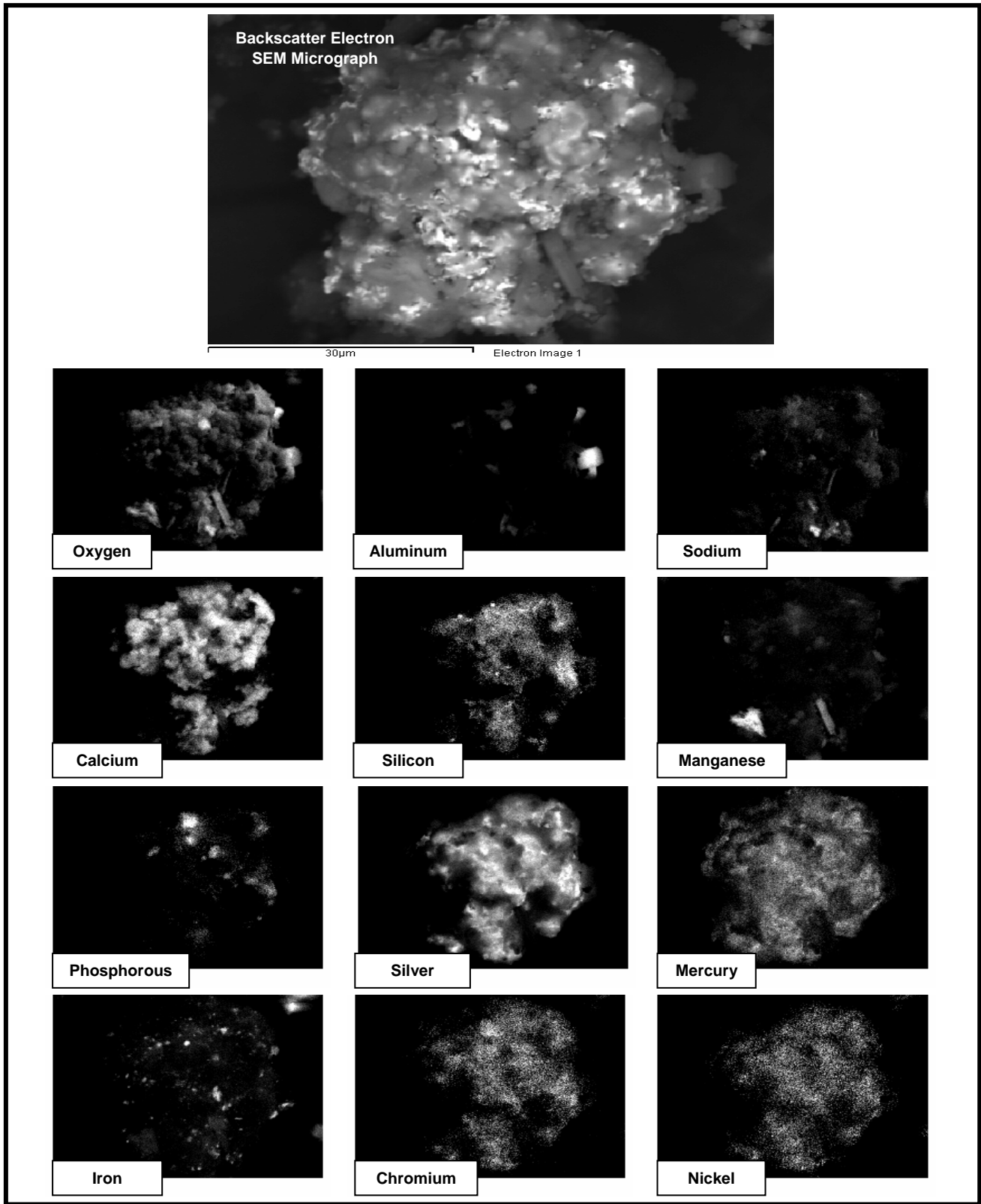
Figure 17. High Magnification SEM BSE Micrograph and Element Distribution Maps for Particles in Unleached Residual Waste from Tank C-106
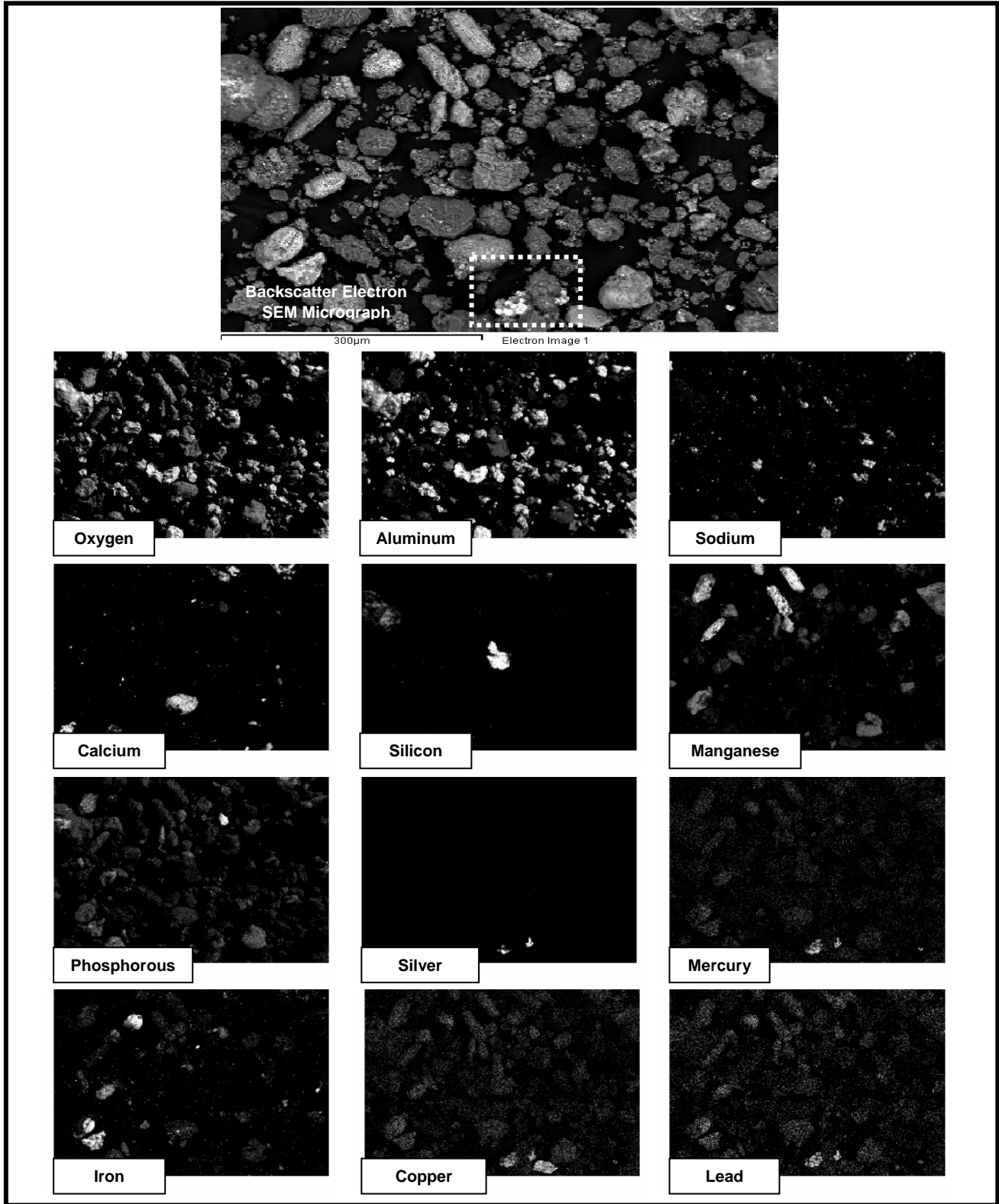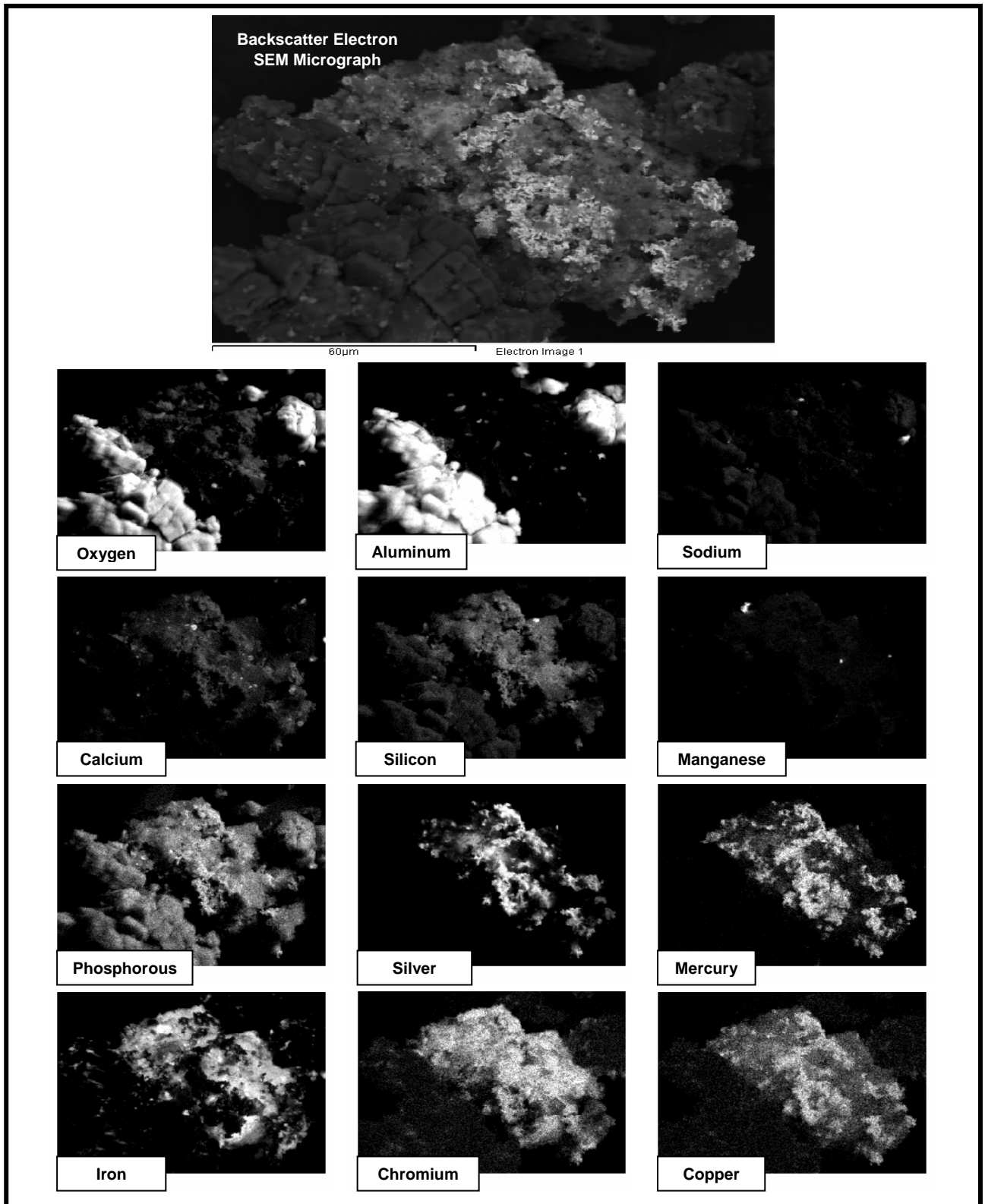
Figure 18. Low Magnification SEM BSE Micrograph and Element Distribution Maps for Particles in 82-Day Water-Leached Residual Waste from Tank C-106
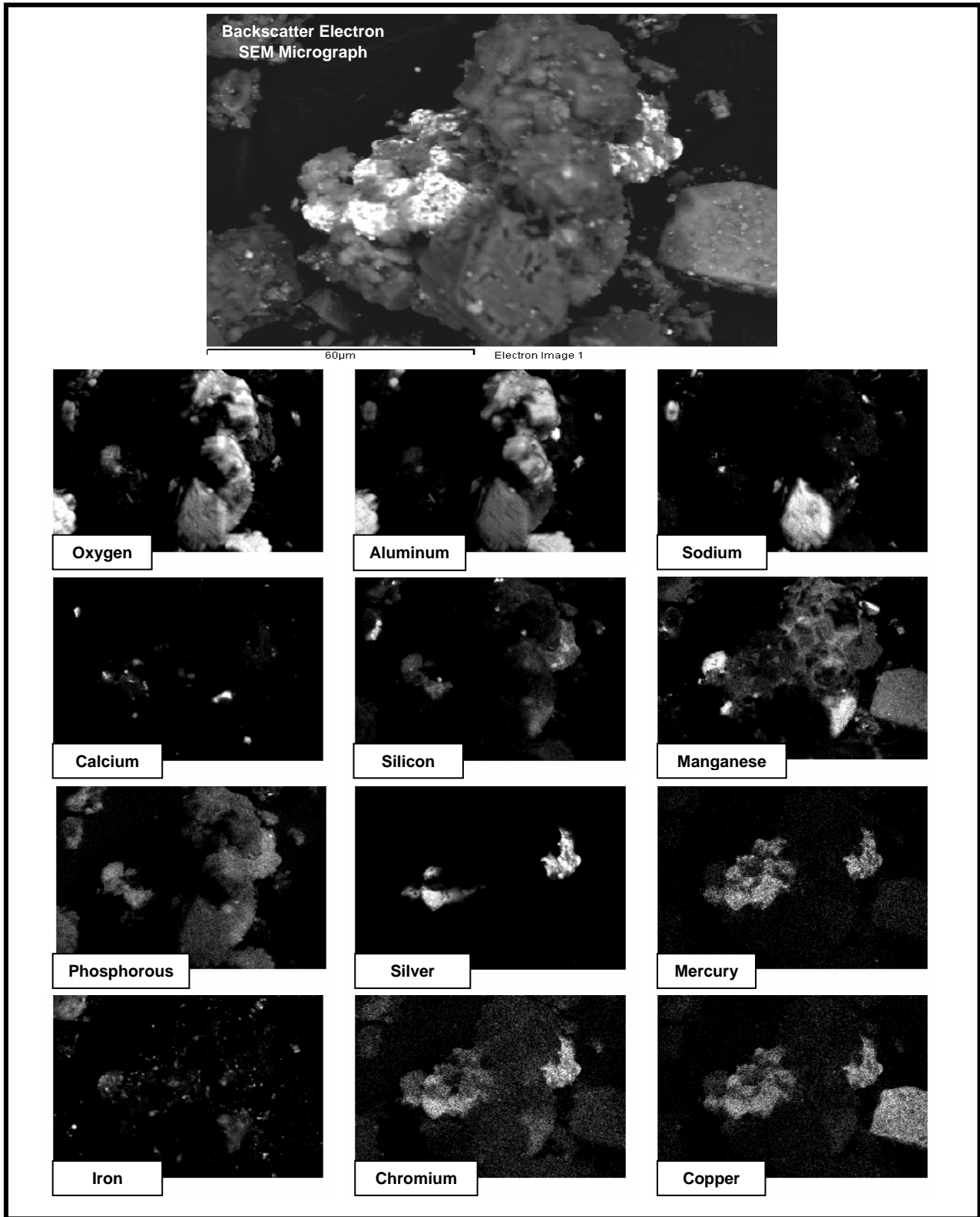
Figure 19. High Magnification SEM BSE Micrograph and Element Distribution Maps for Particles in the Area Indicated by the White Dotted-Line Rectangle in Figure 18 for 82-Day Water-Leached Residual Waste from Tank C-106
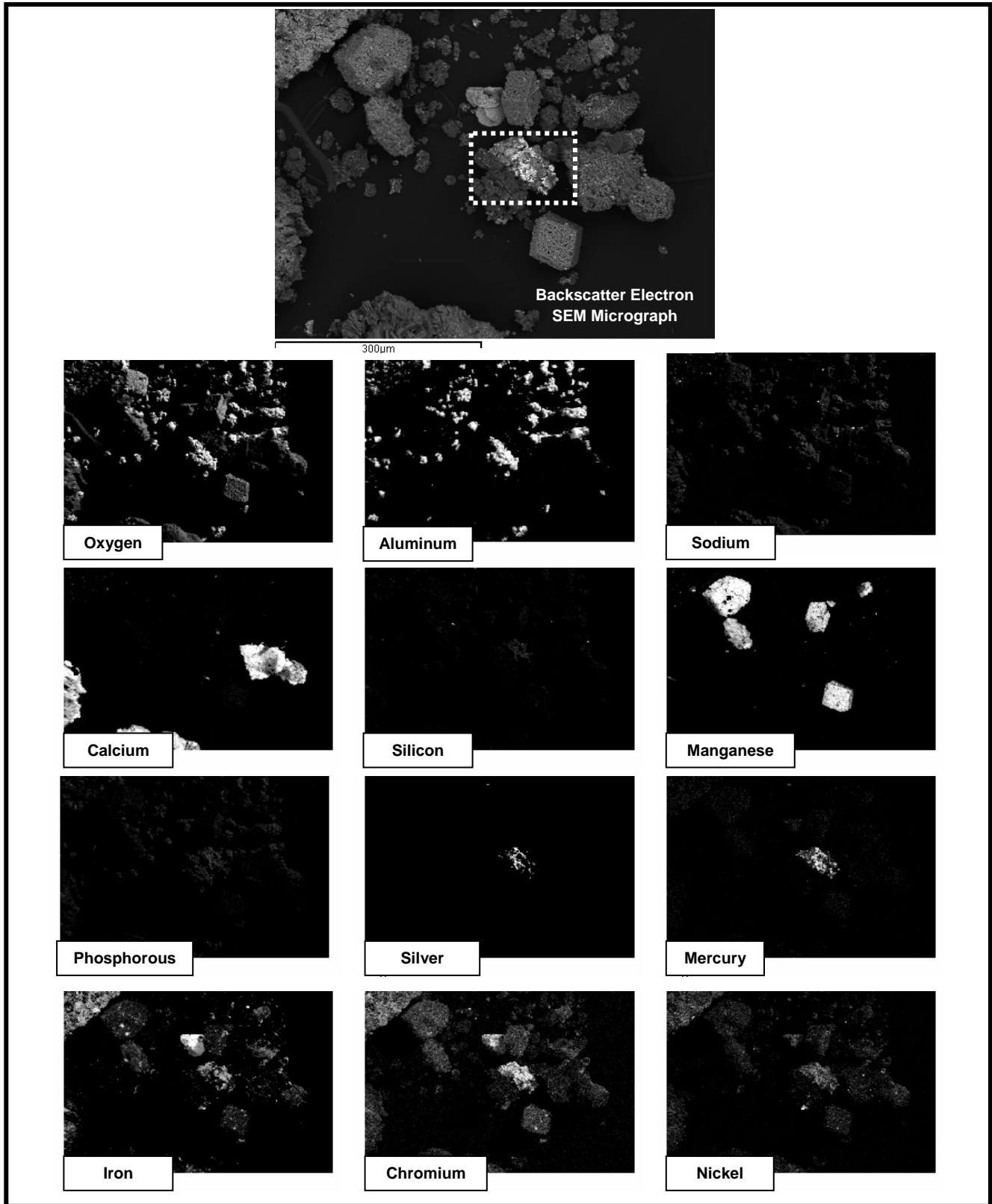
Figure 20. Low Magnification SEM BSE Micrograph and Element Distribution Maps for Particles in HF-Extracted Residual Waste from Tank C-106

Figure 21. High Magnification SEM BSE Micrograph and Element Distribution Maps for Particles in the Area Indicated by the White Dotted-Line Rectangle in Figure 20 for HF-Extracted Residual Waste from Tank C-106

4.4   Synchrotron-Based X-Ray Analysis Methods

This section describes the application of synchrotron-based methods to analyze the solid phases in tank sludge and the use of those methods on sludge from tanks C-106 and C-203.

4.4.1   Synchrotron Radiation Methods – Background

Significant advances have been made over the past two decades in the application of synchrotron radiation methods in low-temperature geochemistry and environmental sciences. These methods provide fundamental data at the molecular level on the speciation and reaction processes affecting radionuclide and contaminant behavior in aqueous solutions, amorphous and crystalline materials, solid-liquid interfaces, and complex nano-size materials. Applications of synchrotron radiation methods have increased steadily in recent years as the scientific community has become more knowledgeable of the potential of such methods. Also, access to user time for conducting studies has become easier at synchrotron sources, such the Advanced Photon Source (APS), which is a DOE general user facility located at Argonne National Laboratory (Argonne, Illinois). However, the huge cost of such facilities precludes dedicated-site facilities. Therefore, because of high user demand, researchers typically must submit proposals for finite blocks of beam time usually several months in advance, and then be willing to work around the clock to complete their experiments within the scheduled time. Prior to granting time, user proposals are typically peer reviewed by staff at the synchrotron facility with respect to technical merit and instrumentation needs. These considerations usually restrict studies using synchrotron radiation sources to narrowly focused studies for a limited set of samples, which might require several blocks of time over the course of a year or more to complete.

An extensive set of review papers and reference lists on the use of synchrotron radiation techniques in low-temperature geochemistry and environmental studies is presented in *Reviews in Mineralogy and Geochemistry, Volume 49* edited by Fenter et al. (2002). The use of synchrotron radiation methods in environmental science and related fields and their impact on environmental problems is also reviewed in *Molecular Environmental Science: An Assessment of Research Accomplishments, Available Synchrotron Radiation Facilities, and Needs* (Stanford Linear Accelerator Center 2004). Some of the synchrotron radiation methods that are useful in characterizing environmental solid and solution samples include x-ray absorption spectroscopy (XAS), x-ray microfluorescence (µXRF), and x-ray microdiffraction (µXRD)] (Brown and Sturchio 2002). X-ray absorption spectroscopy measures the absorption of x-rays by a selected element in a sample at or above that element's characteristic absorption edge energy. The x-ray absorption spectrum is generally divided into four regions: the pre-edge, the x-ray absorption near edge structure (XANES), the near edge x-ray absorption fine structure (NEXAFS), and the extended x-ray absorption fine structure (EXAFS). The near edge structure of an x-ray absorption spectrum is sensitive to the oxidation state and coordination of the absorbing atom, whereas the extended fine structure spectrum provides quantitative information on the number and chemical identities of the near-neighbor atoms and their average interatomic distances out to about 5 to 6 Å.

There are numerous special features of radiation from synchrotron sources that result in the successful application of x-ray analytical methods to analyses of environmental samples. The x-ray energy is easily tunable, a necessary property for x-ray absorption spectroscopy. Radiation from synchrotron sources is highly linearly polarized in the plane of the synchrotron ring. This characteristic produces reduced background from Rayleigh and Compton scattering of the synchrotron beam compared to that from x-ray

tube sources. Synchrotron radiation is also well collimated, which permits the x-ray beams to be focused on areas of a sample ranging from a few hundreds of nanometers to a few millimeters in size. Most importantly, the intensity (or "brightness") of the synchrotron radiation is several orders of magnitude greater than the fixed energy radiation from the characteristic lines of a standard x-ray tube. The advantage is even greater when compared to the continuum radiation from a tube. This high photon flux reduces the time required for measurements, and provides a high sensitivity to better than parts per million level in most cases. Because the x-ray beams can be concentrated into narrow energy bands which can be adjusted by varying the magnetic field, detection of a particular element can be selected by changing the energy band to just above the element's absorption edge. These properties of synchrotron radiation permit XAS to be combined with µXRD and µXRF analyses for studies of environmental samples at the micrometer to submicrometer scale.

4.4.2 Synchrotron-Based X-Ray Analysis of Tank C-203 Water-Leached Residual Waste

Approach for Tank C-203 Water-Leached Sample. After the completion of the studies by Deutsch et al. (2004) of residual waste from tanks C-203 and C-204, a study of limited scope was done to assess the feasibility of using synchrotron-based µXRD to help identify one of the U-containing phases present in the C-203 residual waste. This phase could not be positively identified by bulk XRD but was thought to be poorly crystalline Na uranate ($Na_2U_2O_7$) or clarkeite $\{Na[(UO_2)O(OH)](H_2O)_{0-1}]\}$. X-ray micro-diffraction was used to collect diffraction patterns on ~5-µm diameter areas of relatively large (approxi-mately 20 to 100 µm), U-rich regions that were located from x-ray fluorescence mapping using a sample of two-week, water-leached C-203 residual waste. Sample mounts were prepared using Kapton® tape with acrylic adhesive and Kapton® film. A 2.54-cm square piece of the tape was placed flat with the adhesive side up. Approximately 1 mg of dried C-203 residual waste was then sprinkled onto the center of the tape attempting to cover an area of a few square millimeters with a monolayer of particles. After the particles were spread on the tape, Kapton® film was placed on top of the sample so that the film adhered to the tape. Secondary containment of the sample was then achieved by placing the sample between two more pieces of Kapton® film and then securing the edges with Kapton® tape.

Large particles containing high U concentrations were first located in the sample mount by using microscanning x-ray fluorescence (µSXRF). µSXRF mapping was performed on the taped sample mount using a focused x-ray beam on APS beamline ID-20 (PNC-CAT) (Heald et al. 2001). Focusing of the x-ray beam to a spot size of 5 µm × 5 µm was accomplished using a pair of Kirkpatrick-Baez mirrors, and the incident beam was monochromatized using a Si(111) double-crystal monochromator. A multi-element Ge detector was used to map the distributions of U, Fe, and Pb.

The µXRD patterns were collected on the high U-containing areas in transmission geometry using an x-ray beam with an incoming wavelength of 0.7293 Å and phosphor image plates 20x40 cm in size. The image plates were located approximately 20 cm from the sample, and were read using a Fuji BAS-2500 scanner (Fujifilm Medical Systems U.S.A., Inc., Stamford, Connecticut). The resulting images were processed using FIT2D (Hammersley 1997). The sample-to-detector distance and geometric corrections were calculated from patterns obtained from Si powder. After these corrections were applied, the two-dimensional (2D) images were integrated radially to yield one-dimensional (1D) powder diffraction patterns that could then be analyzed using standard techniques. The Kapton® mount generated significant background scattering and a sharp peak at ~10°2θ. Initial background removal was accomplished by

subtracting a scaled-background pattern from an area with no sample diffraction, but which did include the peak at $\sim$10°2θ contributed by the Kapton® film. Further background subtraction was performed using the JADE® 6.5 software. Identification of the solid phases in the background-subtracted patterns was based on a comparison of the μXRD patterns with the diffraction patterns in the JCPDS-ICDD database.

Results for Tank C-203 Water-Leached Samples. A synchrotron focused x-ray beam was used to collect transmission μXRD patterns on five $\sim$5-μm diameter areas (see spots labeled 1 through 5 in Figure 22) of relatively large (approximately 20 to 100 μm), concentrated U-containing particles. Figures 22 through 24 show the distributions of the relative concentrations of U, Fe, and Pb, respectively, as determined by μSXRF. The scale bar on the right side of Figures 22 through 24 represent the output signal for the indicated element divided by 10, and without some sort of calibration, are regarded as arbitrary units. The concentration of the indicated element increases as the colors in these figures change from dark blue through green and yellow to dark red. Only one of these five μXRD patterns (spot 4 in Figure 22) contained adequate reflections that were suitable for phase identification. Spot 4 is from a U-rich particle sitting on top of a larger Fe-rich region.

The transmission μXRD pattern for spot 4 is shown in Figure 25. The μXRD patterns for spots 1 and 2 did not show any reflections, which indicates that the solid material in these areas was amorphous. The reflections in the patterns for spots 3 and 5 after background subtraction were too weak and/or too board, which prevented identification of any phases in these patterns, but also suggested the presence of a significant quantity of amorphous material. Figure 26 shows the scan trace versus 2θ calculated based on an incoming wavelength of 0.7293 Å and intensities of the reflections in μXRD pattern for spot 4 (Figure 25). The reflections in the background-subtracted pattern for spot 4 match well with the database patterns (colored lines) for goethite [α-FeO(OH)] (PDF 29-0713), maghemite (γ-Fe$_2$O$_3$) (PDF 39-1346), and the Na-uranates clarkeite (PDF 50-1586) and/or Na$_2$U$_2$O$_7$ (PDF 43-0347). Identification of the Fe oxides is consistent with the μSXRF map for Fe, which showed Fe-rich concentrations in the region surrounding spot 4. Goethite and maghemite were not identified in the "bulk" XRD analysis (based on $\sim$1-cm^2 irradiated areas) of the bulk solid, but their identification is consistent with SEM/EDS analyses that revealed the presence of Fe oxides in this residual waste. Although the μXRD pattern for spot 4 is consistent with the presence of a Na uranate, it was not possible from this pattern to distinguish between clarkeite and Na$_2$U$_2$O$_7$, because as noted previously, these two phases are isostructural and have similar XRD patterns. Based on the height of the reflections in the μXRD pattern, the material at spot 4 likely contains a larger mass of Fe oxides than Na uranate. The sharp peak at $\sim$10°2θ corresponds to diffraction produced by the Kapton® mount.

71
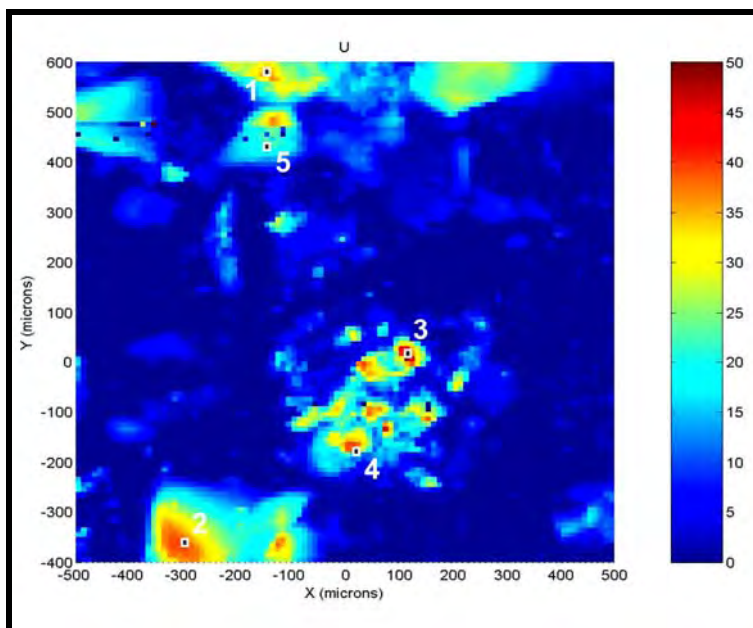
Figure 22. μSXRF Map Showing the Distribution of U Concentrations and the Locations Where the Five μXRD Patterns (black-filled squares at locations marked 1 through 5) were Collected
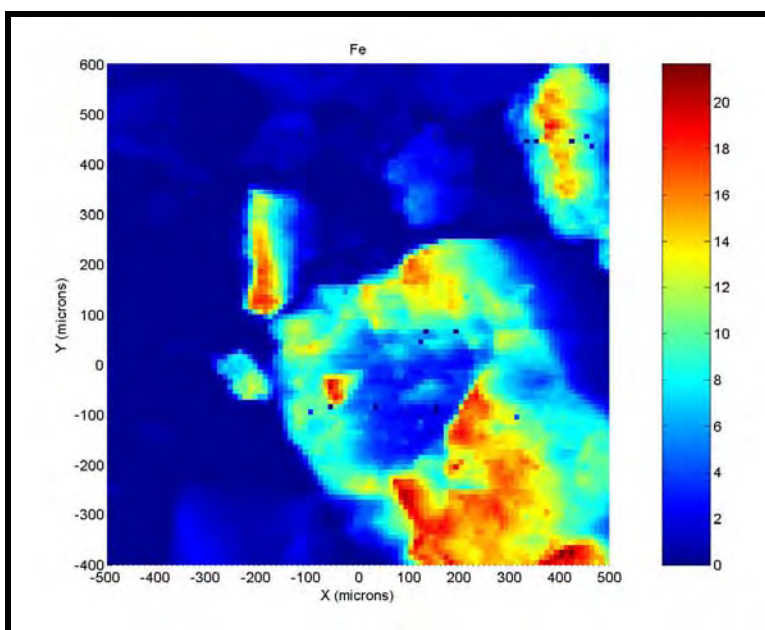
Figure 23. μSXRF Map Showing the Distribution of Fe Concentrations for the Sample Area Where the Five μXRD Patterns were Collected
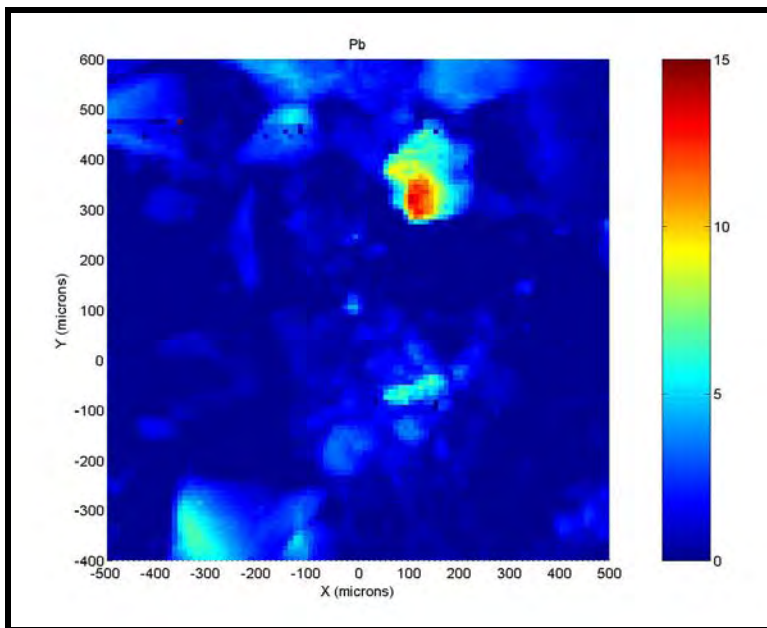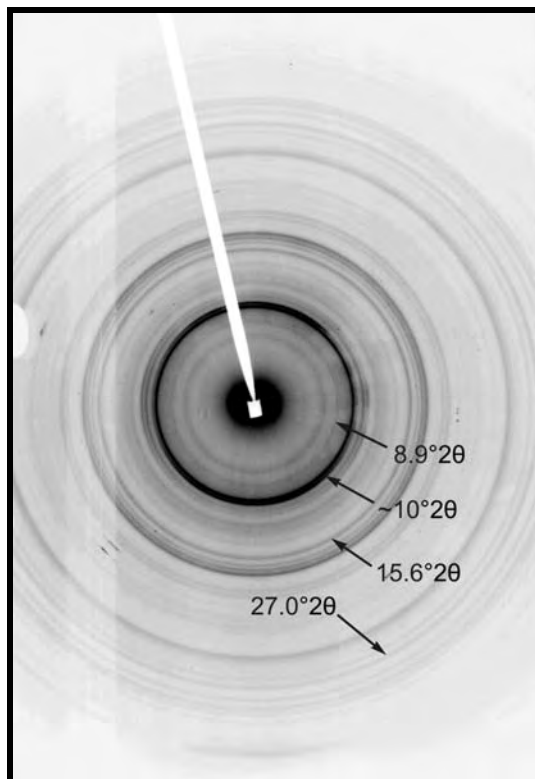
Figure 24. µSXRF Map Showing the Distribution of Pb Concentrations for the Sample Area Where the Five µXRD Patterns were Collected

Figure 25. µXRD Pattern (incoming wavelength of 0.7293 Å) for Spot 4 (~5-µm Diameter Area) for a U-Rich Region Identified from µSXRF Mapping (The darker the line, the higher the diffracted intensity in this gray-scale image. Two-theta values added for arbitrarily selected reflections to provide scale for the µXRD pattern.)
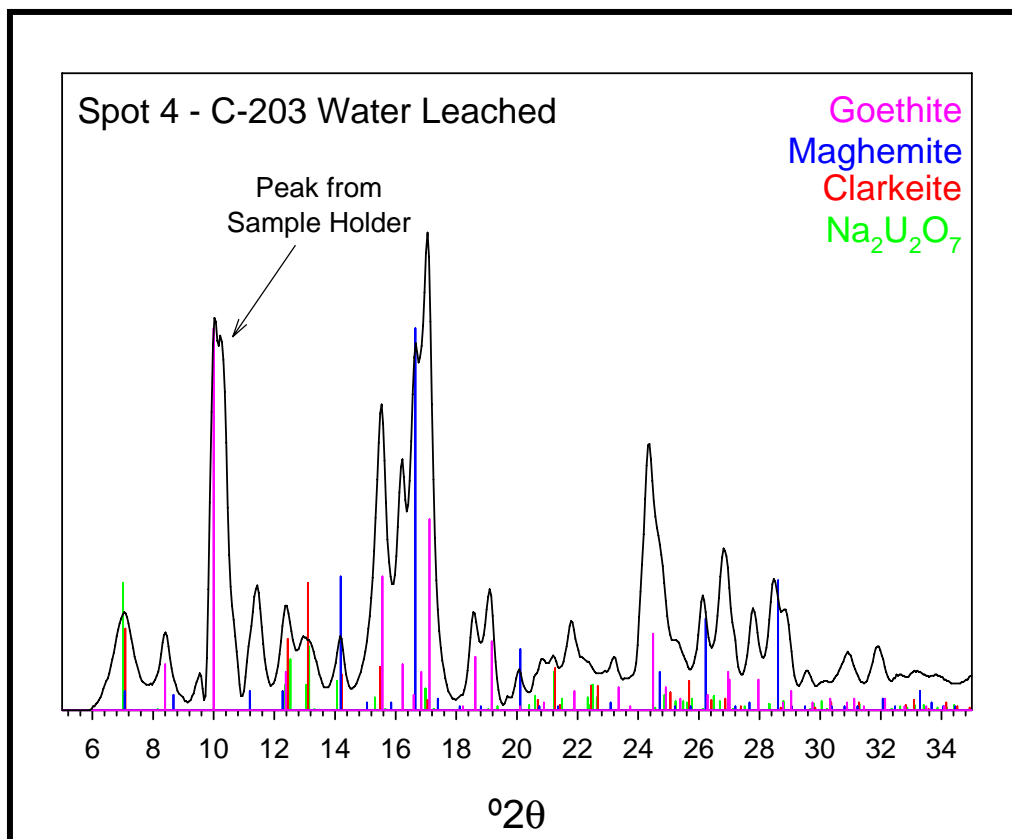
Figure 26. Scan Trace versus 2θ Calculated Based on an Incoming Wavelength of 0.7293 Å and Intensities of the Reflections in the Transmission μXRD Pattern for Spot 4 and Compared to the Corresponding Reflections (Colored Lines) from the Database Patterns for Goethite, Maghemite, Clarkeite, and $Na_2U_2O_7$

4.4.3   Synchrotron-Based X-Ray Analysis of Tank C-106 Residual Waste

Synchrotron techniques were used to study residual water from tank C-106 and the same material after water leaching six times sequentially over a period of 90 days. μXRF, XAS, and μXRD were used to investigate the applicability of these techniques for determining phase associations and speciation of contaminants of concern (^{99}Tc, ^{129}I, ^{90}Sr, Cr, and ^{238}U).

Approach for Tank C-106 Residual Waste. Sample mounts for the tank C-106 material were prepared in the same manner as that described previously for tank C-203 material. Analysis of each of the samples began with a μSXRF map of an area of approximately 1×1.5 mm to locate particles with high concentrations of the major component metals Fe, Mn, and Ag and the contaminants ^{99}Tc, ^{129}I, Cr, ^{90}Sr, and ^{238}U. μSXRF mapping was performed on the taped sample mounts using a focused x-ray beam on beamline ID-20 (PNC-CAT) (Heald et al. 2001) at the Advanced Photon Source. Focusing of the x-ray beam to a spot size of 5×5 μm was accomplished using a pair of Kirkpatrick-Baez mirrors, and the incident beam was monochromatized using a Si(111) double-crystal monochromator. A multi-element Ge detector was used to map the distributions of the elements of interest.

74

Locations of interest for further analysis by XAS were generally selected based on high concentrations of contaminants of concern and their associations with major component metals. The XANES and the EXAFS were examined to determine the oxidation state of the element of interest and when possible the speciation of the element based on the coordination of the absorbing atom. Subsequent to the XAS analysis a number of locations were selected for µXRD analysis. The patterns were collected, corrected, and interpreted in the same manner as that described previously for the tank C-203 samples.

Tank C-106 Residual Waste Results: µSXRF Maps for C-106 Unleached Sample. The µSXRF map for Ag in the tank C-106 unleached sample is shown in Figure 27. Some of the locations which were selected for more detailed analysis by µXRF, X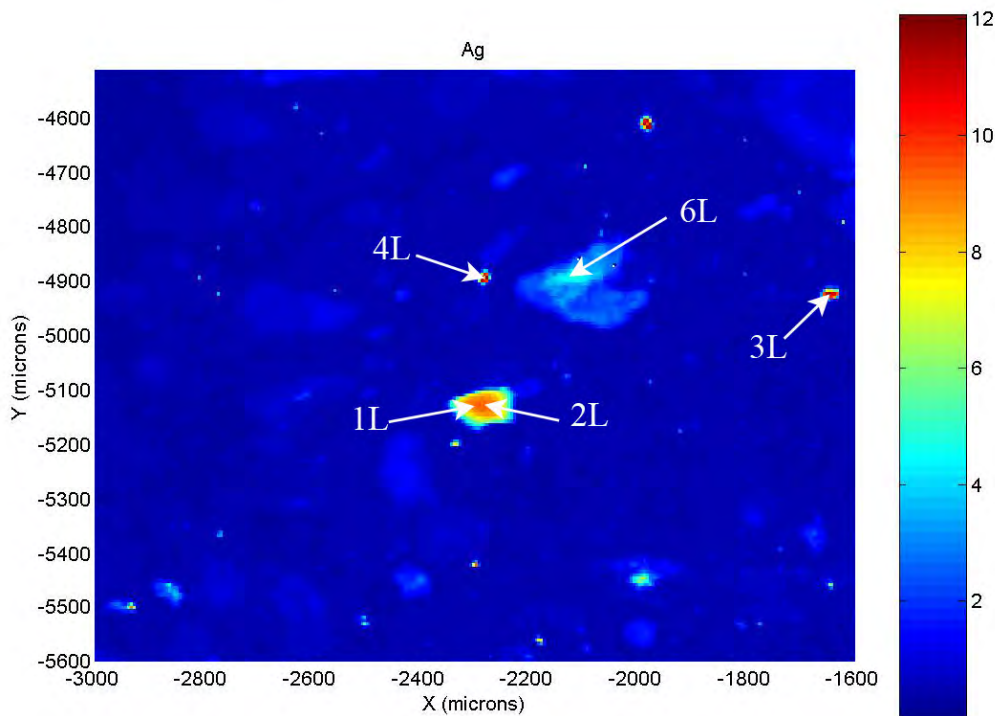AS and µXRD are indicated by arrows and numbers. The scale-bar to the right of Figure 27 and the other µSXRF maps illustrated in the paper show the relative concentration distributions for the element of interest. These images have been corrected for peak overlaps such as the Mn K_β contribution to Fe, and the overlap of the U and Rb peaks. However, this scale bar must be regarded as arbitrary units because calibration was not done for these scans. For the elements with high energy lines (U, Sr, and Ag), the relative signal levels can be taken as approximate relative concentrations. Note that the sizes of the Ag-containing particles are relatively small. This is consistent with the sizes of Ag particles observed with SEM (Deutsch et al. 2004).
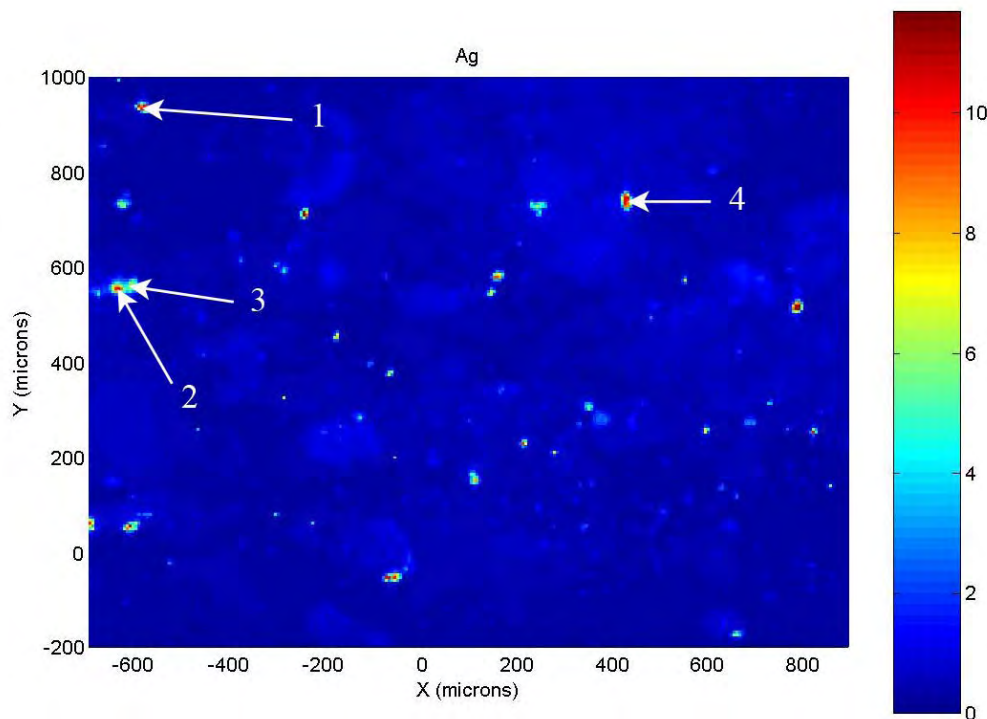
Figure 27. µSXRF Map for Ag in the Tank C-106 Unleached Sample. (Some locations selected for more detailed analysis by µXRF, XAS and µXRD are indicated by arrows and numbers.)

The μSXRF map for Mn in the tank C-106 unleached sample is shown in Figure 28. The size of the Mn-containing particles are similar in size and shape to that of the Fe-containing particles (Figure 29) and are consistent with the size of particles observed in SEM images of tank C-106 unleached tank waste.
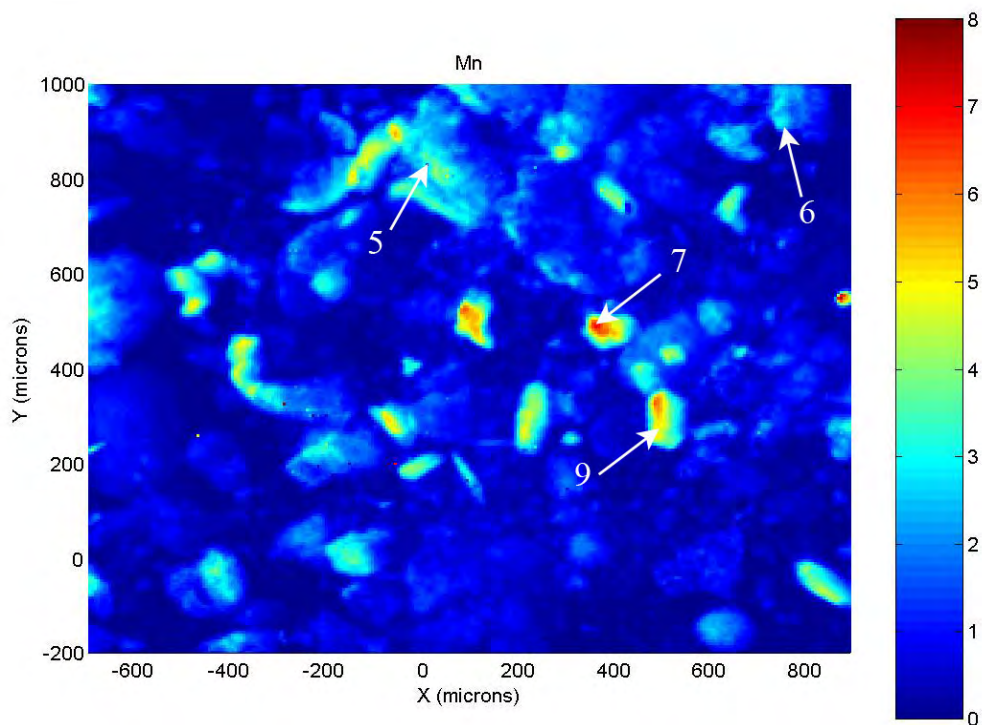
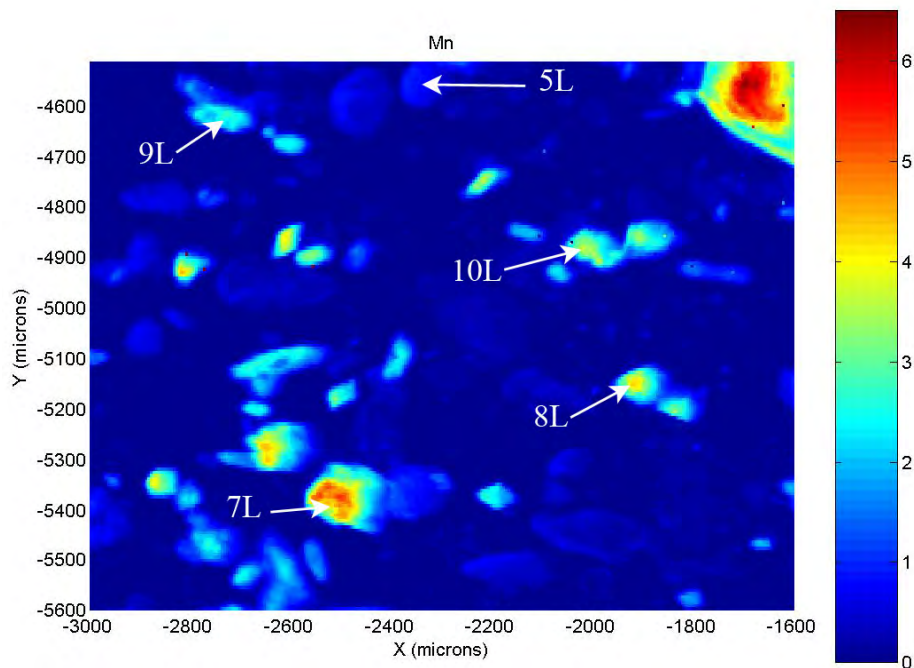**Figure 28**.   μSXRF Map for Mn in the Tank C-106 Unleached Sample. (Locations selected for more detailed analysis by μXRF, XAS and μXRD are indicated by arrows and numbers.)

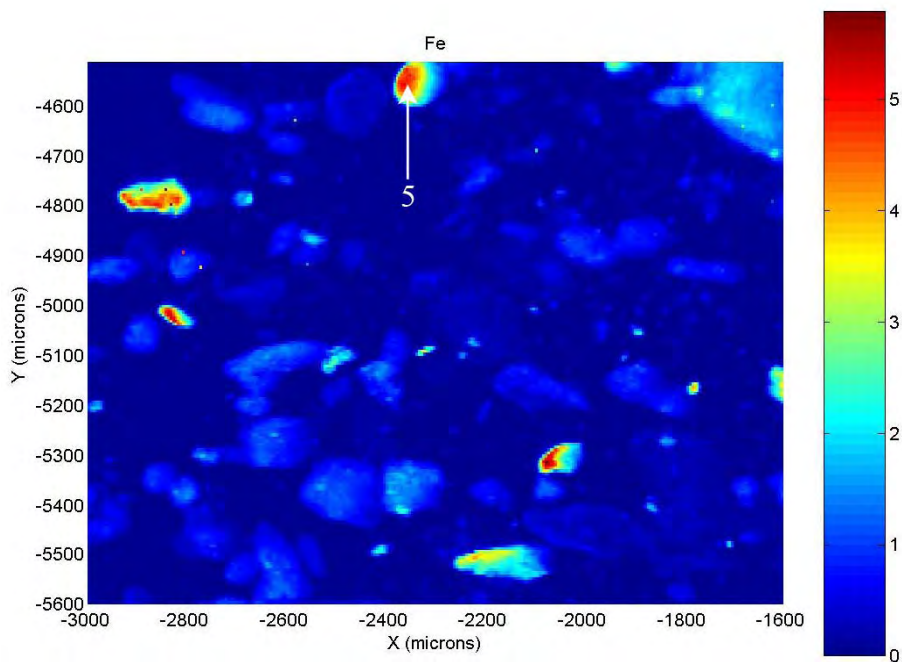The μSXRF map for Fe in the tank C-106 unleached sample is shown in Figure 29. The size of the Fe-containing particles are much larger than those of the Ag particles and are consistent with the size of particles observed in SEM images of tank C-106 unleached tank waste.
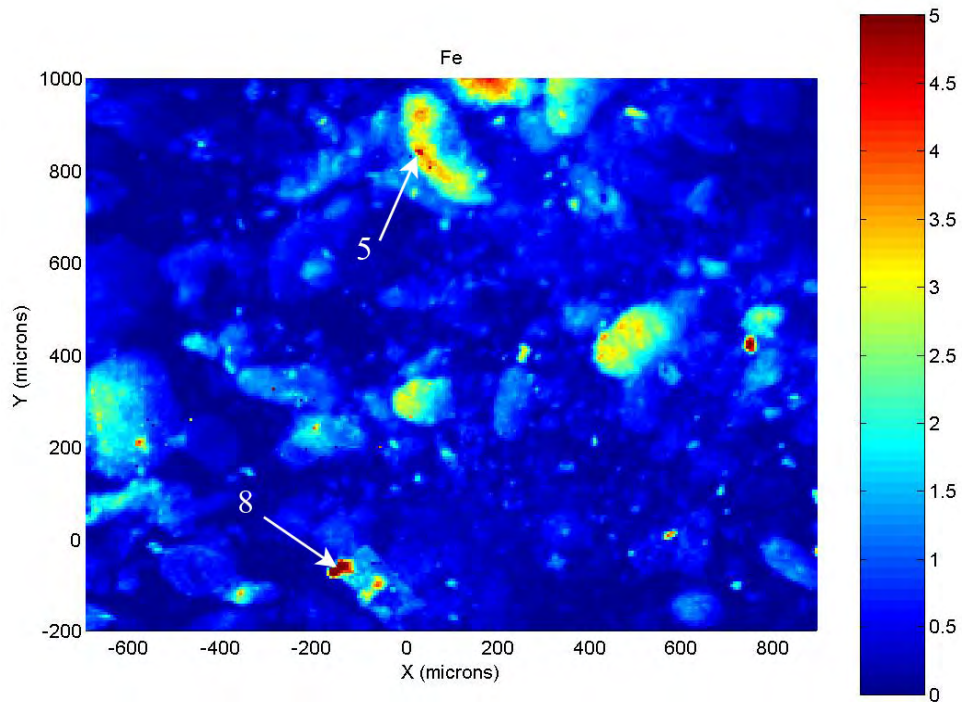
Figure 29. µSXRF Map for Fe in the Tank C-106 Unleached Sample. (Locations selected for more detailed analysis by µXRF, XAS and µXRD are indicated by arrows and numbers.)

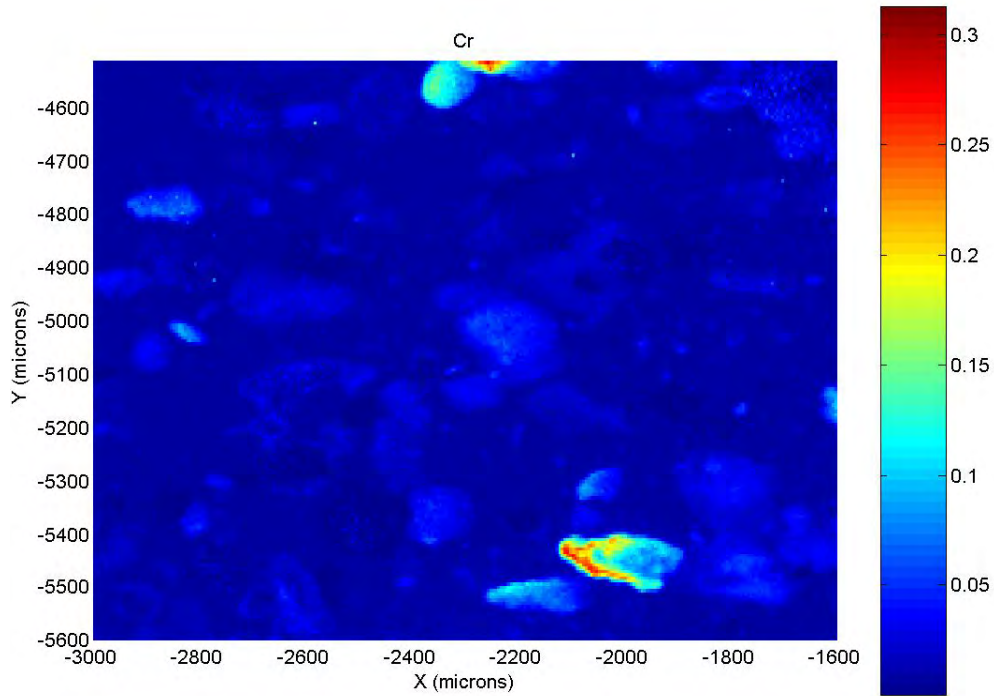The µSXRF map for Cr in the tank C-106 unleached sample is shown in Figure 30.
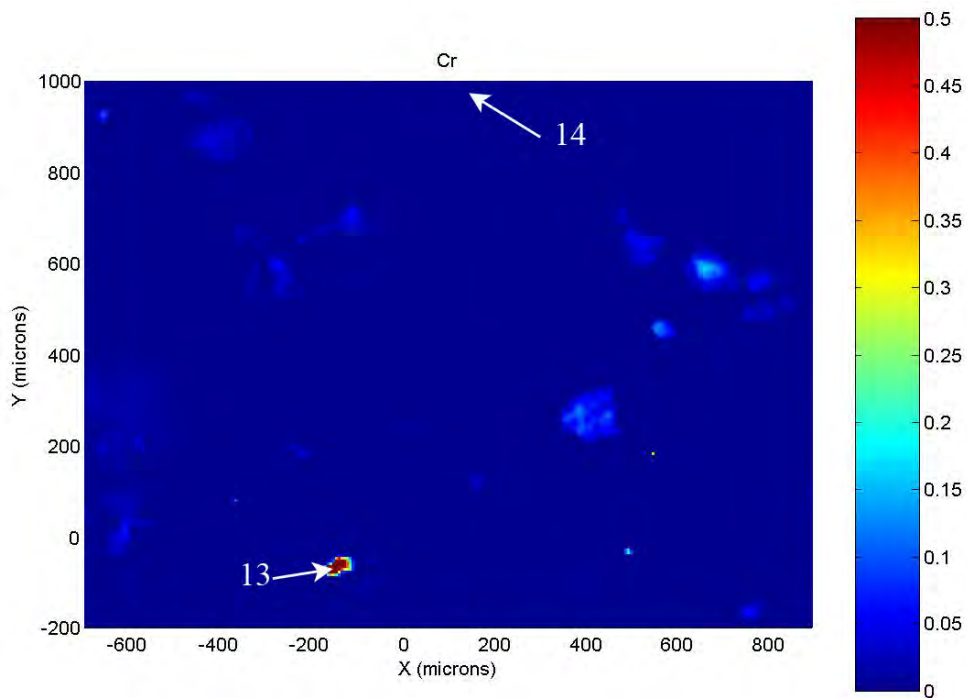
Figure 30. µSXRF Map for Cr in the Tank C-106 Unleached Sample

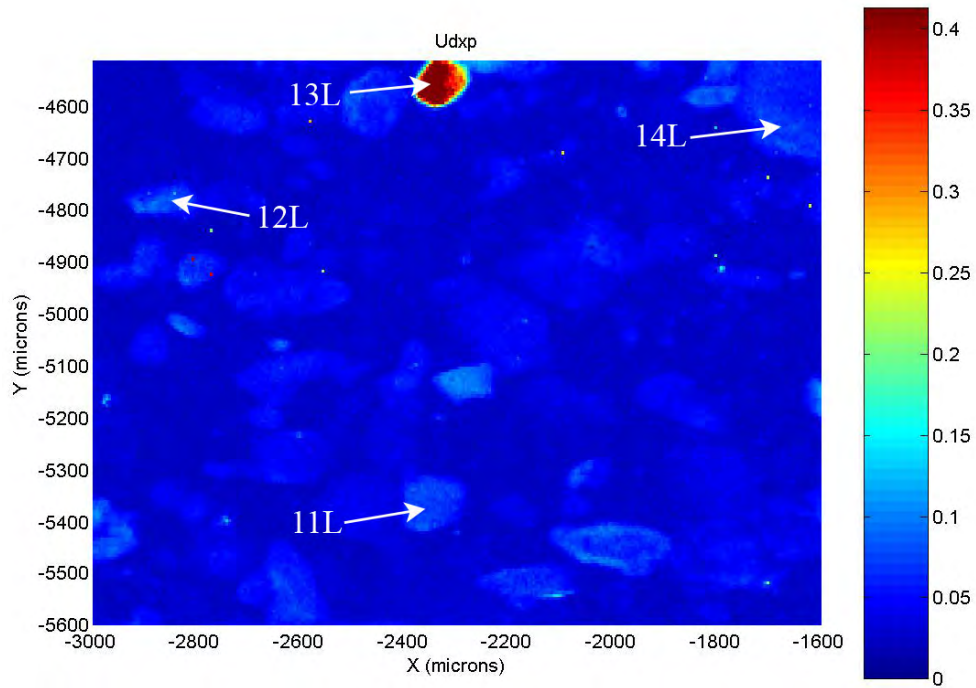The μSXRF map for U in the tank C-106 unleached sample is shown in Figure 31.
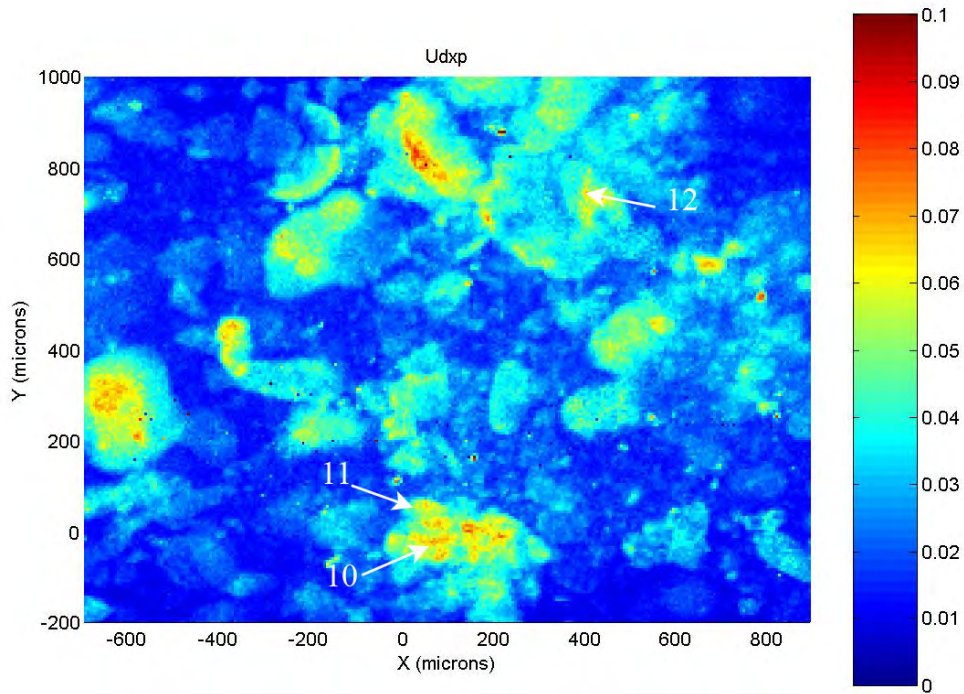
Figure 31. μSXRF Map for U in the Tank C-106 Unleached Sample

The μSXRF map for Sr in the tank C-106 unleached sample is shown in Figure 32.
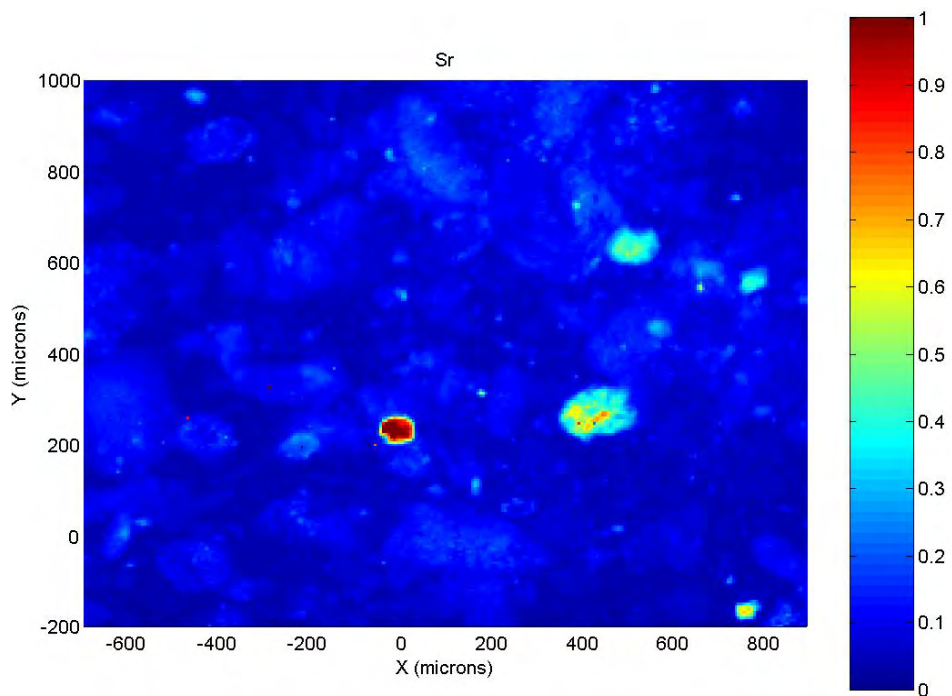
Figure 32. μSXRF Map for Sr in the Tank C-106 Unleached Sample

µSXRF maps for I and Tc are not shown. The scan for I in the C-106 unleached sample was not useful because of a small signal-to-noise ratio for the low energy peaks of this element due to the Kapton containment, and large interferences from the calcium peaks. Technetium was undetectable due to low concentrations.

Tank C-106 Residual Waste Results: µSXRF Maps for C-106 Unleached Sample. The µSXRF map for Ag in the C-106 water-leached sample is shown in Figure 33. Some locations which were selected for more detailed analysis by µXRF, XAS and µXRD are indicated by arrows and numbers.

Figure 33.   µSXRF Map for Ag in the Tank C-106 Water-Leached Sample. (Some locations selected for more detailed analysis by µXRFD, XAS and µXRD are indicated by arrows and numbers.)

The µSXRF map for Mn in the tank C-106 water-leached sample is shown in Figure 34. Some locations selected for more detailed analysis by µXRFD, XAS and µXRD are indicated by arrows and numbers.

Figure 34. µSXRF Map for Mn in the Tank C-106 Water-Leached Sample. (Locations selected for more detailed analysis by µXRF, XAS and µXRD are indicated by arrows and numbers.)

The µSXRF map for Fe in the tank C-106 water-leached sample is shown in Figure 35.

Figure 35. µSXRF Map for Fe in the Tank C-106 Water-Leached Sample. (Locations selected for more detailed analysis by µXRF, XAS and µXRD are indicated by arrows and numbers.)

The μSXRF map for Cr in the tank C-106 water-leached sample is shown in Figure 36.

Figure 36. μSXRF Map for Cr in the Tank C-106 Water-Leached Sample

The μSXRF map for U in the C-106 water-leached sample is shown in Figure 37.

Figure 37. μSXRF Map for U in the Tank C-106 Water-Leached Sample

The μSXRF map for Sr in the C-106 water-leached sample is shown in Figure 38. The coincidence of the area of very high Sr concentrations in the upper center of Figure 38 with that of U in the same location (Figure 37), suggests that this particle could be a spent fuel particle; however, it was not possible to confirm this conjecture.
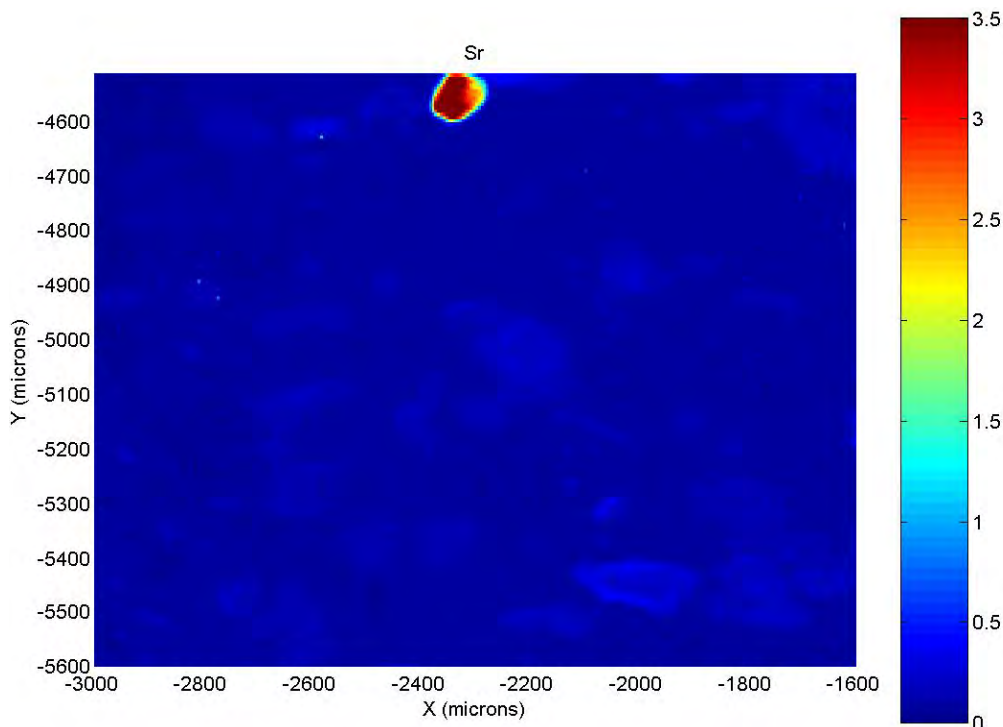
Figure 38. μSXRF Map for Sr in the Tank C-106 Water-Leached Sample

As with the unleached C-106 sample, μSXRF maps for I and Tc from the water-leached C-106 sample are not shown. The μSXRF map for I in the C-106 water-leached sample was not useful because of a small signal-to-noise ratio for the low energy peaks of this element and large interferences from the calcium peaks. Technetium was undetectable due to low concentrations.

Results and Discussion of μXRF and XAS Analysis Results for C-106 Residual Waste. The μSXRF maps of the unleached and leached tank C-106 samples shown in Figure 27 and Figure 33 indicate that the majority of the silver occurs as small discreet particles. XANES and EXAFS spectra collected from four locations within the unleached C-106 residual waste sample that contained high concentrations of Ag are shown in Figure 39, along with standard results for Ag and AgI. Similar results for the C-106 water-leached sample are shown in Figure 40. The sample locations for the spectra shown in Figures 39 through 45 are referred to by spot number (see Figures 27 through 38). The results for both samples indicate that the majority of the Ag is in the zero-valent (metallic) form. The shift of some of the edges to higher energies also suggests that some of the Ag is in a more oxidized form which was not identified. AgO and $AgNO_3$ are examples of other compounds that could potentially exit in the sludge. Although not imaged in the original scans, it was also determined from near edge scans that smaller amounts of zero-valent Hg frequently occurred with the Ag.
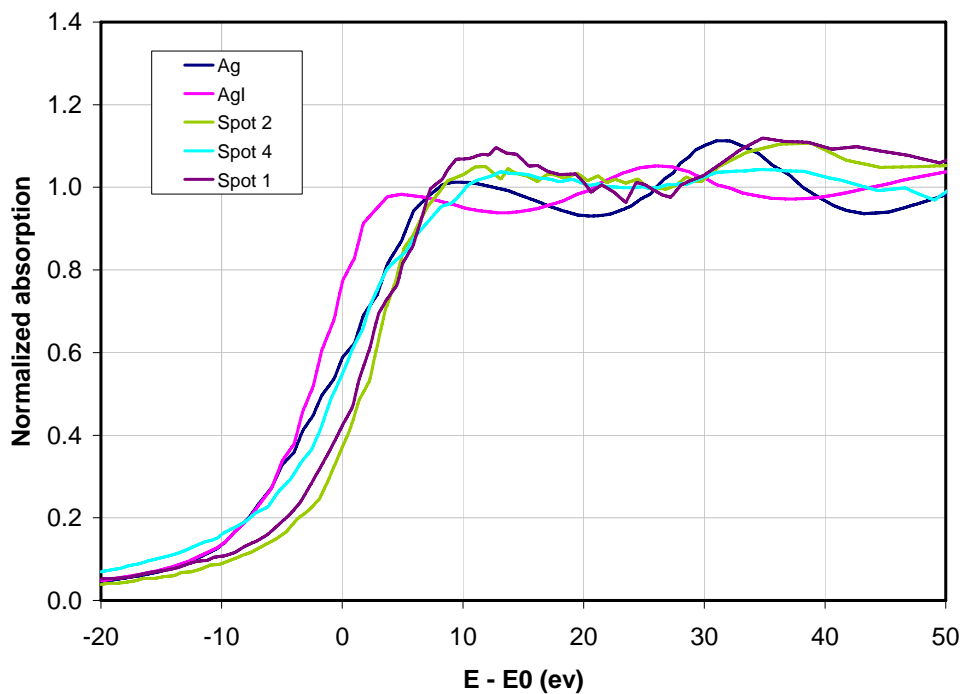
Figure 39. XANES and EXAFS Spectra Collected from Three Locations Within the Unleached Tank C-106 Residual Waste Sample that Contained High Concentrations of Ag. (Standard results for Ag^0 and AgI are also included.)
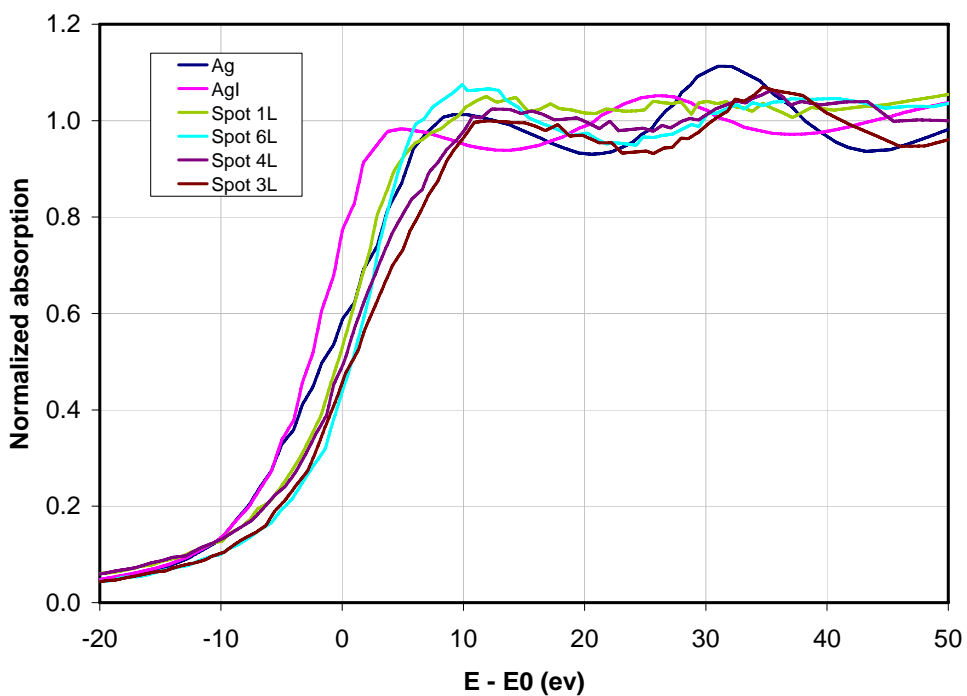

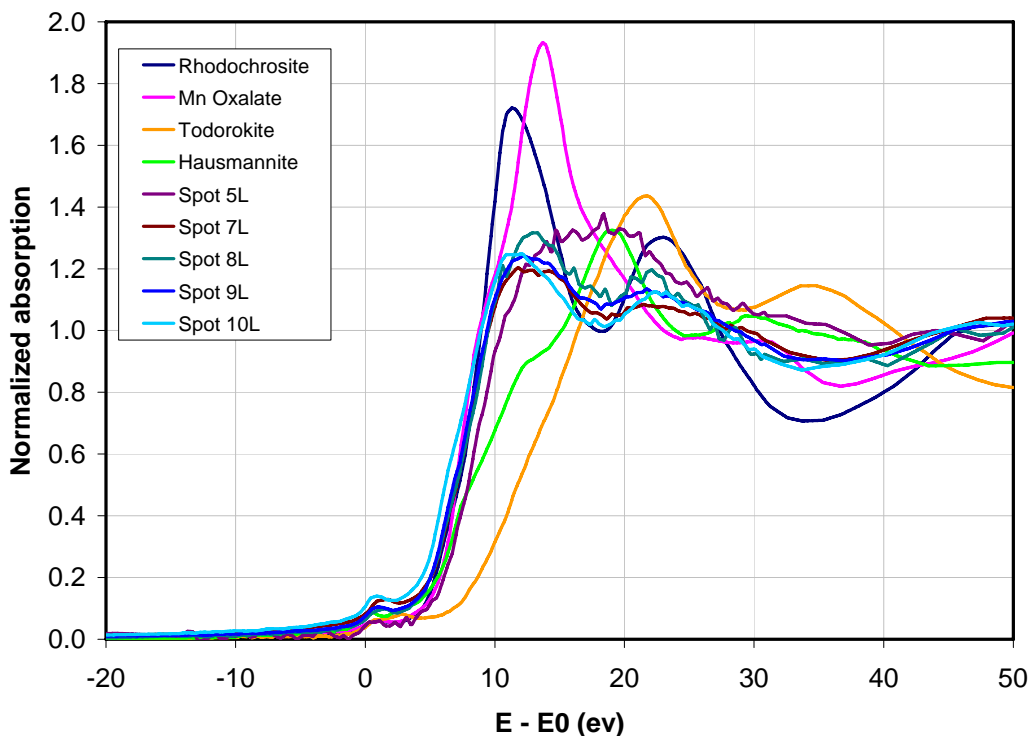**Figure 40**. XANES and EXAFS Spectra Collected from Four Locations Within the Water-Leached Tank C-106 Residual Waste Sample that Contained High Concentrations of Ag. (Standard results for Ag^0 and AgI are also included.)

XANES and EXAFS spectra collected from a number of high Mn locations within the unleached C-106 residual waste sample (Figure 41) and the water-leached C-106 residual waste sample (Figure 42) are shown below. Due to the relatively high concentration of Mn and the use of fluorescence detection, it is likely there is some self-absorption distortion in the spectra (Pfalzer et al. 1999). This suppresses the peaks above the edge, and enhances the pre-edge peak. Since only qualitative comparisons were used in the analysis, no attempt was made to apply a correction. Standard spectra for rhodochrosite, Mn oxalate, todorokite, and hausmannite are included in both figures. Analysis of XANES and EXAFS spectra indicate that the majority of Mn occurs as Mn^{+2} similar to rhodochrosite. In addition, the presence of a Mn(II)-oxalate, and a Mn^{+3} containing oxide or oxyhydroxide phase is also possible. These results are consistent with previous bulk XRD analysis of the samples.
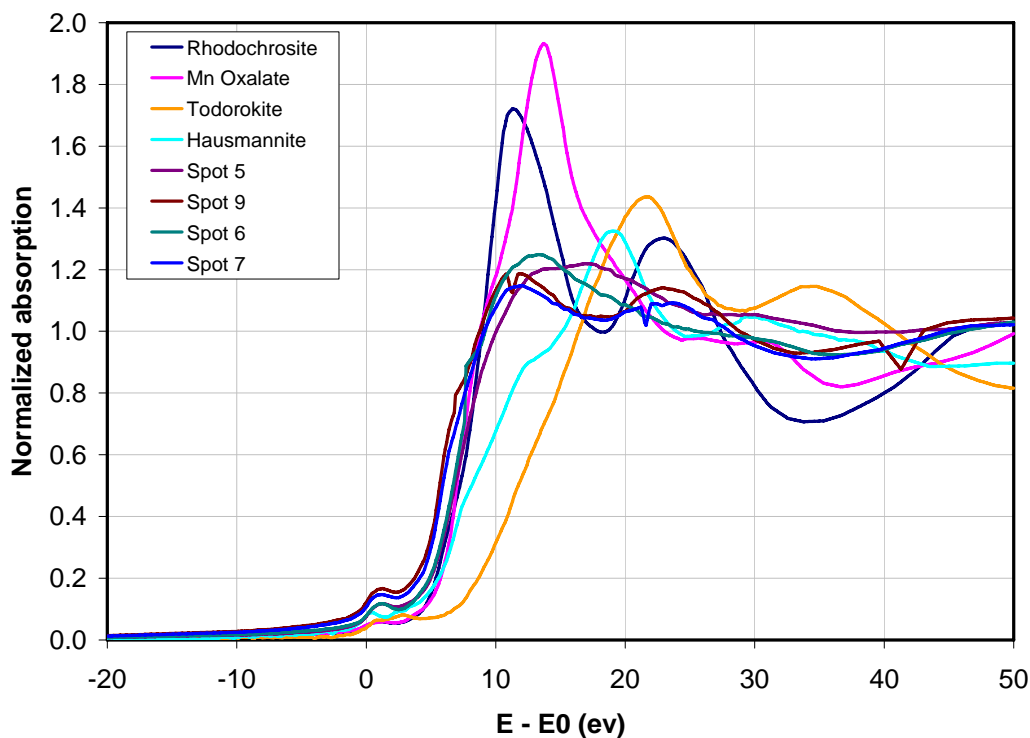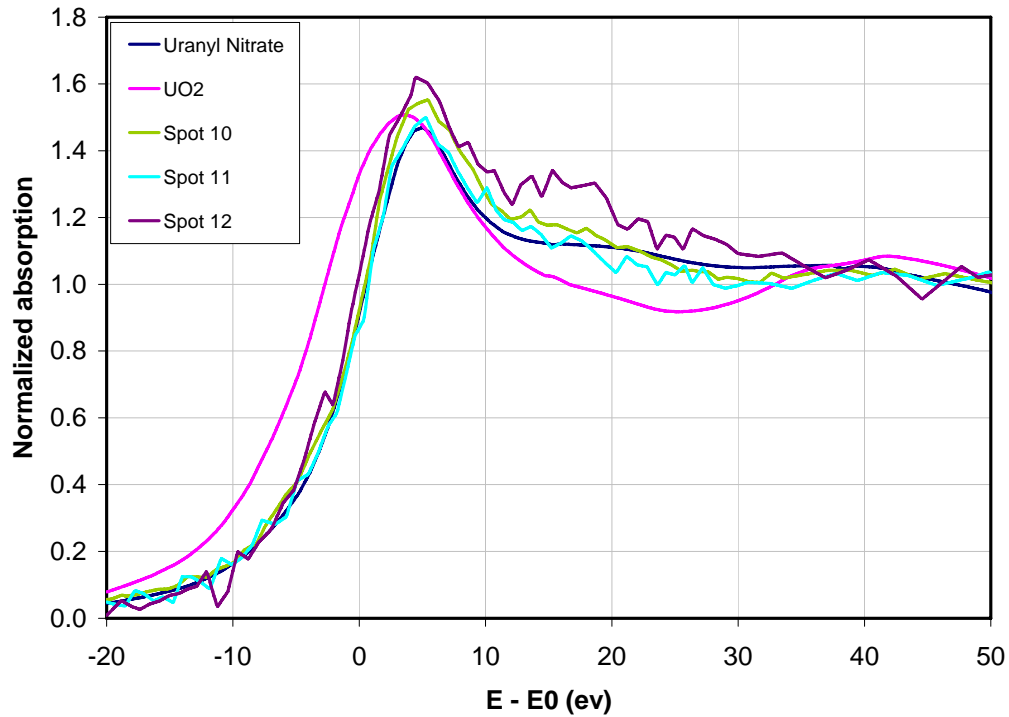

Figure 41.   XANES and EXAFS Spectra Mn Collected at Five Locations Within the Unleached Tank C-106 Residual Waste Sample, Along with Four Standard Phases
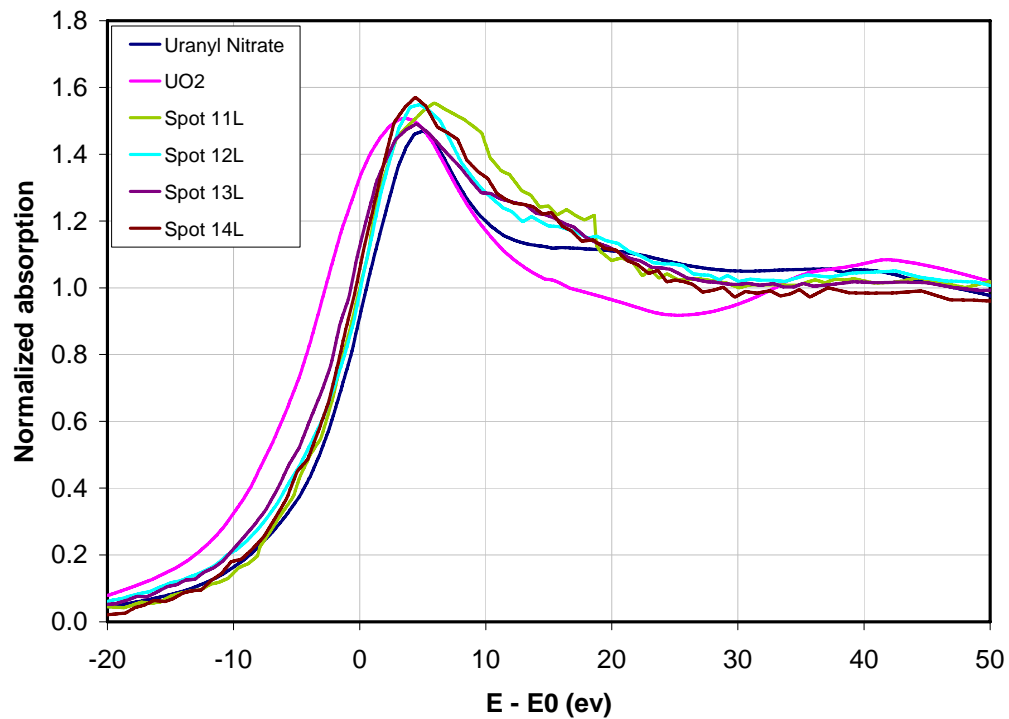
Figure 42. XANES and EXAFS Spectra Mn Collected at Five Locations Within the Water-Leached
Tank C-106 Residual Waste Sample, Along with Five Standard Phases

XANES and EXAFS spectra collected from a number of high U locations within the unleached C-106 residual waste sample (Figure 43) and the water-leached C-106 residual waste sample (Figure 44) are shown below. Standard spectra for uranyl nitrate and UO_2 are included in both figures. Analysis of these XANES and EXAFS spectra indicate that U occurs primarily in the form of UO_2^{2+} in both the unleached and water-leached C-106 samples. In the water-leached sample, the XANES spectra suggest that a small fraction of the U may be present as U^{+4}.

Figure 43. XANES and EXAFS Spectra U Collected at Three Locations Within the Unleached Tank C-106 Residual Waste Sample, Along with Two Standard Phases

Figure 44. XANES and EXAFS Spectra U Collected at Four Locations Within the Water-Leached Tank C-106 Residual Waste Sample, Along with Two Standard Phases

XANES and EXAFS spectra collected from a number of high Cr locations within the unleached C-106 residual waste sample are shown in Figure 45. The results indicate that the majority of the Cr in the unleached C-106 residual waste sample is in the tri-valent oxidation state. The exception to this was spot 8 in Figure 29. This location, which was enriched in Cr (see Figure 30), was also found to be enriched in nickel. Further analysis with XANES determined that the Fe, Cr, and Ni at this location were in the zero-valent oxidation state. This suggests that this particle is stainless steel. It is likely that this is contamination from the stainless steel sampling device used to collect the residual sludge sample after the sludge retrieval process was completed. Note that this material could not have come from the steel tank liners which are carbon steel, not stainless steel.

XANES analysis of Fe (spectra not shown) indicated that the majority of Fe present in both C-106 unleached and water-leached residual waste was in the tri-valent oxidation state.

A general conclusion from the analysis by µXRF, XANES, and EXAFS of the C-106 unleached and water-leached samples is that with a few minor exceptions, the two samples appear to be relatively similar in terms of the speciation of the major components and the contaminants of concern that could be examined with synchrotron x-ray techniques.
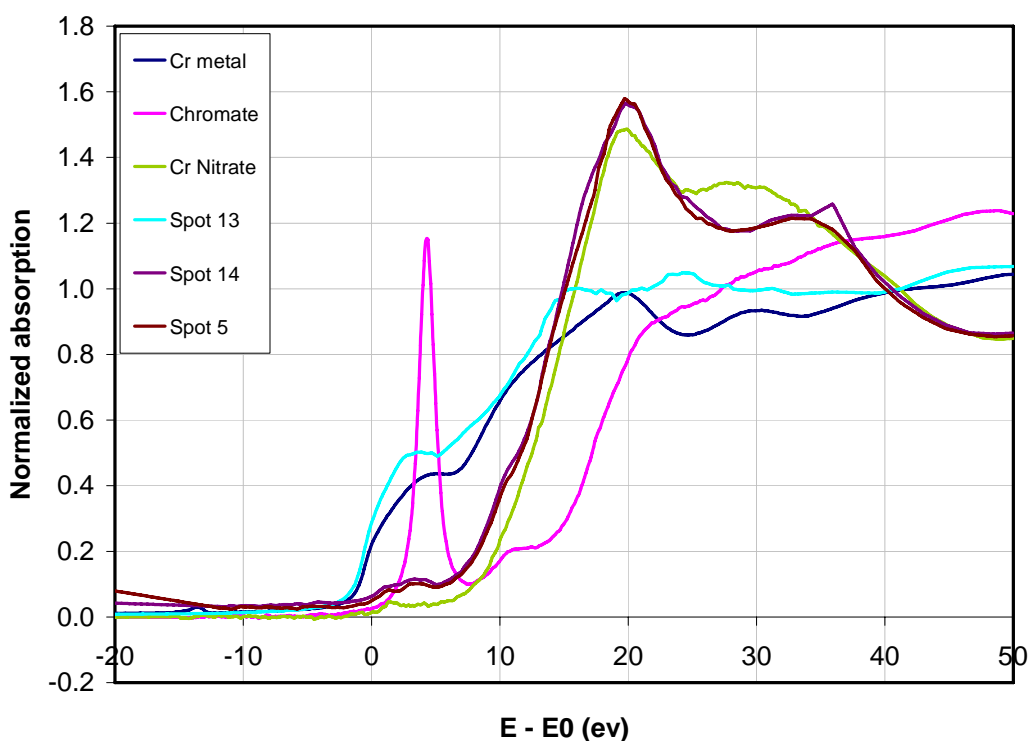

Figure 45.   XANES and EXAFS Spectra Cr Collected at Three Locations Within the Unleached Tank C-106 Residual Waste Sample, Along with Three Standard Phases

Tank C-106 Residual Waste Results: µXRD Analysis. µXRD patterns were collected on the unleached and leached residual waste from Hanford tank C-106. Each spot size measured approximately 5-µm diameter and covered areas of relatively large (approximately 20 to 100 µm) regions previously identified by µSXRF mapping as containing elements of interest (e.g., Ag, U, and I). Eight spot patterns (spot 1 to 8) were collected from the unleached residual waste sample and four spot patterns (spot 1L, 2L,

4L, and 5L) were collected from the leached residual waste sample. For convenience purposes, the crystalline phases previously identified in residual sludge from Hanford tank C-106 by bulk XRD (Deutsch et al. 2005) are provided in Table 9.

Table 9.   Crystalline Phases Identified by Bulk XRD in the Unleached and Leached Residual Waste from Hanford Tank C-106 (Deutsch et al. 2005)

Crystalline Phase	Formula	PDF
lindbergite	$MnC_2O_4 \cdot 2H_2O$	25-0544
gibbsite	$Al(OH)_3$	33-0018
dawsonite	$NaAlCO_3(OH)_2$	45-1359
hematite	Fe_2O_3	86-0550
böhmite	$AlO(OH)$	83-1505
rhodochrosite	$MnCO_3$	83-1763
whewellite	$CaC_2O_4 \cdot H_2O$	20-0231

As described in the methods section, 2D diffraction images for each spot were collected on image plates. Figure 46 is an example of the image collected from spot 4 of the unleached residual waste sample. These concentric rings correspond to diffraction from a polycrystalline material which consists of large numbers of discrete particles, each oriented slightly differently and each producing a distinct diffraction pattern. The different orientations allow for all possible diffraction patterns, resulting in concentric circles. The diffuse dark colored ring close to the center of the image is from the interaction of the sample holder material (Kapton) with the x-ray beam. Using software such as FIT2D or JADE, the image was converted into 1D scans of image intensity versus °2θ (Figure 47) thus allowing for conventional XRD pattern processing. Because all the µXRD data were similar, only one µXRD image and resulting 1D plot will be presented in this section with the remaining located in the appendix.

The µXRD patterns taken of the unleached residual waste (spot 1 to 8) have reflections matching the database patterns for minerals already identified in the residual waste by bulk XRD (Table 9). However, more importantly, several of the spot patterns (spot 1 to 4) have reflections consistent with silver metal, which was not identified in the "bulk" sample. For example, spot 4 (unleached) has reflections at 17.784, 20.563, 29.241, and 34.433 °2θ, which matched PDF #65-2871, silver metal (Figure 47). Identification of silver is consistent with the µSXRF map for Ag, which showed Ag-rich concentrations in the regions surrounding spots 1 to 4. This is also in agreement with the SEM/EDX data reported by Deutsch et al. (2005).
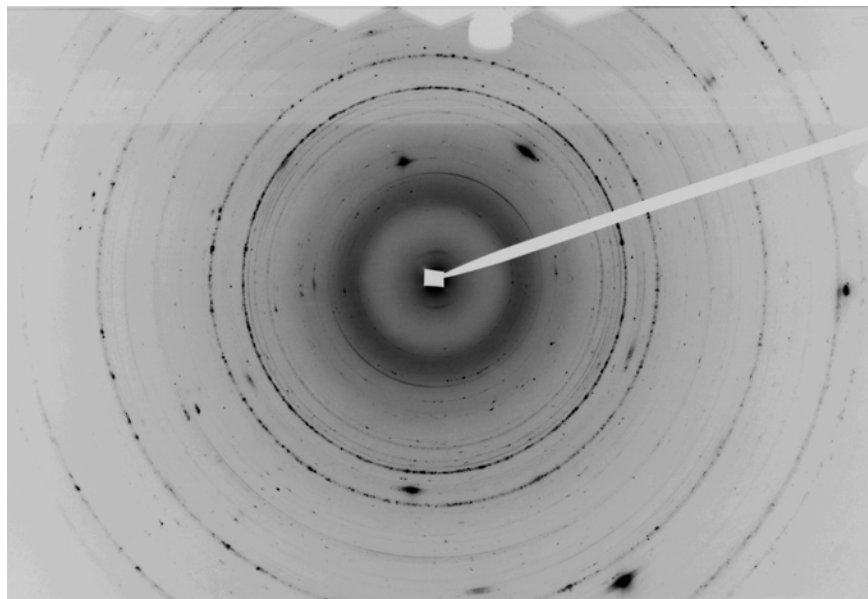
Figure 46. µXRD Pattern (incoming wavelength of 0.7293 Å) for Spot 4 (~5-µm diameter area), An Ag-Rich Region Identified from µSXRF Mapping
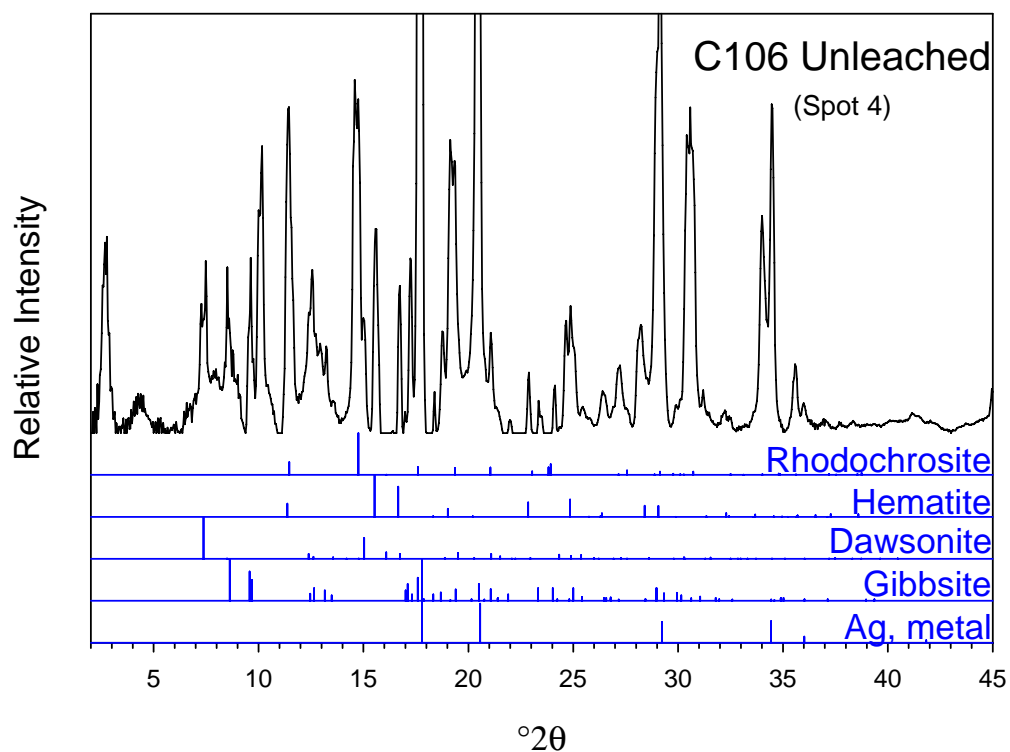

Figure 47. Background Subtracted µXRD Pattern for Unleached C-106 Residual Waste Shown with PDF Patterns for Gibbsite (PDF #33-0018), Hematite (PDF #86-0550), Rhodochrosite (PDF #83-1763), Dawsonite (PDF #45-1359), and Silver Metal (PDF #65-2871)

4.5   Mössbauer Spectroscopic Analysis of Tank C-204 Residual Waste

Previous selective extraction work conducted on tank sludge samples from several Hanford tanks indicated that significant fractions of several typically highly mobile contaminants of concern have been effectively immobilized in a number of samples. The selective extractions indicate that immobile fractions of ^{99}Tc and Cr are associated with Fe-containing phases. XRD has not been successful at identifying any crystalline Fe phase in sludge from tanks C-203 or C-204. As a result of these findings, Mössbauer spectroscopy was used to investigate the identity of the Fe-containing phase or phases responsible for sequestering ^{99}Tc and Cr in this tank sludge. Understanding the nature of these immobile forms of contaminants of concern is valuable for developing mechanistically based release models for risk assessments. In addition, fundamental knowledge of how these normally mobile contaminants have been so effectively sequestered could be applied in other applications for environmental benefit. Tank C-204 sludge has been selected for this investigation because of its relatively high Fe content (~13%) and low radioactivity.

Mössbauer spectra are used for identification and characterization of Fe oxides. This follows primarily from the fact that the different Fe oxides are ordered magnetically over a wide range of temperatures from 950 K down to below 78 K. The Mössbauer parameters of the various magnetically ordered Fe oxides differ considerably and thus allow unequivocal identification and often quantification in mixtures to be made. Mössbauer spectroscopy is insensitive to all isotopes except [57]Fe (and a few other rare elements) and this makes the technique particularly useful in systems where Fe oxides may be too low in concentration or in crystallinity to be detected by XRD.

Mössbauer spectroscopy is based on the magnetic behavior of Fe in a crystal structure, yielding information about charge and coordination. The Mössbauer effect involves resonant absorption of γ-radiation by [57]Fe nuclei in solid Fe oxides. Transitions between the I = 1/2 and the I = 3/2 nuclear energy levels induce resonant absorption. A Mössbauer spectrum is a plot of the transmission of the rays versus the velocity of their source. Movement of the source ([57]Co for Fe compounds) ensures that the nuclear environments of the absorber and the source will match at certain velocities (i.e., energies) and, hence, absorption takes place. In the absence of a magnetic field, the Mössbauer spectrum consists of one or two adsorption maxima. When a static magnetic field acts on the resonant nuclei, this splits the nuclear spin of the ground state into two and those of the excited state into four. The six allowed transitions then produce a 6-line spectrum. The positions and the numbers of the absorption maxima are determined by the hyperfine interactions between the resonant nuclei and the electrons surrounding them. There are three types of hyperfine interaction:

1. The *electric monopole interaction* is a function of the s electron densities at the nucleus. The resulting displacement of the spectrum provides information about the coordination number, the valency and spin state of the Fe in the compound.

2. The *electric quadrupole interaction* is generated when an electric field gradient acts on the nucleus. The quadrupole interaction or splitting provides information about site distortion, e.g., specifically bound ligands.

3. The *magnetic hyperfine field* provides information about the valence and magnetic properties of the compound. Because the latter depend on temperature, Mössbauer spectra are often recorded at different temperatures.

4.5.1   Methods

Because of the radioactive nature of these samples, they were encased in epoxy to eliminate the possibility of sample dispersion. The samples are prepared in a small copper ring with a volume of approximately 1.5 ml. Cellophane tape is applied to one end of the ring. A mixture of approximately 1 ml of epoxy resin, hardener, and approximately 200 mg of whole dry tank C-204 sludge was placed in the ring on the tape and allowed to harden.

Mössbauer spectra were collected using a 50 mCi (initial strength) ^{57}Co/Rh source. The velocity transducer MVT-1000 (WissEL) was operated in constant acceleration mode (23 Hz, ±10 mm/s or ±6 mm/s). An Ar-Kr proportional counter was used to detect the radiation transmitted through the holder, and the counts were stored in a multi-channel scalar (MCS) as a function of energy (transducer velocity) using a 1024 channel analyzer. Data were folded to 512 channels to give a flat background and a zero-velocity position corresponding to the center shift (CS or δ) of a metallic Fe foil at room temperature (RT). Calibration spectra were obtained with a 20 μm thick α-Fe(m) foil (Amersham, England) placed in exactly the same position as the sample to minimize any errors due to changes in geometry.

A closed-cycle cryostat (ARS, Allentown) was employed for low temperature measurements. For the low temperature measurements, both the source and drive assembly were held at RT.

The data were modeled with Recoil software (University of Ottawa, Canada) using a Voigt-based spectral fitting routine (Rancourt and Ping 1991). In this method, each distribution [quadrupole splitting distribution (QSD) and hyperfine field distribution (HFD)] is represented by a sum of Gaussian distributions having different positions, widths, and relative areas. The number of Gaussians used for a fit was the minimum required for good statistics. The coefficients of variation of the spectral areas of the individual sites generally ranged between 1 and 2% of the fitted value. The following guidelines were used in modeling the Mössbauer data: i) for sextets, the ratios of the spectral areas of peak 1 to peak 3, and peak 2 to peak 3 were fixed at 3 and 2, respectively; ii) coupling was not allowed between δ (isomer shift) or the CS (center shift) with the distributed hyperfine parameter [quadrupole splitting (Δ or QS)]; and iii) coupling was not allowed between the quadrupole shift parameter (ε) with the distributed hyperfine parameter (z).

4.5.2   Results

Mössbauer analysis of the tank C-204 sample was conducted at RT, 77 K and 12 K. The three spectra are shown below in Figure 48. The RT spectrum clearly indicates that almost all of the Fe is present as Fe(III), most probably in octahedral configuration (based on isomer shift and quadruple shift parameter values). Note that the doublet feature is due to paramagnetic Fe and sextet feature indicates magnetic character. The presence of multiple signals in the 12 K spectrum, at least two sextets and a doublet, indicates that the doublet at RT is a mix of Fe environments. The fit of the 12 K is good but is not unique. The 12 K spectrum suggests that the sample may have a couple percent Fe(II).

After examination of the 77 K spectrum (panel b of the figure displayed below) of the sample, it appears that the outer sextet evident in the 12 K spectrum (panel c) could be due to Fe(III)-oxide (possibly Al-goethite) of small particle size (~10 nm) and/or oxide with some diamagnetic metal substitution (e.g., Al). Note the spectral areas of the sextet in 77 K spectrum and the outer sextet in the 12 K spectrum are
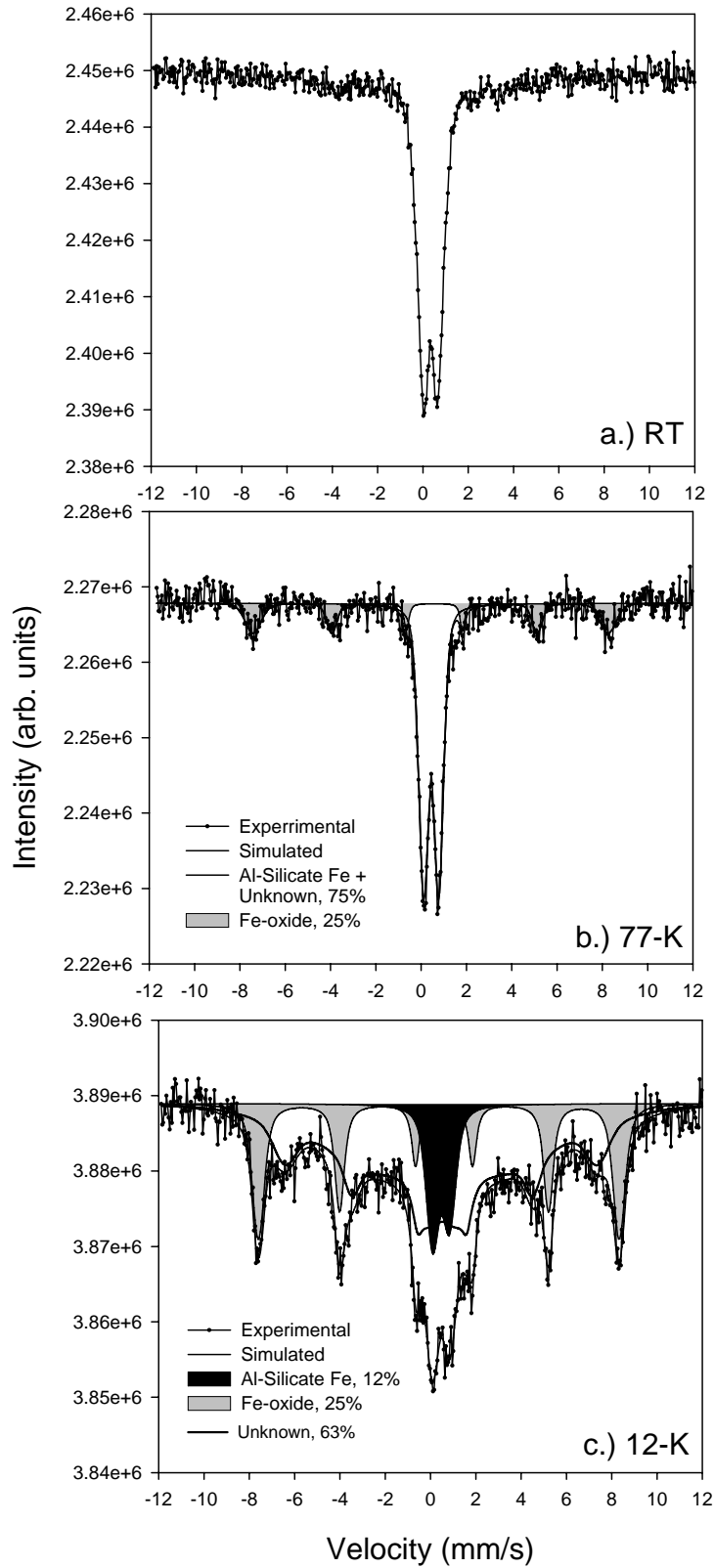
Figure 48. Mössbauer Spectra of Tank C-204 Residual Tank Waste Collected at Room Temperature, 77 K, and 12 K

identical, 25% – they differ from each other in the hyperfine field values (which is expected due to the temperature difference). This interpretation was based on: (a) evidence of Fe(III)-oxide presence in the sludge by SEM/EDS, (b) Al presence in the sludge, and (c) spectral features similar to that of a soil Al-goethite (Kukkadapu et al. 2005) (doublet at RT and sextet at 77 K and 12 K with similar features). The sextet feature is not likely to be due to hematite/maghemite, and definitely not due to lepidocrocite, based on derived Mössbauer parameters.

Mössbauer spectra obtained at various temperatures also indicated that the doublet at 77 K is mixture of at least two Fe-environments that were unresolved from each other at this temperature. The presence of "collapsed" sextet/inner sextet (63% area) feature in the 12 K spectrum was in agreement with such a hypothesis. The combined spectral area of the doublet and the "collapsed" sextet was similar to that of the 77 K doublet area. The nature of the "collapsed" sextet, however, is not apparent from Mössbauer data due to sludge heterogeneity. What is apparent from Mössbauer is: a) it is due to Fe(III) and b) the amount of Fe in this phase could be low [due to diamagnetic metal substitution (e.g., Al)].

5.0   Conclusions

Advancements in the testing of tank waste have led to a better understanding of the chemical composition and solid phases present in the material. The following is a summary of the contribution made by each technique discussed in this report.

A method has been developed to completely extract ^{129}I from tank sludge. The method consists of potassium nitrate/potassium hydroxide fusion of a sludge sample followed by dissolution of the solid in a mixture of sulfuric acid and sodium bisulfite. The sulfuric acid and sodium bisulfite enhance dissolution of the solid and prevent volatilization of iodine. This extraction method is an improvement over previous methods that did not completely dissolve the sludge and may have resulted in low recoveries. After extraction, the solution is directly analyzed on an ICP-MS using reaction cell technology. This analytical method significantly reduces sample preparation time/complexity compared to previous analytical methods (radio-counting by LEPS) and provides an estimated quantitation limit (EQL) on the order of 1 pCi/L.

The reaction cell technology of the ICP-MS system is also being evaluated for the measurement of the TRUs (^{237}Np, ^{239}Pu, and ^{241}Am) and ^{90}Sr. These important constituents of tank sludge are conventionally measured using a multi-step, wet chemical separation procedure followed by analysis using radio-counting. The ICP-MS method significantly reduces the complexity of this analysis. Testing of the method has shown promise of low quantitation limits, and the technique is being optimized to bring the limits into the range achievable by counting.

The mapping of elements in sludge using SEM/EDS has lead to a significant improvement in understanding the distribution of elements and their associations in the sludge solids. Previous methods provided spot measurements of elements in the solids, but the new procedure allows for an elemental map of a wide area of a sample. Work to date has shown the association of Ag and Hg with Fe solids in tank C-106 sludge and the apparent lack of these metal associations with Al solids.

Synchrotron-based x-ray techniques, including µXRD, µXRF, XANES, and EXAFS, have been shown to have significant potential for determining phase associations and speciation of major components and contaminants of concern in sludge. Goethite and maghemite were identified in tank C-203 sludge using µXRD. These minerals were not identified in this sample using standard XRD on the bulk sample of this sludge. XANES and EXAFS data collected from tank C-106 sludge suggest that Ag is present in the zero-valent (metallic) form and not, primarily, as an iodide. This does not discount the possibility that iodide is present as AgI, but it would be a small part of the total Ag present in the sludge. The XANES and EXAFS spectra for tank C-106 sludge also showed that the majority of the Mn is present as rhodochrosite, U occurs primarily as U(VI) [with a small fraction of U(IV)], the majority of Cr is Cr(III), and Fe is primarily Fe(III).

The initial attempt at the application of Mössbauer spectra for identification and characterization of Fe oxides in residual tank sludge was less definitive than the synchrotron-based x-ray techniques. Select use of this analytical technique for tank waste samples in combination with other analytical techniques may still prove to be useful but will require additional evaluation.

6.0   Path Forward

Although the analytical techniques described in this report have improved our knowledge of the tank waste, there are many aspects of this material that have not been suitably characterized. In particular, the solid phase sources of ^{99}Tc and ^{129}I have not been identified. Our working model is that ^{99}Tc is associated with Fe oxyhydroxides, and ^{129}I may be associated with silver in the sludge; however, it has not been possible to confirm those associations with the current testing methods. This section describes some of the improvements to sludge characterization and testing that are being considered.

6.1   Enhancement of JEOL JSM-840 SEM System

The JEOL JSM-840 SEM system used for the SEM analyses presented in this report is equipped with EDS. For the reasons discussed below, the chemical analyses of solids in residual tank waste could be further quantified by the addition of wavelength dispersive spectroscopy (WDS).

When an electron beam from the SEM electron gun collides with a specimen, generation of x-rays, in addition to BSE, secondary electrons, and photons (cathodoluminescence), are the most important kinds of emissions that take place. X-rays are emitted in the specimen from a volume of a few cubic micrometers, and can therefore be considered to originate from a point source. The x-rays are generated with energies and wavelengths that are characteristic of the chemical elements responsible for their emission. SEM instruments are capable of being fitted with energy dispersive (EDS or EDX) or wavelength dispersive (WDS) x-ray spectrometers that discriminate x-ray emissions via energy or wavelength, respectively. EDS is more commonly applied due to its simplicity and speed. On the other hand, WDS measurements are more quantitative, but more time consuming. Because the instrument must be tuned to the elements of interest, their presence in a sample must first be detected or anticipated. WDS is also the foundation for analysis of x-ray emissions in electron probe microanalysis (EPMA) (or electron microprobe), which is in the same general family of particle beam instruments that utilize high-energy electrons and the information gained from their interaction within a specimen. WDS offers important advantages over EDS by providing more accurate and quantitative analyses, analyses of light elements with at least an order of magnitude higher sensitivity than EDS instruments, resolution of overlapped spectrum peaks for improved element specificity, and lowered detection limits over the entire periodic table. With WDS, most elements are detected below 1,000 ppm and some as low as a few ppm. Combining EDS and WDS spectrometers on an SEM would allow the analyst to take advantage of the strengths of both techniques.

6.2   Inductively Coupled Plasma-Mass Spectrometry Method Development

The state-of-the-art Perkin Elmer Elan DRC II ICP-MS, with its dynamic reaction cell technology, is being tested for its potential to replace several radiochemical separations and counting procedures currently being used at PNNL. Preliminary testing of TRU elemental analysis in the presence of high concentrations of U as well as Sr analysis in the presence of Y and Zr has been successful. Although these analytical protocols have yet to be perfected, they both appear to be viable alternatives to conventional radiochemical counting techniques. Additional details regarding the path forward for the respective techniques are contained below.

6.2.1   Transuranic Analysis

Currently, PNNL has successfully analyzed "surrogate" solutions of tank C-203 acid extracts containing 10 mg/L U with 0.1 µg/L of [237]Np, [239]Pu, and [241]Am. We believe the Perkin Elmer Elan DRC II ICP-MS can be used to achieve seven orders of magnitude reduction in U signal via reaction of the element with O_2. Analytical method testing/development by adjusting reaction gas flows, nebulizer gas flows, and instrument power settings (RPq values) is continuing.

6.2.2   Strontium-90 Analysis

PNNL has documented the potential applicability of ICP-MS analysis of [90]Sr. We have yet to optimize this analytical protocol with respect to removal of Y prior to injection of the samples into the instrument's second (and primary) quadrapole. Although we have theoretically reduced the Y signal sufficiently enough to make quantitative analysis of ^{90}Sr possible, we have yet to test this analysis with ^{90}Sr/[90]Y. Additionally, we believe the protocol can be further optimized, by adjusting gas flows and power settings, to reduce the Y signal even further. Therefore, additional method development testing is currently underway. Once the analytical method has been optimized (reaction gas flows/instrument settings), we plan to use extracts from tank C-106 residual sludge samples (approximately 3,500 µCi/g ^{90}Sr) to verify this new analytical technique. We will compare the ICP-MS results from this effort with the "conventionally measured" values based on ^{90}Sr wet chemical separation and LSC as reported in Deutsch et al. (2005).

6.2.3   Analysis of Hanford In-Tank Sludge by Microwave Digestion

A critical part of testing for the Hanford in-tank sludge is the measurement of the total composition. The current test plan utilizes two basic preparation methods to accomplish this goal. The first method is an acid leaching procedure that is similar to EPA Method 3050B (EPA 2003) that involves heating the sample with nitric acid and hydrogen peroxide. The second method is a caustic fusion procedure that involves adding a potassium hydroxide and sodium nitrate solution to the sample and heating it to 550°C. The resulting fused solid is then dissolved in an aqueous acid solution. Both methods show the presence of filterable solids at the completion of the preparation. Though the percentage of the residual solid is low compared to the total solids treated, there remains an uncertainty on how to calculate total composition. To resolve these uncertainties, a new technique – total dissolution by microwave digestion – is being investigated.

Microwave digestion uses high temperatures and pressures to accelerate the digestion process and assist in the dissolution of difficult sample matrixes. There are several advantages to this type of sample preparation: 1) the ability to use hydrofluoric acid with nitric acid to achieve complete dissolution; 2) lower sample to solution ratios, which lead to improved detection limits; and 3) the use of high pressure to prevent volatilization of certain elements. EPA Method 3052, *Microwave Assisted Acid Digestion of Siliceous and Organically Based Matrices* (EPA 2003) is a promulgated procedure for the total digestion of solid and sludge. It is also approved for the analysis of mercury by ICP-MS.

Method 3052 has been evaluated at PNNL by performing digestions on three National Institute of Standards and Technology (NIST) Standard Reference Materials[6] (SRM):

- SRM 2709 San Joaquin Soil, Baseline Trace Element Concentrations.
- SRM 2710 Montana Soil, Highly Elevated Trace Element Concentrations.
- SRM 2711 Montana Soil, Moderately Elevated Trace Element Concentrations.

The standards were digested in 10 mL double deionized water, 5 mL nitric acid, 2 mL hydrochloric acid, and 1 mL HF acid with microwave setting in accordance to Method 3052. Boric acid was added at the completion of the digestion. The resulting digestates contained no visible solids. The measured concentrations by ICP-OES for the major elements were compared to the standard values with recoveries between 92% to 100% with the exceptions of silicon (80%) and sulfur (86%).

The next phase of testing will be to perform the same digestion method on Hanford tank sludge from tanks 241-C-203, 241-C-204 and 241-C-106. ICP and radiochemical analysis of the resulting digestates will be compared to existing analytical data. With acceptable comparison data and the lack of visible solids, the need to perform two separate preparations would be eliminated. This would lower the amount of waste generated and improve the quality of the data.

6.2.4 Coprecipitation of ^{99}Tc by Fe(III) and Al Hydroxide/Oxide Solids

PNNL's studies of residual waste from tanks AY-102, BX-101, C-203, C-204, and C-106 (Deutsch et al. 2004, 2005; Krupka et al. 2004) were not successful at identifying the solid phase(s) that are sequestering ^{99}Tc. This determination is difficult due to the multi-phase assemblage of crystalline and amorphous solids that make up the waste, the complexity of the structure of multi-phase aggregates and mineral coatings that exist in this waste, and the low concentrations of ^{99}Tc in the bulk solid waste relative to the concentrations of the other elements present. Selective extraction studies by Deutsch et al. (2005) and Krupka et al. (2004) suggest that ^{99}Tc is likely associated with Fe(III) and/or Al hydroxide/oxide solids present in the tank waste, but there is no direct evidence for this from the results of the solid-phase characterization studies completed to date.

Studies are therefore proposed to (1) determine if ^{99}Tc under oxidizing conditions coprecipitates in the crystalline structures of specific Fe(III) and Al hydroxide/oxide solid phase identified by PNNL in residual tank waste, and (2) measure the dissolution rates of such coprecipitated ^{99}Tc solids. The dissolution rates in turn can be used in source term models to predict the long-term release of ^{99}Tc from such residual tank waste with or without implementation of in situ sludge stabilization technologies. The proposed research will focus on the hypothesis that in some Hanford underground storage tanks, ^{99}Tc is present as coprecipitated (i.e., absorbed into the crystalline structure) ^{99}Tc in Fe(III) oxide solids (e.g., hematite ─ Fe_2O_3) and/or Al hydroxide/oxide solids (e.g., gibbsite ─ $Al(OH)_3$) in the residual waste. Hematite and gibbsite have been identified by PNNL in unleached solid residual waste from tanks AY-102 and C-106 (Deutsch et al. 2005, Krupka et al. 2004). By restricting these experiments to single-solid phase systems, there is greater likelihood of determining the role of Fe or Al oxides/hydroxides have in trapping ^{99}Tc, and using solid-phase characterization techniques (discussed in the following paragraphs) to determine the speciation and coordination of the trapped ^{99}Tc. If PNNL's hypothesis is correct, this

---

[6] Registered Trademark.

uptake process is, therefore, responsible for the recalcitrant nature measured by Krupka et al. (2004) and others for ^{99}Tc in AY-102 sludge leached by water, carbonate-rich, acid, and other leachates.

The geochemical interactions between ^{99}Tc(VII) and Fe(III) hydroxide/oxide solids will be investigated by first precipitating hematite following the procedures used by Duff et al. (2002) and Ford et al. (1999) at ambient and higher temperatures relevant for tank environments from a series of solutions containing a range of dissolved concentrations of ^{99}Tc in the pertechnetate oxidation state [^{99}Tc(VII)]. The speciation of ^{99}Tc in the coprecipitated hematite will be characterized by techniques, such as bulk XRD, SEM in conjunction with EDS, synchrotron-based methods (XANES, μXRD, μXRF), TEM, Mössbauer spectroscopy, and x-ray photoelectron spectroscopy (XPS).

If coprecipitation of ^{99}Tc(VII) is detected in hematite, dissolution experiments will be conducted at ambient temperature to measure the dissolution rate of the Tc(VII)-Fe(III) coprecipitated hematite. The experiments will consist of a series of batch and flow-through leach studies to estimate ^{99}Tc(VI) release from ^{99}Tc(VII)-Fe(III) coprecipitated hematite as a function of time and key geochemical parameters (e.g., pH and dissolved carbonate). The leachates will include deionized water, Hanford vadose pore water, and simulated cement pore fluid. These characterization results and measured dissolution rates will be used to develop a kinetic source-term model for the long-term release of ^{99}Tc from residual sludge materials in the absence of any situ sludge stabilization.

If the coprecipitation experiments with hematite fail to show any detectable substitution of ^{99}Tc(VII) for Fe(III) in the hematite structure, a second series of coprecipitation experiments will be proposed (and procedures identified and refined) to test the hypothesis that coprecipitation of ^{99}Tc(VII) for Al in gibbsite [$Al(OH)_3$] is the key process responsible for the recalcitrant nature measured by Krupka et al (2004) for ^{99}Tc in AY-102 sludge. As noted previously, gibbsite was also identified by XRD and SEM analyses as one of the dominant crystalline phases present in the samples of unleached and water-leached residual waste from tanks C-106 (Deutsch et al. 2005) and AY-102 (Krupka et al. 2004). The behavior (or lack) of stable ^{99}Tc(VII) in the coprecipitated gibbsite will be characterized by techniques, such as XRD, SEM, XPS, XANES, μXRD, and μXRF. If coprecipitation of ^{99}Tc(VII) is detected in gibbsite, dissolution experiments will also be completed at ambient temperature to measure the dissolution rate of the coprecipitated gibbsite. The leachates will include deionized water, Hanford vadose pore water, and simulated cement pore fluid.

7.0 References

Allison JD, DS Brown, and KJ Novo-Gradac. 1991. *MINTEQA2/PRODEFA2, A Geochemical Assessment Model for Environmental Systems: Version 3.0 User's Manual*. EPA/600/3-91/021, U.S. Environmental Protection Agency, Athens, Georgia.

Agnew SF, J Boyer, RA Crobin, TB Duran, JR FitzPatrick, KA Jurgensen, TP Ortiz, and BL Young. 1997. *Hanford Tank Chemical and Radionuclide Inventories: HDW Model Rev. 4*. LA-UR-96-3860, Los Alamos National Laboratory, Los Alamos, New Mexico.

Ames LL and D Rai. 1978. *Radionuclide Interactions with Soil and Rock Media. Volume 1: Processes Influencing Radionuclide Mobility and Retention, Element Chemistry and Geochemistry, and Conclusions and Evaluations*. EPA 520/6-78-007-a, U.S. Environmental Protection Agency, Las Vegas, Nevada.

Ames LL, JE McGarrah, BA Walker, and PF Salter. 1982. "Sorption of Uranium and Cesium by Hanford Basalts and Associated Secondary Smectite." *Chemical Geology* 35:205-225.

Anderson JD. 1990. *A History of the 200 Area Tank Farms*. WHC-MR-0132, Westinghouse Hanford Company, Richland, Washington.

Anderson KA and P Markowski. 2000. "Speciation of Iodide, Iodine, and Iodate in Environmental Matrixes by Inductively Coupled Plasma Atomic Emission Spectrometry Using in situ Chemical Manipulation." *Journal of AOAC International* 83:225-230.

Barnett MO, PM Jardine, and SC Brooks. 2002. "U(VI) Adsorption to Heterogeneous Subsurface Media: Application of a Surface Complexation Model." *Environmental Science and Technology* 36:937-942.

Barrow NJ and JW Bowden. 1987. "A Comparison of Models for Describing the Adsorption of Anions on a Variable Charge Mineral Surface." *Journal of Colloid and Interface Science* 119:236-250.

Bartlett RJ and JM Kimble. 1976a. "Behavior of Chromium in Soils: I. Trivalent Forms." *J. Environ. Qual*. 5(4):379-383.

Bartlett RJ and JM Kimble. 1976b. "Behavior of Chromium in Soils: II. Hexavalent Forms." *J. Environ. Qual*. 5(4):383-386.

Bartlett R and B James. 1979. "Behavior of Chromium in Soils: III. Oxidation." *J. Environ. Qual*. 8(1):31-35.

Barton GB and ED McClanahan. 1956. *Chemistry of the "Silver Reactor" Part A. Influence of NO$_2$ Concentration and Temperature during Slug Dissolving. Part B. Reactions with Ammonia Gas*. HW-42408, United States Atomic Energy Commission, Hanford Atomic Products Operation, Richland, Washington.

Beasley TM and HV Lorz. 1984. "A Review of the Biological and Geochemical Behavior of Technetium in the Marine Environment." In *Technetium in the Environment*, G Desment and C Myttenaere, pp. 197-2xx, Elsevier, New York, New York.

Bechtold DB, GA Cooke, DL Herting, JC Person, RS Viswanath, and RW Warant. 2003. *Laboratory Testing of Oxalic Acid Dissolution of Tank 241–C–106 Sludge*. RPP-17158, Rev. 0, Fluor Hanford, Inc., Richland, Washington.

Borovec Z, B Kribek, and V Tolar. 1979. "Sorption of Uranyl by Humic Acids." *Chemical Geology* 27:39-46.

Brown GE, Jr., and NC Sturchio. 2002. "An Overview of Synchrotron Radiation Applications to Low Temperature Geochemistry and Environmental Science." In *Reviews in Mineralogy and Geochemistry, Volume 4. Applications of Synchrotron Radiation in Low-Temperature Geochemistry and Environmental Sciences*. PA Fenter, ML Rivers, NC Sturchio, and SR Sutton (eds.), pp. 1-115, The Mineralogical Society of America, Washington, D.C.

Burns PC and R Finch (eds.). 1999. *Uranium: Mineralogy, Geochemistry and the Environment. Reviews in Mineralogy. Volume 38*. Mineralogical Society of America, Washington, D.C.

Cantrell KJ, RJ Serne, and GV Last. 2002. *Hanford Contaminant Distribution Coefficient Database and Users Guide*. PNNL-13895, Pacific Northwest National Laboratory, Richland, Washington.

Cantrell KJ, RJ Serne, and GV Last. 2003. *Hanford Contaminant Distribution Coefficient Database and Users Guide*. PNNL-13895 Rev. 1, Pacific Northwest National Laboratory, Richland, Washington.

Chisholm-Brause C, SD Conradson, CT Buscher, PG Eller, and DE Morris. 1994. "Speciation of Uranyl Sorbed at Multiple Binding Sites on Montmorillonite." *Geochimica et Cosmochimica Acta* 58(17):3625-3631.

Colton NG, GJ Lumetta, AR Felmy, and JA Franz. 1993. *ESPIP Alkaline Tank Sludge Treatment: Fiscal Year 1993 Annual Report*. Pacific Northwest National Laboratory, Richland, Washington.

Coughtrey PJ, D Jackson, and MC Thorne. 1983. *Radionuclide Distribution and Transport in Terrestrial and Aquatic Ecosystems. A Critical Review of Data*. AA Balkema, Rotterdam, Netherlands.

Davis A and RL Olsen. 1995. "The Geochemistry of Chromium Migration and Remediation in the Subsurface." *Ground Water* 33(5):759-768.

Davis JA and DB Kent. 1990. "Surface Complexation Modeling in Aqueous Geochemistry." In *Mineral-Water Interface Geochemistry*, MF Hochella, Jr. and AF White (eds.), pp. 177-260, Reviews in Mineralogy, Volume 23, Mineralogical Society of America, Washington, D.C.

Deutsch WJ, KM Krupka, MJ Lindberg, KJ Cantrell, CF Brown, and HT Schaef. 2004. *Hanford Tanks 241-C-203 and 241-C-204: Residual Waste Contaminant Release Model and Supporting Data*. PNNL-14903, Pacific Northwest National Laboratory, Richland, Washington

Deutsch WJ., KM. Krupka, MJ Lindberg, KJ Cantrell, CF Brown, and HT Schaef. 2005. *Hanford Tank 241-C-106: Residual Waste Contaminant Release Model and Supporting Data*. PNNL-15187, Pacific Northwest National Laboratory, Richland, Washington.

DOE. 2002. *Performance Management Plan for the Accelerated Cleanup of the Hanford Site*. DOE/RL-2002-47, U.S. Department of Energy, Richland, Washington.

DOE. 2003. *Environmental Impact Statement for the Retrieval, Treatment, and Disposal of Tank Waste and Closure of Single-Shell Tanks at the Hanford Site, Richland, WA, Inventory, and Source Term Data Package*. DOE/ORP-2003-02, Rev. 0, U. S. Department of Energy, Richland, Washington.

Duff MC, J Urbanik Coughlin, and DB Hunter. 2002. "Uranium Co-precipitation with iron Minerals." *Geochimica et Cosmochimica Acta*, Vol. 66(20):3533-3547.

Duff MC and C Amrhein. 1996. "Uranium(VI) Adsorption on Goethite and Soil in Carbonate Solutions." *Soil Science Society of America Journal* 60(5):1393-1400.

EPA. 2003. "Microwave Assisted Acid Digestion of Siliceous and Organically Based Matrice." Method 3052 in *Test Methods for Evaluating Solid Waste, Physical/Chemical Methods*. EPA Publication SW-846, U.S. Environmental Protection Agency, Washington, D.C. Available online at http://www.epa.gov/epaoswer/hazwaste/test/pdfs/3052.pdf

EPA. 1999a. *Understanding Variation in Partition Coefficient, K_d, Values: Volume I. The K_d Model, Methods of Measurement, and Application of Chemical Reaction Codes*. EPA 402-R-99-04A, prepared by Pacific Northwest National Laboratory for the U.S. Environmental Protection Agency, Washington, D.C.

EPA. 1999b. *Understanding Variation in Partition Coefficient, K_d, Values: Volume II. Review of Geochemistry and Available K_d Values for Cadmium, Cesium, Chromium, Lead, Plutonium, Radon, Strontium, Thorium, Tritium (^3H), and Uranium*. EPA 402-R-99-004B, prepared by Pacific Northwest National Laboratory for the U.S. Environmental Protection Agency, Washington, D.C.

EPA. 2003 (in press). *Understanding Variation in Partition Coefficient, Kd, Values: Volume III. Review of Geochemistry and Available K_d Values for Americium, Arsenic, Curium, Iodine, Neptunium, Radium, and Technetium*. EPA 402-R-99-004C, prepared by KM Krupka and RJ Serne for the U.S. Environmental Protection Agency, Washington, D.C.

EPA. 2003. "Acid Digestion of Sediments, Sludges, and Soils." Method 3050B in *Test Methods for Evaluating Solid Waste, Physical/Chemical Methods*. EPA Publication SW-846, U.S. Environmental Protection Agency, Washington, D.C. Available online at http://www.epa.gov/epaoswer/hazwaste/test/pdfs/3050b.pdf

EPA. 2004. *Understanding Variation in Partition Coefficient, Kd, Values*. EPA 402-R 04-002C, prepared by KM Krupka and RJ Serne for the U.S. Environmental Protection Agency, Washington, D.C.

Eriksen TE, P Ndalamba, J Bruno, and M Caceci. 1992. "The Solubility of $TcO_2 \cdot nH_2O$ in Neutral to Alkaline Solutions under Constant p_{CO2}." *Radiochimica Acta* 58/59:67-70.

Falck WE. 1991. *CHEMVAL Project. Critical Evaluation of the CHEMVAL Thermodynamic Database with Respect to its Contents and Relevance to Radioactive Waste Disposal at Sellafield and Dounreay*. DoE/HMIP/RR/92.064, Department of Environment, Her Majesty's Stationary Office, London, England.

Fenter PA, ML Rivers, NC Sturchio, and SR Sutton (eds.). 2002. *Reviews in Mineralogy and Geochemistry, Volume 4. Applications of Synchrotron Radiation in Low-Temperature Geochemistry and Environmental Sciences*. The Mineralogical Society of America, Washington, D.C.

Finch R and T Murakami. 1999. "Systematics and Paragenesis of Uranium Minerals." In *Uranium: Mineralogy, Geochemistry and the Environment. Reviews in Mineralogy. Volume 38*, PC Burns and R Finch (eds.), pp. 91-179, Mineralogical Society of America, Washington, D.C.

Ford RG, KM Kemner, and PM Bertsch. 1999. "Influence of Sorbate-Sorbent Interactions on the Crystallization Kinetics of Nickel- and Lead-Ferrihydrite Coprecipitates." *Geochimica et Cosmochimica Acta*, Vol. 63(1):39-48.

Fredrickson JK, HM Kostandarithes, SW Li, AE Plymale, and MJ Daly. 2000. "Reduction of Fe(III), Cr(VI), U(VI), and Tc(VII) by Deinococcus radiodurans R1." *Applied and Environmental Microbiology* 66:2006-2011.

Frondel C. 1958. *Systematic Mineralogy of Uranium and Thorium*. Geological Survey Bulletin 1064, U.S. Geological Survey, Washington, D.C.

Gorski B and H Koch. 1970. "Uber die Komplexbideling von Technetium mit Chelatbildenden Ligande - II." *Journal of Inorganic and Nuclear Chemistry* 32:3831-3836.

Grenthe I, J Fuger, RJM Konings, RJ Lemire, AB Muller, C Nguyen-Trung, and H Wanner. 1992. *Chemical Thermodynamics 1: Chemical Thermodynamics of Uranium*. North-Holland, Elsevier Science Publishing Company, Inc., New York, New York.

Grenthe I, I Puigdomenech, MCA Sandino, and MH Rand. 1995. "Appendix D - Chemical Thermodynamics of Uranium." In *Chemical Thermodynamics 2: Chemical Thermodynamics of Americium*, pp. 347-374. North-Holland, Elsevier Science Publishing Company, Inc., New York, New York.

Gu B and RK Schulz. 1991. *Anion Retention in Soil: Possible Application to Reduce Migration of Buried Technetium and Iodine*. NUREG/CR-5464, prepared by the University of California at Berkeley, California, for the U.S. Nuclear Regulatory Commission, Washington, D.C.

Hammersley AP. 1997. FIT2D: An Introduction and Overview. Internal Report ESRF97HA02T, European Synchrotron Radiation Facility, Grenoble, France.

Hanlon, BM. 2000. Waste Tank Summary Report for Month Ending June 30, 2000. HNF-EP-0182-147. CH2M HILL Hanford Group, Inc., Richland, Washington.

Heald SM, EA Stern, D Brewe, RA Gordon, ED Crozier, D Jiang, and JO Cross. 2001. "XAFS at the Pacific Northwest Consortium - Collaborative Access Team Undulator Beamline." *J. Synchrotron Rad*. 8:42-344.

Hill JF, GS Anderson, and BC Simpson. 1995. *The Sort on Radioactive Waste Type Model: A Method to Sort Single-Shell Tanks in Characteristic Groups*. PNL-9814, Rev. 2, Pacific Northwest Laboratory, Richland, Washington.

Higley BA and DE Place. 2004. *Hanford Defined Waste Model – Revision 5*. RPP-19822, CH2M HILL Hanford Group, Inc. Richland, Washington.

Hsi C-KD and D Langmuir. 1985. "Adsorption of Uranyl Onto Ferric Oxyhydroxides: Application of the Surface Complexation Site-Binding Model." *Geochimica et Cosmochimica Acta* 49:1931-1941.

Hughes MA and FJC Rossotti. 1987. *A Review of Some Aspects of the Solution Chemistry of Technetium*. AERE-R 12820, University of Oxford, Oxford, England.

James BR and RJ Bartlett. 1983a. "Behavior of Chromium in Soils: V. Fate of Organically Complexed Cr(III) Added to Soil." *J. Environ. Qual*. 12(2):169-172.

James BR and RJ Bartlett. 1983b. "Behavior of Chromium in Soils. VI. Interactions Between Oxidation-Reduction and Organic Complexation." *J. Environ. Qual*. 12(2):173-176.

James BR and RJ Bartlett. 1983c. "Behavior of Chromium in Soils: VII. Adsorption and Reduction of Hexavalent Forms." *J. Environ. Qual*. 12(2):177-181.

Johnson KS. 1994. "Iodine." In *Industrial Minerals and Rocks*, D. C. Carr (ed.), pp. 583-588, Society for Mining, Metallurgy, and Exploration, Inc., Littleton, Colorado.

Jones EO, NG Colton, GR Bloom, GS Barney, SA Colby, and RG Cowan. 1992. "Pretreatment Process Testing of Hanford Tank Waste for the U.S. Department of Energy's Underground Storage Tank Integrated Demonstration." Proceedings of the International Topical Meeting on Nuclear and Hazardous Waste Management Spectrum '92, American Nuclear Society, Inc., La Grange Park, Illinois.

Kaplan DI, RJ Serne, and MG Piepho. 1995. *Geochemical Factors Affecting Radionuclide Transport Through Near and Far Fields at a Low-Level Waste Disposal Site*. PNNL-10379, Pacific Northwest National Laboratory, Richland, Washington.

Kaplan DI, RJ Serne, AT Owen, J Conca, TW Wietsma, and TL Gervais. 1996. *Radionuclide Adsorption Distribution Coefficient Measured in Hanford Sediments for the Low Level Waste Performance Assessment Project*. PNNL-11385, Pacific Northwest National Laboratory, Richland, Washington.

Krupka KM and RJ Serne. 2002. *Geochemical Factors Affecting the Behavior of Antimony, Cobalt, Europium, Technetium, and Uranium in Vadose Zone Sediments*. PNNL-14126, Pacific Northwest National Laboratory, Richland, Washington.

Krupka KM, WJ Deutsch, MJ Lindberg, KJ Cantrell, NJ Hess, HT Schaef, and BW Arey. 2004. *Hanford Tanks 241-AY-102 and 241-BX-101: Sludge Composition and Contaminant Release Data*. PNNL-14614, Pacific Northwest National Laboratory, Richland, Washington.

Kukkadapu RK, JM Zachara, J Fredrickson, J McKinley, S Smith, D Kennedy, and H Dong. 2005. "Reductive Biotransformation of Fe in Shale-Limestone Saprolite Containing Fe(III) Oxides and Fe(II)/Fe(III) Phyllosilicates." (Submitted to *Geochimica Cosmochimica Acta*.)

Lafemina JP. 1995. T*ank Waste Treatment Science Task Quarterly Report for April-June 1995*. PNL-10764, Pacific Northwest National Laboratory, Richland, Washington.

Langmuir D. 1997. *Aqueous Environmental Geochemistry*. Prentice Hall, Upper Saddle River, New Jersey.

Lieser KH. 1993. "Technetium in the Nuclear Fuel Cycle, in Medicine and in the Environment." *Radiochimica Acta* 63:5-8.

Lindberg MJ. 2004a. *Liquid Scintillation Counting and Instrument Verification Using the 1400 DSA™ Support Software*. AGG-ESL-002 Rev. 0, unpublished PNNL Technical Procedure, Pacific Northwest National Laboratory, Richland, Washington.

Lindberg MJ. 2004b. ^{99}Tc and ^{90}Sr Analysis Using Eichrom TEVAspec and SrSpec Resin. AGG-ESL-003 Rev. 0, unpublished PNNL Technical Procedure, Pacific Northwest National Laboratory, Richland, Washington.

Lindberg MJ. 2004c. *Precipitation Plating of Actinides for High-Resolution Alpha Spectrometry*. AGG-ESL-004 Rev. 0, unpublished PNNL Technical Procedure, Pacific Northwest National Laboratory, Richland, Washington.

Lindberg MJ. 2004d. *Counting Procedure for Alpha Spectrometry*. AGG-ESL-005 Rev. 0, unpublished PNNL Technical Procedure, Pacific Northwest National Laboratory, Richland, Washington.

Lindberg MJ. 2004e. *Separation of Am and Pu and Actinide Screen by Extraction Chromatography*. AGG-ESL-006 Rev. 0, unpublished PNNL Technical Procedure, Pacific Northwest National Laboratory, Richland, Washington.

Lindberg MJ and WJ Deutsch. 2003. *Tank 241-AY-102 Data Repor*t. PNNL-14344, Pacific Northwest National Laboratory, Richland, Washington.

Lloyd JR and LE Macaskie. 1996. "A Novel PhoshorImager-Based Technique for Monitoring the Microbial Reduction of Technetium." *Applied and Environmental Microbiology* 62(2):578-582.

Lloyd JR, JA Cole, and LE Macaskie. 1997. "Reduction and Removal of Heptavalent Technetium from Solution by Escherichia coli." *Journal of Bacteriology* 179(6):2014-2021.

Lloyd JR, HF Nolting, VA Solé, K Bosecker, and LE Macaskie. 1998. "Technetium Reduction and Precipitation by Sulfate-Reducing Bacteria." *Geomicrobiology Journal* 15:45-58.

Lloyd JR, J Ridley, T Khizniak, NN Lyalikova, and LE Macaskie. 1999. "Reduction of Technetium by *Desulfovibrio desulfuricans*: Biocatalyst Characterization and Use in a Flowthrough Bioreactor." *Applied and Environmental Microbiology* 65:2691-2696.

Lloyd JR, VA Sole, CVG Van Praagh, and DR Lovley. 2000. "Direct and Fe(II)-Mediated Reduction of Technetium by Fe(III)-Reducing Bacteria." *Applied and Environmental Microbiology* 66:3743-3749.

Lumetta GJ, BM Rapko, MJ Wagner, J Liu, and YL Chen. 1996a. *Washing and Caustic Leaching of Hanford Tank Sludges: Results of FY 1996 Studies*. PNNL-11278, Rev. 1, Pacific Northwest National Laboratory, Richland, Washington.

Lumetta GJ, MJ Wagner, FV Hoopes, and RT Steele. 1996b. *Washing and Caustic Leaching of Hanford Tank C-106 Sludge*. PNNL-11381, Pacific Northwest National Laboratory, Richland, Washington.

Lumetta GJ, IE Burgeson, MJ Wagner, J Liu, and YL Chen. 1997. *Washing and Caustic Leaching of Hanford Tank Sludges: Results of FY 1997 Studies*. PNNL-11636, Pacific Northwest National Laboratory, Richland, Washington.

Marchetti AA, L Rose, and T Straume. 1994. "A Simple and Reliable Method to Extract and Measure Iodine in Soils." *Analytica Chimica Acta* 296:243-247.

Mazzi U. 1989. "The Coordination Chemistry of Technetium in its Intermediate Oxidation States." *Polyhedron*, 8:1683-1688.

McKinley JP, JM Zachara, SC Smith, and GD Turner. 1995. "The Influence of Uranyl Hydrolysis and Multiple Site-Binding Reactions on Adsorption of U(VI) to Montmorillonite." *Clays and Clay Minerals* 43(5):586-598.

Meyer RE, WD Arnold, and FI Case. 1985. *Valence Effects on the Adsorption of Nuclides on Rocks and Minerals II*. NUREG/CR-4114, prepared for the U.S. Nuclear Regulatory Commission by Oak Ridge National Laboratory, Oak Ridge, Tennessee.

Meyer RE, WD Arnold, FI Case, and GD O'Kelley. 1991. "Solubilities of Tc(IV) Oxides." *Radiochimica Acta* 55:11-18.

Moran JE, U Fehn, and RTD Teng. 1998. "Variations in ^{129}I/^{127}I Ratios in Recent Marine Sediments: Evidence for a Fossil Organic Component." *Chemical Geology* 152:193-203.

Morel FMM, JG Yeasted, and JC Westall. 1981. "Adsorption Models: A Mathematical Analysis in the Framework of General Equilibrium Calculations." In *Adsorption of Inorganics at Solid-Liquid Interfaces*, MA Anderson and AJ Rubin (eds.), pp. 263-294, Ann Arbor Science Publishers, Inc., Ann Arbor, Michigan.

Muramatsu Y and KH Wedepohl. 1998. "The Distribution of Iodine in the Earth's Crust." *Chemical Geology* 147:201-216.

Nishiizumi K, D Elmore, M Honda, JR Arnold, and HE Gove. 1983. "Measurement of ^{129}I in Meteorites and Lunar Rock by Tandem Accelerator Mass Spectrometry." *Nature* 305:611-612.

Noll B, S Seifert, and R Münze. 1980. "New Tc(IV) Compounds with Nitriloacetic Acid." *Radiochemical and Radioanalytical Letters* 43:215-218.

Onishi Y, RJ Serne, EM Arnold, CE Cowan, and FL Thompson. 1981. *Critical Review: Radionuclide Transport, Sediment Transport, and Water Quality Mathematical Modeling; and Radionuclide Adsorption/Desorption Mechanisms*. NUREG/CR-1322 (PNL-2901), prepared for the U.S. Nuclear Regulatory Commission, Washington, D.C. by Pacific Northwest Laboratory, Richland, Washington.

Paquette J and WE Lawrence. 1985. "A Spectroelectrochemical Study of the Technetium(IV)/ Technetium(III) Couple in Bicarbonate Solutions." *Canadian Journal of Chemistry* 63:2369-2373.

Pfalzer P, JP Urbach, M Klemm, S Horn, ML denBoer, AI Prenkel, and JP Kirkland. 1999. "Elimination of Self-Absorption in Fluorescence Hard X-Ray Absorption Spectra." *Phys. Rev. B* 60:9335-9339.

Place, DE, BA Higley, and CW Burrup. 2004. *Best-Basis Inventory Template Compositions of Common Tank Waste Layers*. RPP-8847-Rev 1, CH2M HILL Hanford Group, Richland, Washington.

Rai D, JM Zachara, LE Eary, CC Ainsworth, FE Amonette, CE Cowin, RW Szelmeczka, CT Resch, RL Schmidt, SC Smith, and DC Girvin. 1988. *Chromium Reactions in Geologic Material*. EA-5741, Electric Power Research Institute, Palo Alto, California.

Rancourt DG and JY Ping. 1991. "Voigt-Based Methods for Arbitrary-Shape Static Hyperfine Parameter Distributions in Mossbauer Spectroscopy." In *Nuclear Instrumentation Methods Physical Reviews B58*, pp. 85-87.

Rapko BM and GJ Lumetta. 2000. *Status Report on Phase Identification in Hanford Tank Sludges*. PNNL-13394, Pacific Northwest National Laboratory, Richland, Washington.

Rapko BM, DL Blanchard, NG Colton, AR Felmy, J Liu, and GJ Lumetta. 1996. *The Chemistry of Sludge Washing and Caustic Leaching Processes for Selected Hanford Tank Wastes*. PNNL-11089, Pacific Northwest National Laboratory, Richland, Washington.

Rard JA, MH Rand, G Anderegg, and H Wanner (MCA Sandino and E Östhols, eds.). 1999. *Chemical Thermodynamics 3: Chemical Thermodynamics of Technetium*. North-Holland, Elsevier Science Publishing Company, Inc., New York, New York.

Read D, TA Lawless, RJ Sims, and KR Butter. 1993. "Uranium Migration Through Intact Sandstone Cores." *Journal of Contaminant Hydrology* 13:277-289.

Resano M, E Garcia-Ruiz, L Moens, and F Vanhaecke. 2005. "Solid Sampling-Electrothermal Vaporization-Inductively Coupled Plasma Mass Spectrometry for the Direct Determination of Traces of Iodine." *Journal of Analytical Atomic Spectrometry* 20:81-87.

Richard FC and ACM Bourg. 1991. "Aqueous Geochemistry of Chromium: A Review." *Wat. Res*. 25(7):807-816.

Russell CD, RC Crittenden, and AG Cash. 1980. "Determination of Net Ionic Charge on Tc-99m DTPA and Tc-99m EDTA by a Column Ion-Exchange Method." *Journal of Nuclear Medicine* 21:354-360.

Serkiz SM and WH Johnson. 1994. *Uranium Geochemistry in Soil and Groundwater at the F and H Seepage Basins (U)*. EPD-SGS-94-307, Westinghouse Savannah River Company, Savannah River Site, Aiken, South Carolina.

Shanbhag PM and GR Choppin. 1981. "Binding of Uranyl by Humic Acid." *Journal of Inorganic Nuclear Chemistry* 43:3369-3372.

Sheppard MI and DH Thibault. 1988. "Migration of Technetium, Iodine, Neptunium, and Uranium in the Peat of Two Minerotrophic Mires." *Journal of Environmental Quality* 17:644-653.

Smith DK. 1984. "Uranium Mineralogy." In *Uranium Geochemistry, Mineralogy, Geology, Exploration and Resources*, B DeVero, F Ippolito, G Capaldi, and PR Simpson (eds.) pp. 43-88. Institution of Mining and Metallurgy, London, England.

Smith RM and AE Martell. 1976. *Critical Stability Constants. Volume 4: Inorganic Complexes*. Plenum Press, New York, New York.

Smith RM, AE Martell, and RJ Motekaitis. 1997. *NIST Critically Selected Stability Constants of Metal Complexes Database. Version 4.0. User's Guide*. NIST Standard Reference Database 46, National Institute of Standards and Technology, Gaithersburg, Maryland. (Includes software and database files for use on personal computers using DOS and Windows operating systems.)

Sparks ST and SE Long. 1987. *The Chemical Speciation of Technetium in the Environment: A Literature Study*. DOE/RW 88.098 (UKAEA/DOE Radiological Protection Research Programme Letter AERE-R 12743), Harwell Laboratory, Oxfordshire, England.

Stanford Linear Accelerator Center. 2004. *Molecular Environmental Science: An Assessment of Research Accomplishments, Available Synchrotron Radiation Facilities, and Needs*. SLAC-R-704, Stanford Linear Accelerator Center, Stanford Synchrotron Radiation Laboratory, Stanford University, Stanford, California. Available URL: http://www.slac.stanford.edu/pubs/slacreports/slac-r-704.html

Strickert R, AM Friedman, and S Fried. 1980. "The Sorption of Technetium and Iodine Radioisotopes by Various Minerals." *Nuclear Technology* 49:253.

Temer DJ and R Villarreal. 1995. *Sludge Washing and Alkaline Leaching Tests on Actual Hanford Tank Sludge: A Status Report*. LAUR-95-2070, Los Alamos National Laboratory, Los Alamos, New Mexico.

Temer DJ and R Villarreal. 1996. *Sludge Washing and Alkaline Leaching Tests on Actual Hanford Tank Sludge: FY1996 Results*. LAUR-96-2839, Los Alamos National Laboratory, Los Alamos, New Mexico.

Temer DJ and R Villarreal. 1997. *Sludge Washing and Alkaline Leaching Tests on Actual Hanford Tank Sludge: FY1997 Results*. LAUR-97-2889, Los Alamos National Laboratory, Los Alamos, New Mexico.

Tripathi VS. 1984. *Uranium(VI) Transport Modeling: Geochemical Data and Submodels*. Ph.D. Dissertation, Stanford University, Stanford, California.

Turner GD, JM Zachara, JP McKinley, and SC Smith. 1996. "Surface-Charge Properties and UO_2^{2+} Adsorption of a Subsurface Smectite." *Geochimica et Cosmochimica Acta* 60(18):3399-3414.

Um W, RJ Serne, and KM Krupka. 2004. "Linearity and Reversibility of Iodide Adsorption on Sediments from Hanford, Washington, Under Water-Saturated Conditions." *Water Research* 38:2009-2016.

Uziemblo NH, B Mastel, and RR Adee. 1987. Unpublished results.

Waite TD, TE Payne, JA Davis, and K Sekine. 1992. *Alligators Rivers Analogue Project. Final Report Volume 13. Uranium Sorption*. ISBN 0-642-599394 (DOE/HMIP/RR/92/0823, SKI TR 92:20-13).

Waite TD, JA Davis, TE Payne, GA Waychunas, and N Xu. 1994. "Uranium(VI) Adsorption to Ferrihydrite: Application of a Surface Complexation Model." *Geochimica et Cosmochimica Acta* 58(24):5465-5478.

Wedepohl H. 1995. "The Composition of the Continental Crust." *Geochimica Cosmochimica Acta* 59:1217-1239.

Westall JC and H Hohl. 1980. "A Comparison of Electrostatic Models for the Oxide/Solution." *Advances in Colloid and Interface Science* 12(4):265-294.

Wharton MJ, B Atkins, JM Charnock, FR Livens, RAD Pattrick, and D Collison. 2000. "An X-Ray Absorption Spectroscopy Study of the Coprecipitation of Tc and Re with Mackinawite (FeS)." *Applied Geochemistry* 15:347-354.

Wildung RE, RC Routson, RJ Serne, and TR Garland. 1974. "Pertechnetate, Iodide and Methyl Iodide Retention by Surface Soils." In *Pacific Northwest Laboratory Annual Report for 1974 to the USAEC Division of Biomedical and Environmental Research. Part 2. Ecological Sciences*, BE Vaughan (manager), pp. 37-40, BNWL-1950 PT2, Pacific Northwest Laboratories, Richland, Washington.

Wildung RE, KM McFadden, and TR Garland. 1979. "Technetium Sources and Behavior in the Environment." *Journal of Environmental Quality* 8:156-161.

Wildung RE, YA Gorby, KM Krupka, NJ Hess, SW Li, AE Plymale, JP McKinley, and JK Fredrickson. 2000. "Effect of Electron Donor and Solution Chemistry on the Products of the Dissimilatory Reduction of Technetium by *Shewanella putrefaciens*." *Applied and Environmental Microbiology* 66:2452-2460.

Zachara JM, CC Ainsworth, GE Brown, Jr., JG Catalano, JP McKinley, O Qafoku, SC Smith, JE Szecsody, SJ Traina, and JA Warner. 2004. "Chromium Speciation and Mobility in a High Level Nuclear Waste Vadose Zone Plume." *Geochem Cosmochim. Acta* 68(1):13-30.

Appendix

2D μXRD Images and 1D Powder Diffraction Patterns for Unleached and Water-Leached C-106 Residual Sludge
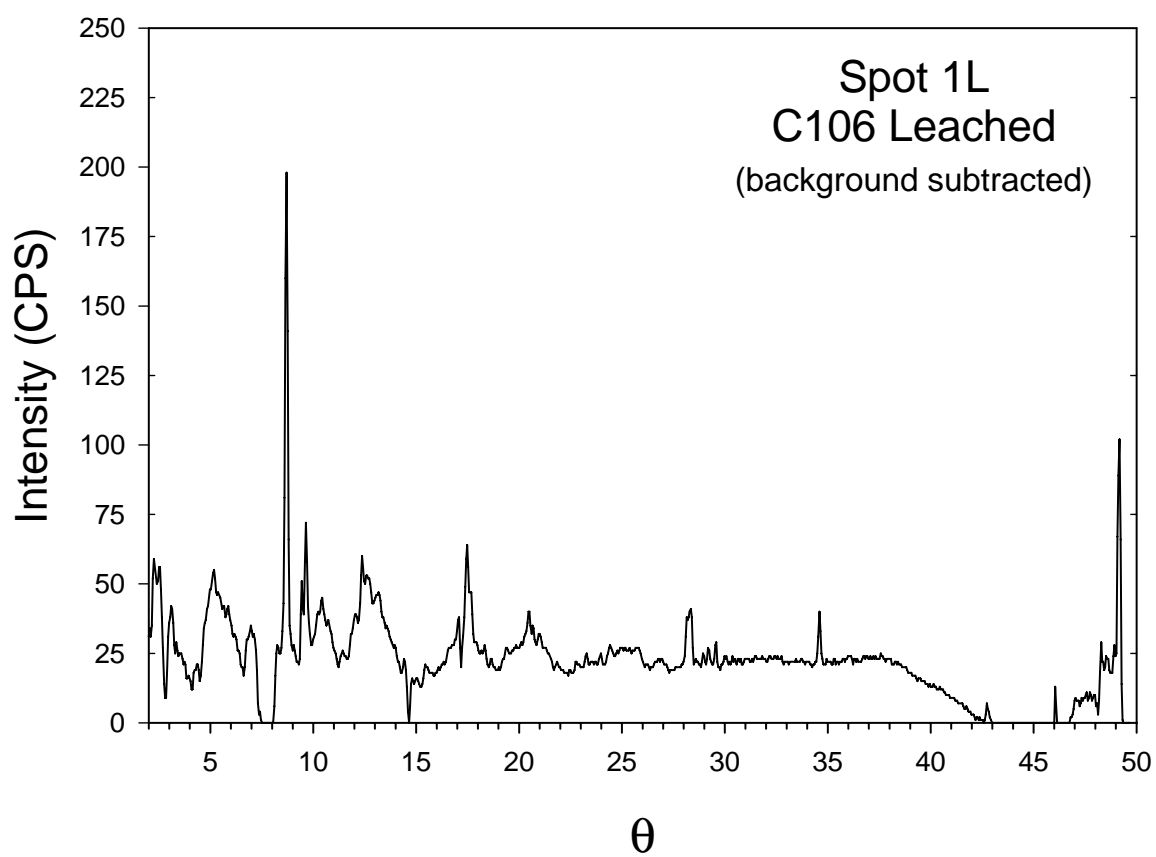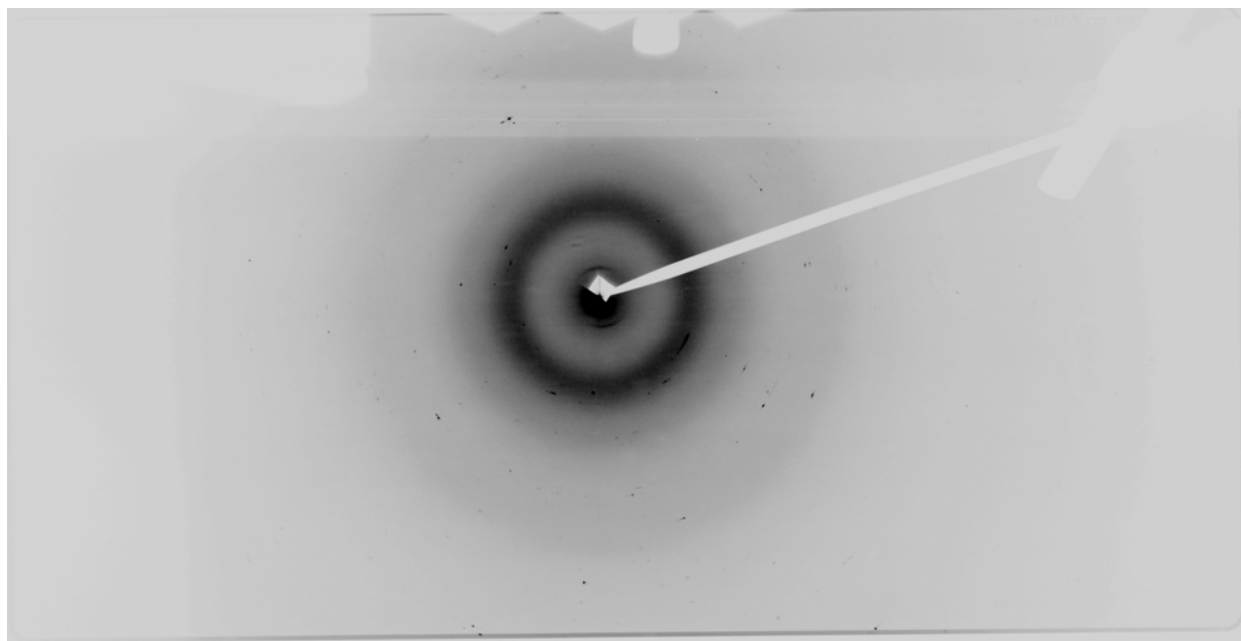
Figure A.1. µXRD 2D image (top) and 1D powder diffraction pattern (bottom) for spot 1L (Figure 33) (incoming wavelength of 0.7293 Å) collected from C106 Leached
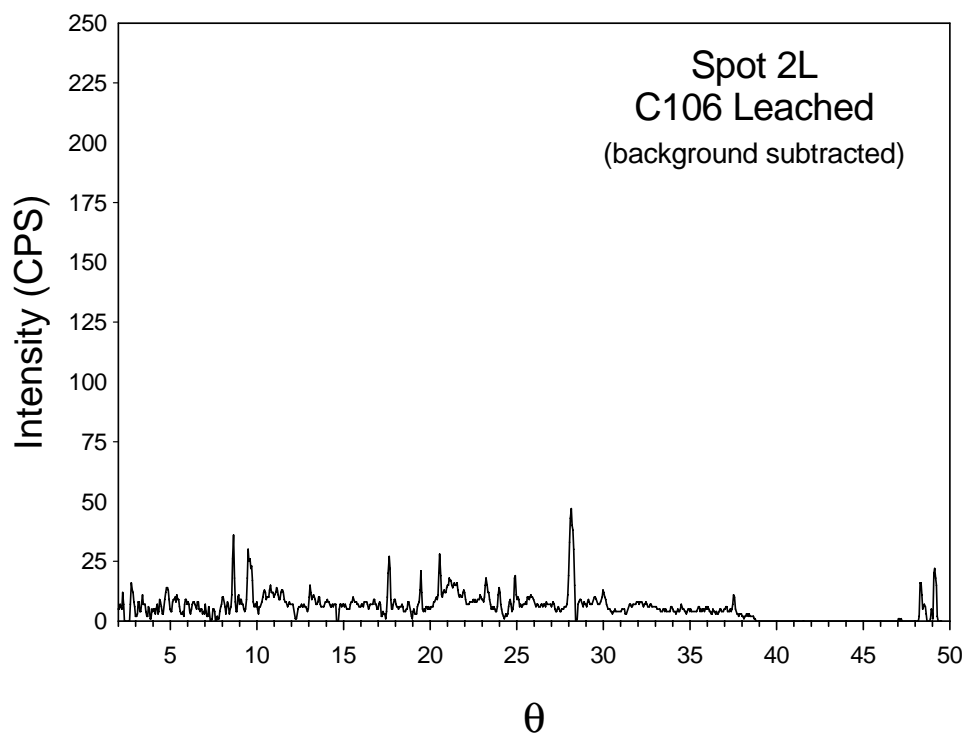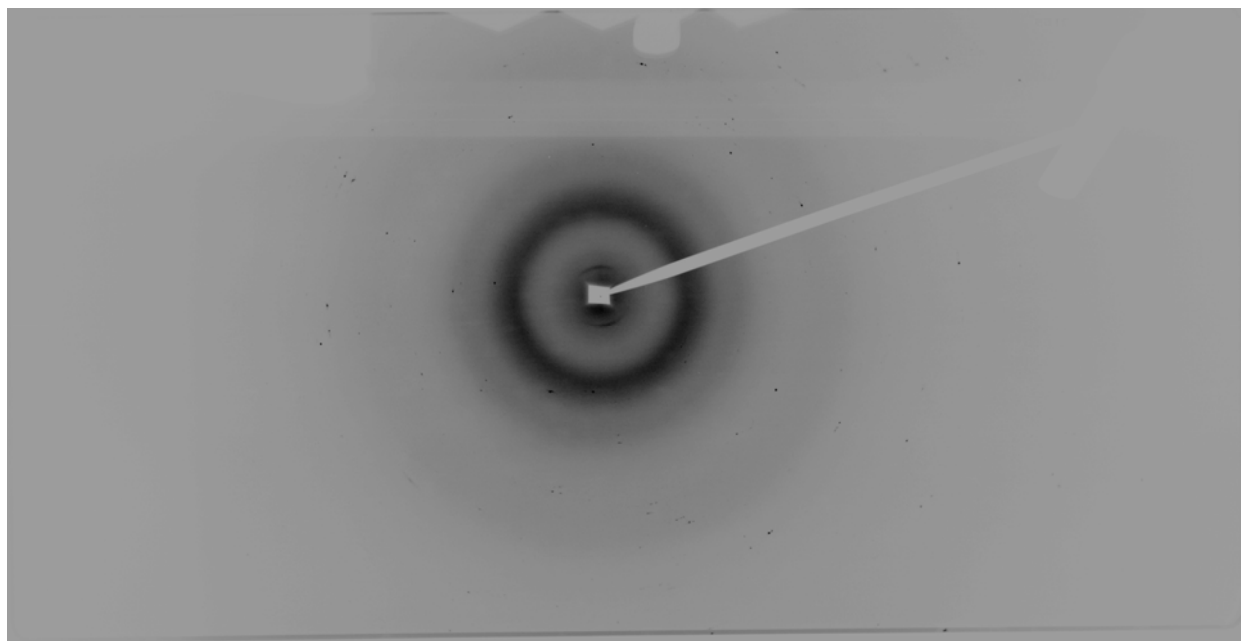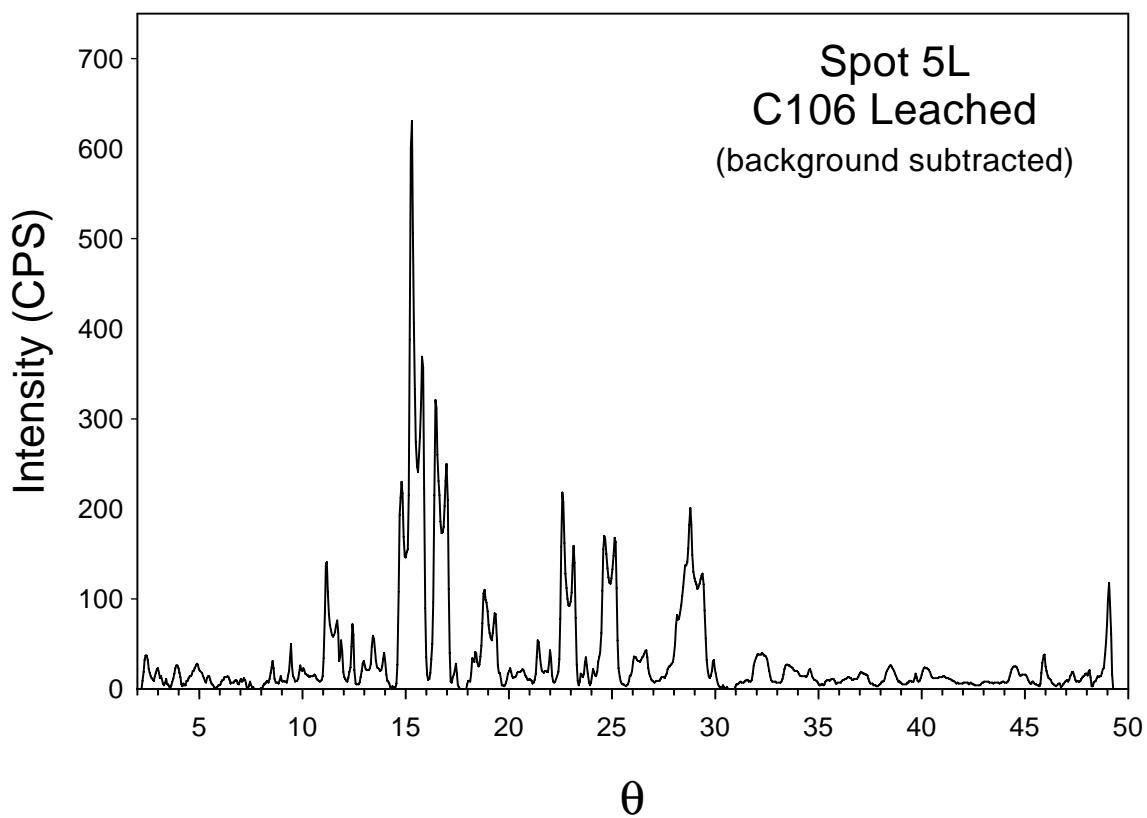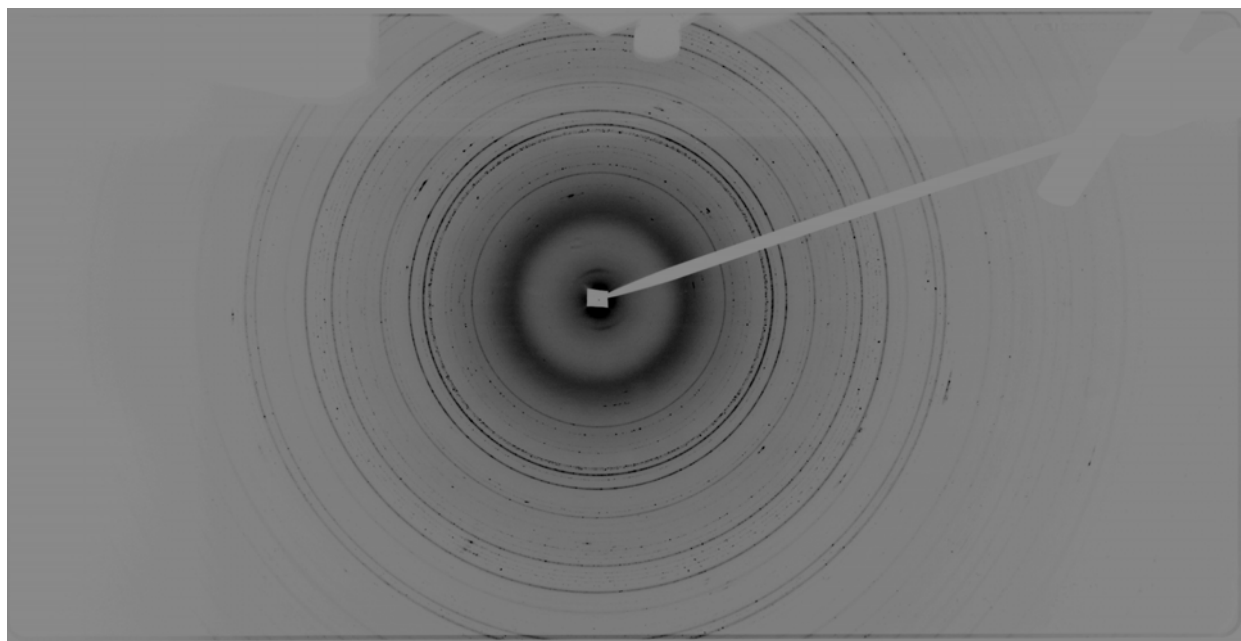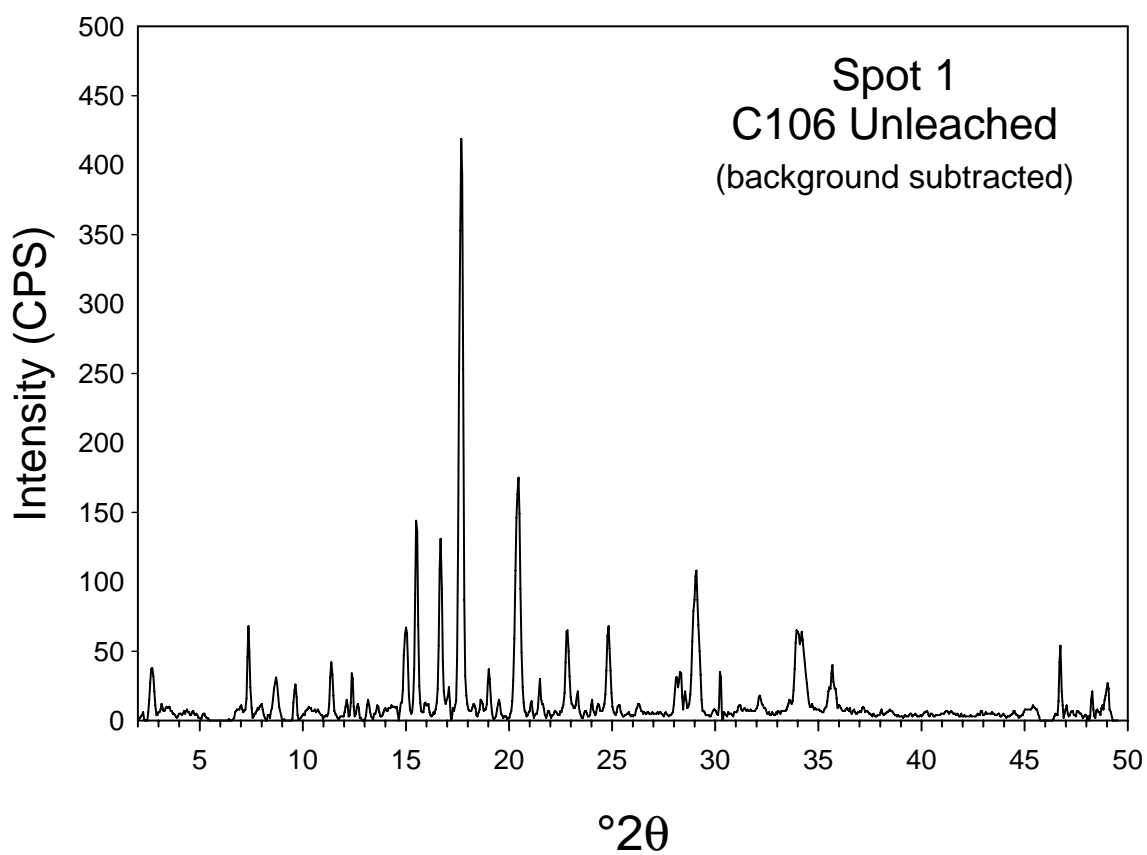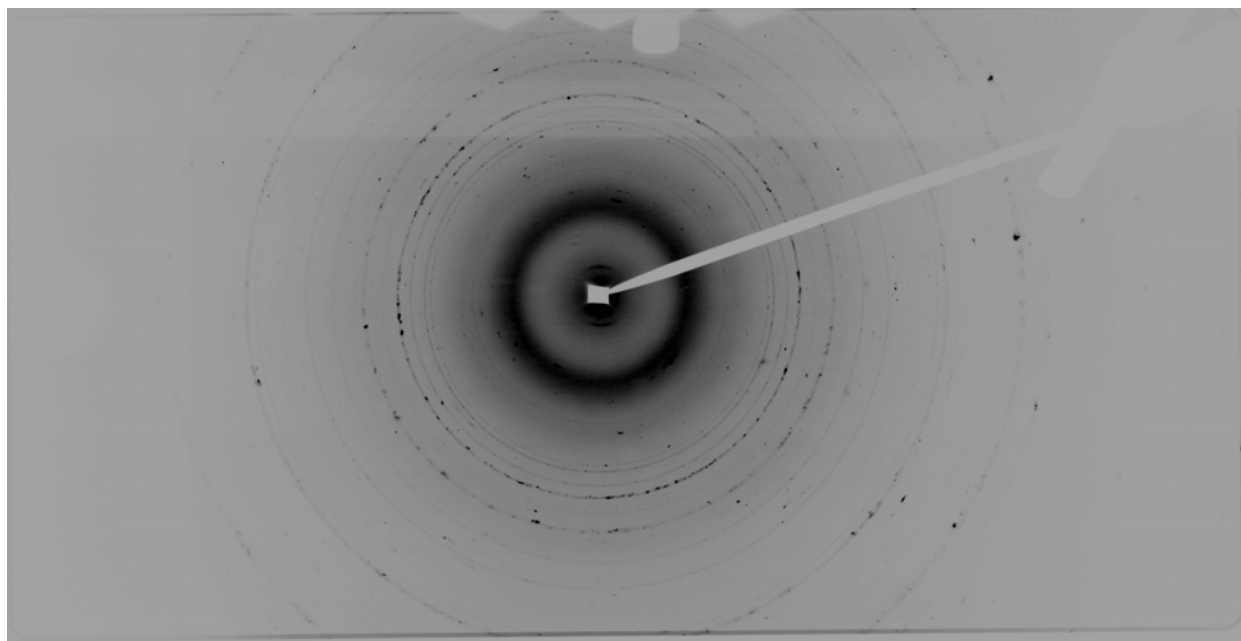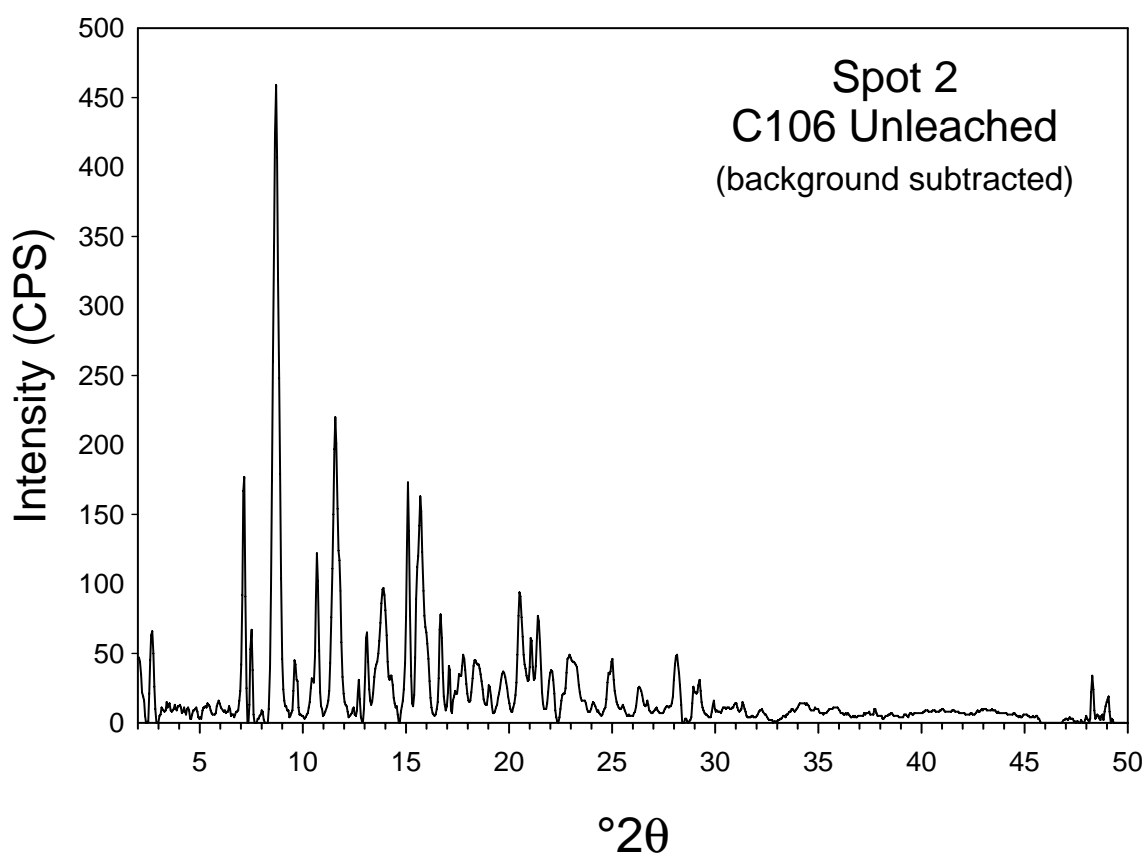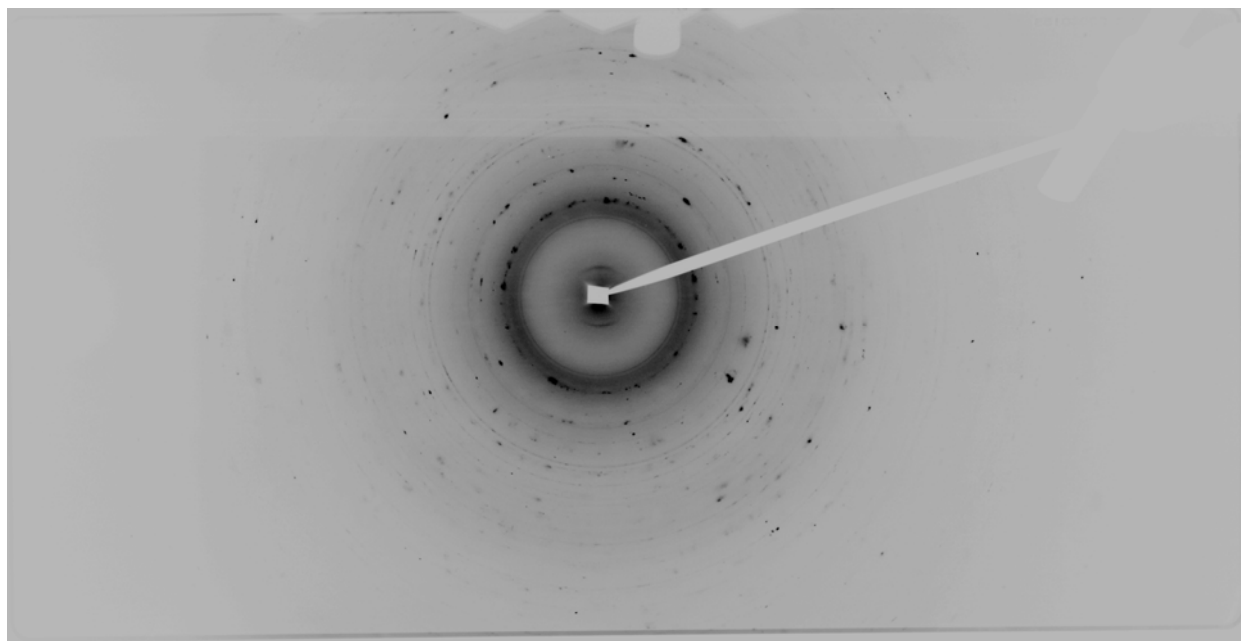
Figure A.2.   µXRD 2D image (top) and 1D powder diffraction pattern (bottom) for spot 2L (Figure 33) (incoming wavelength of 0.7293 Å) collected from C106 Leached
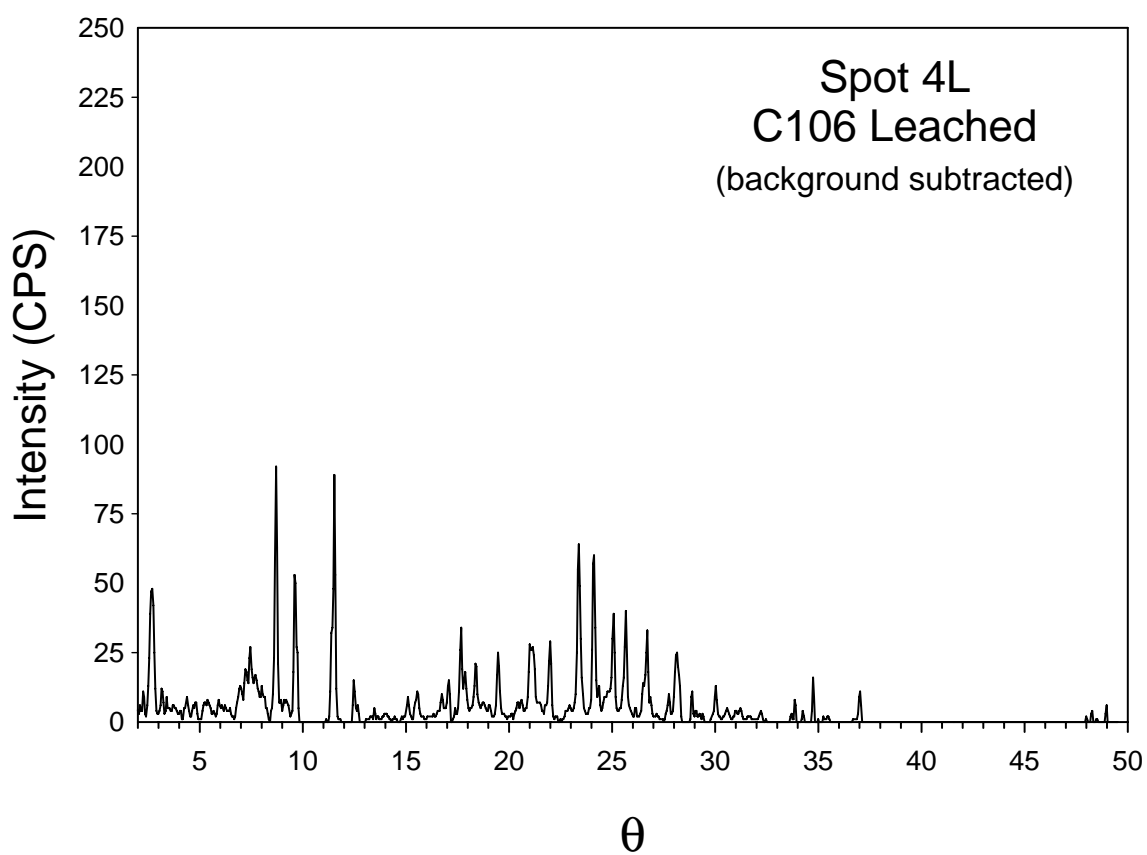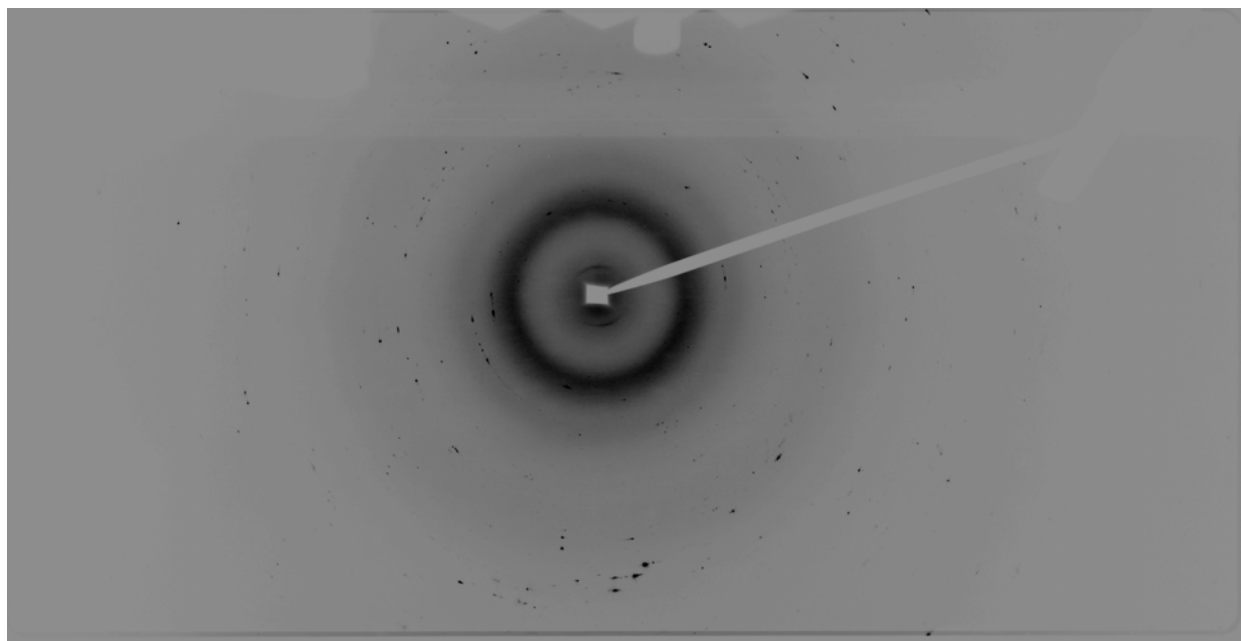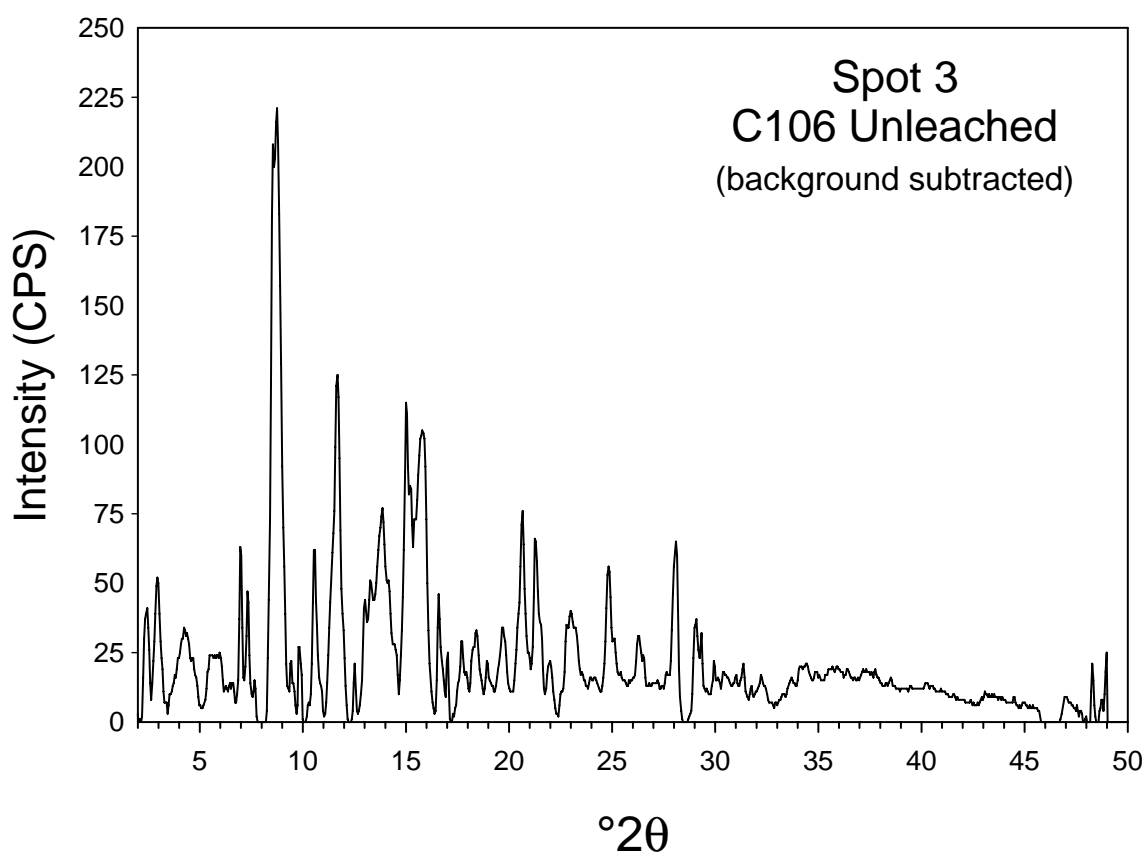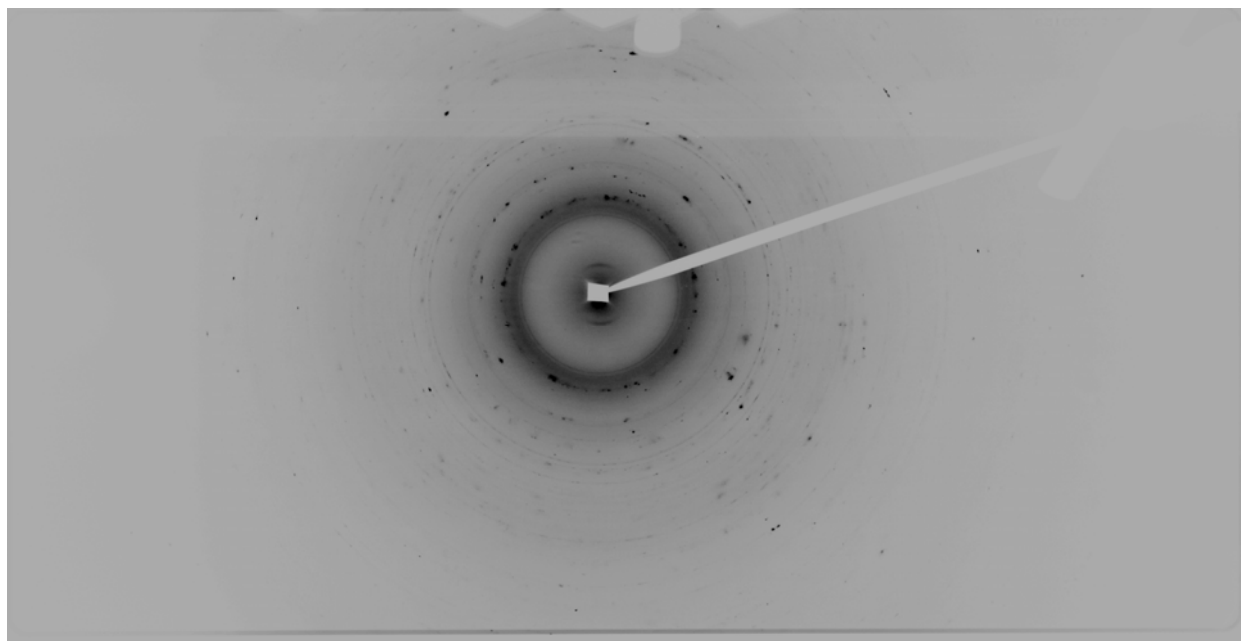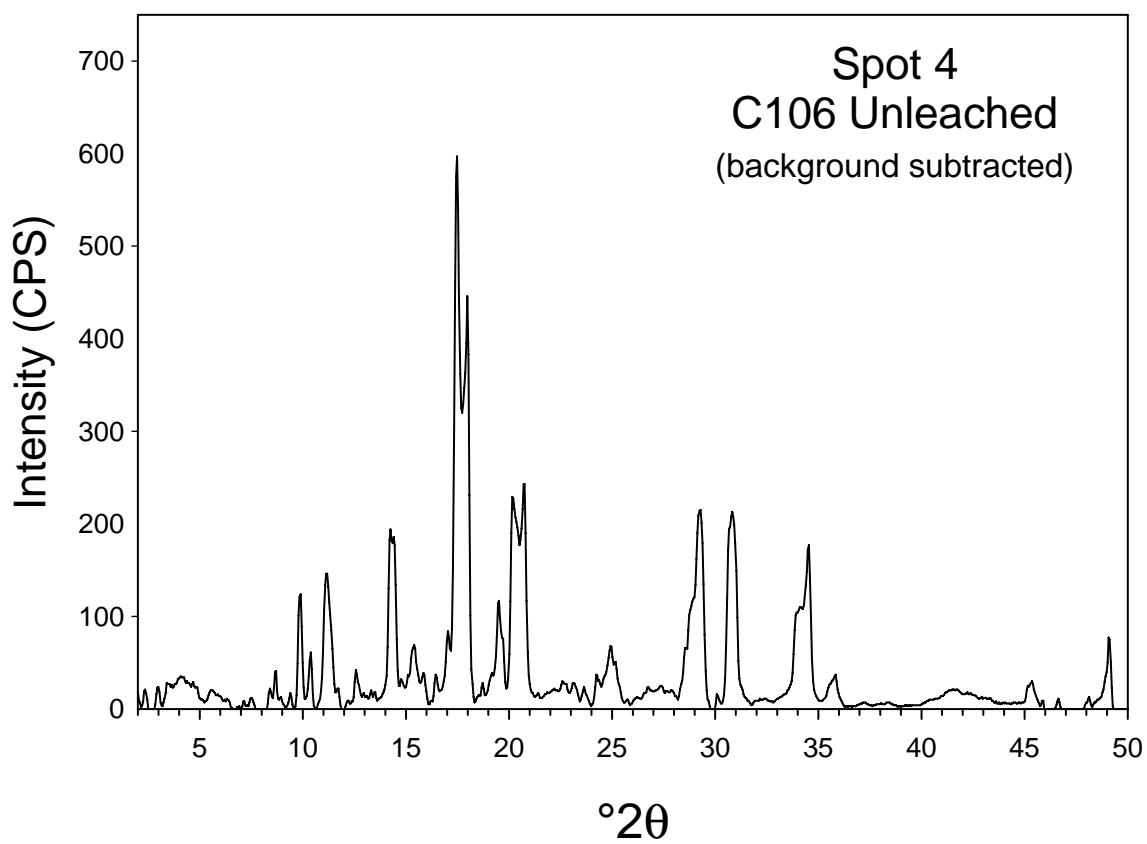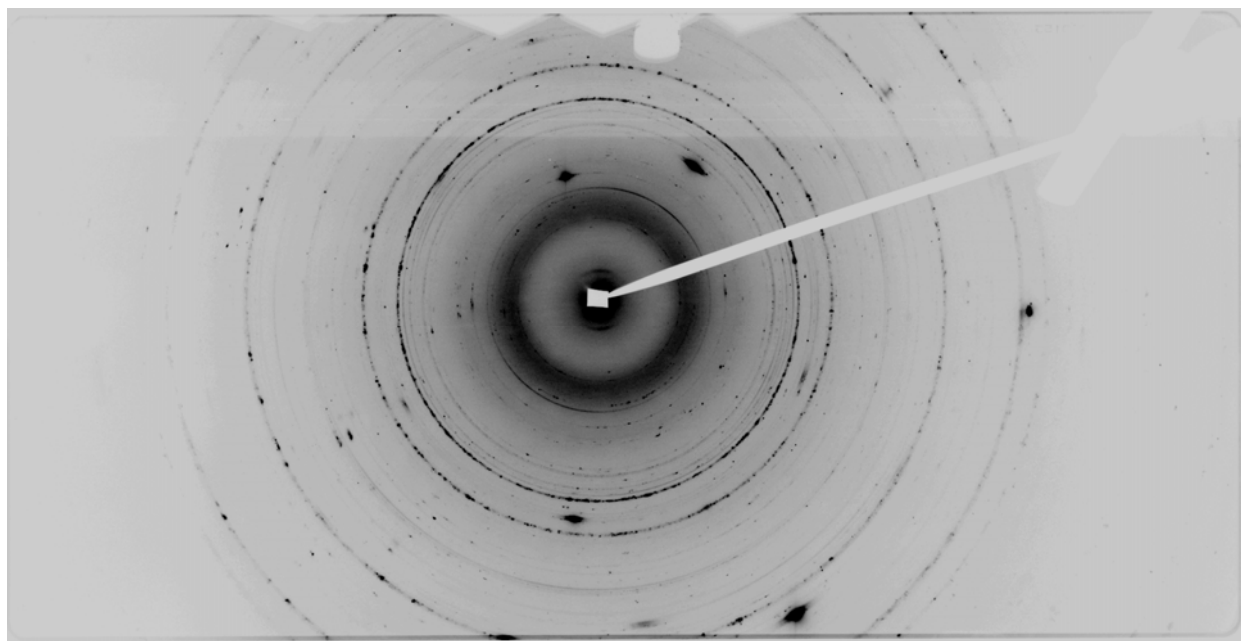
Figure A.3.   µXRD 2D image (top) and 1D powder diffraction pattern (bottom) for spot 4L (Figure 33) (incoming wavelength of 0.7293 Å) collected from C106 Leached

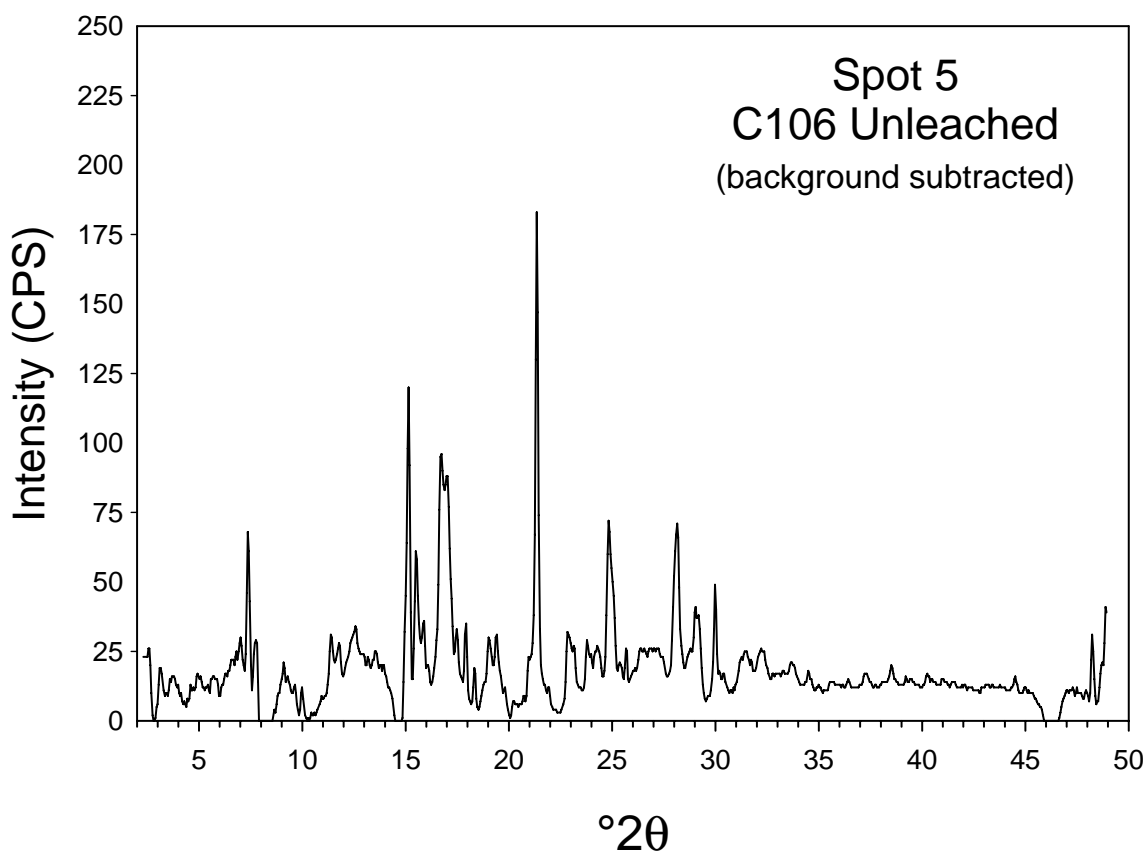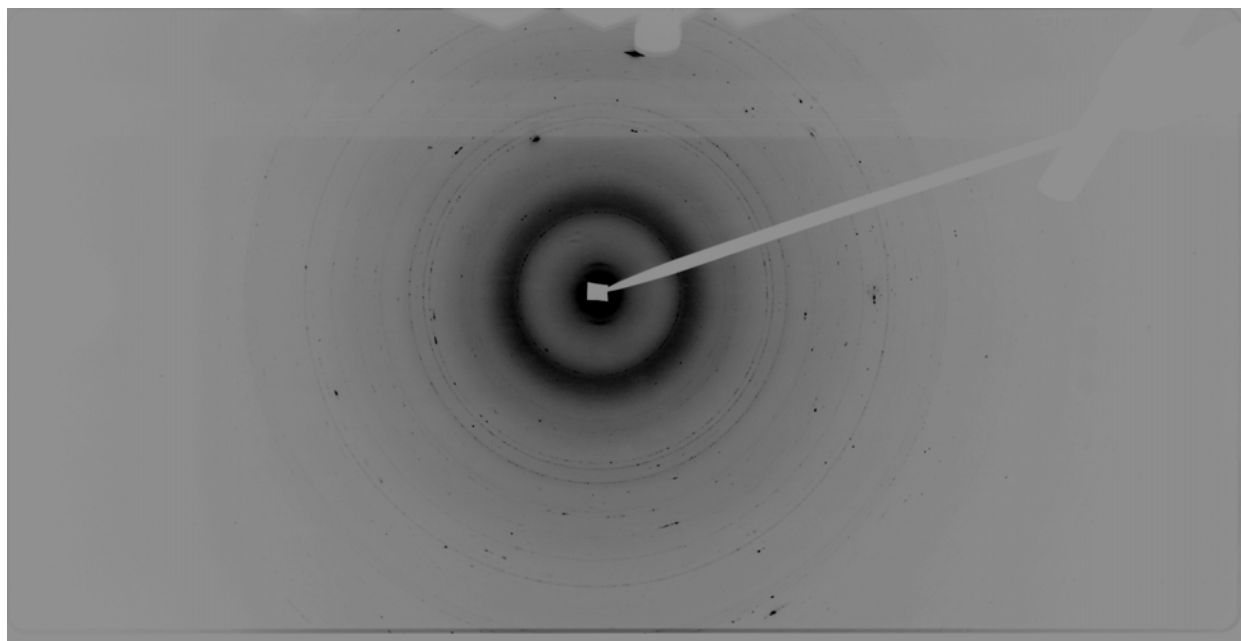**Figure A.4**.   µXRD 2D image (top) and 1D powder diffraction pattern (bottom) for spot 5L (Figure 34) (incoming wavelength of 0.7293 Å) collected from C106 Leached

Figure A.5.   µXRD 2D image (top) and 1D powder diffraction pattern (bottom) for spot 1 (Figure 27) (incoming wavelength of 0.7293 Å) collected from C106 Unleached

Figure A.6.   μXRD 2D image (top) and 1D powder diffraction pattern (bottom) for spot 2 (Figure 27) (incoming wavelength of 0.7293 Å) collected from C106 Unleached
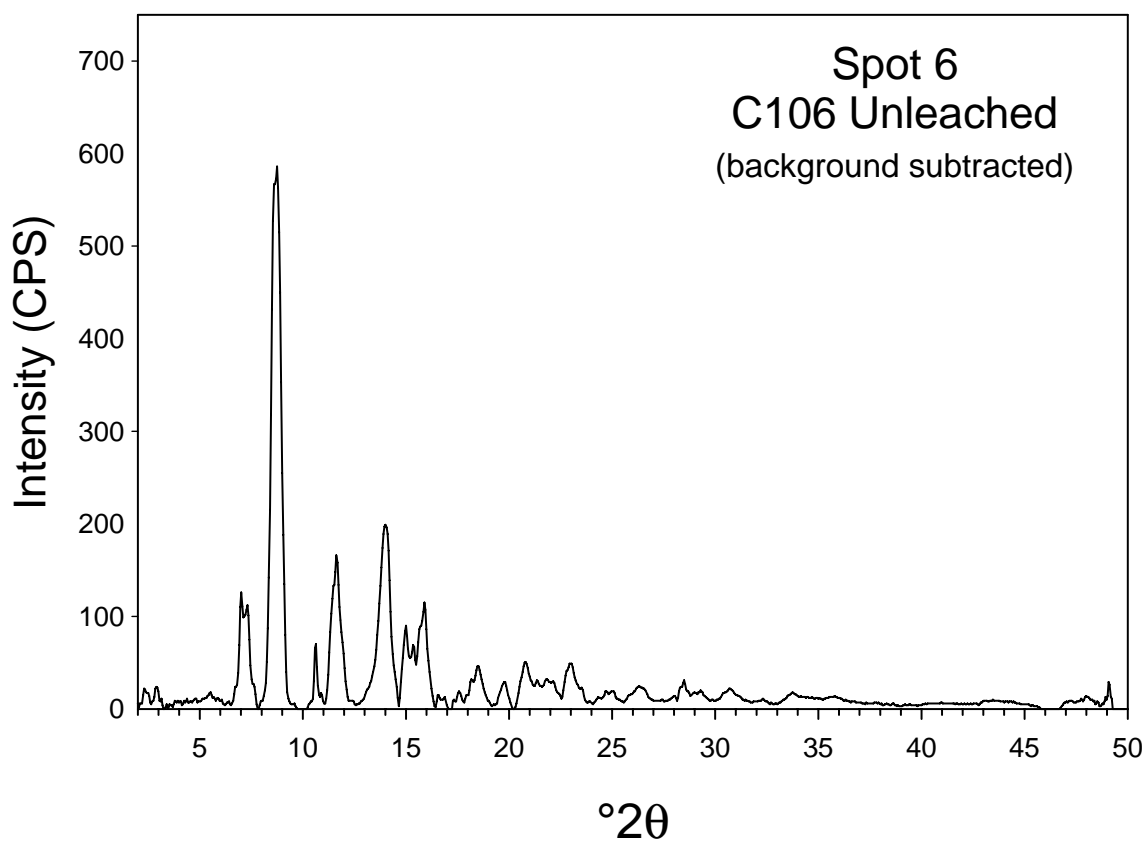
Figure A.7. μXRD 2D image (top) and 1D powder diffraction pattern (bottom) for spot 3 (Figure 27) (incoming wavelength of 0.7293 Å) collected from C106 Unleached
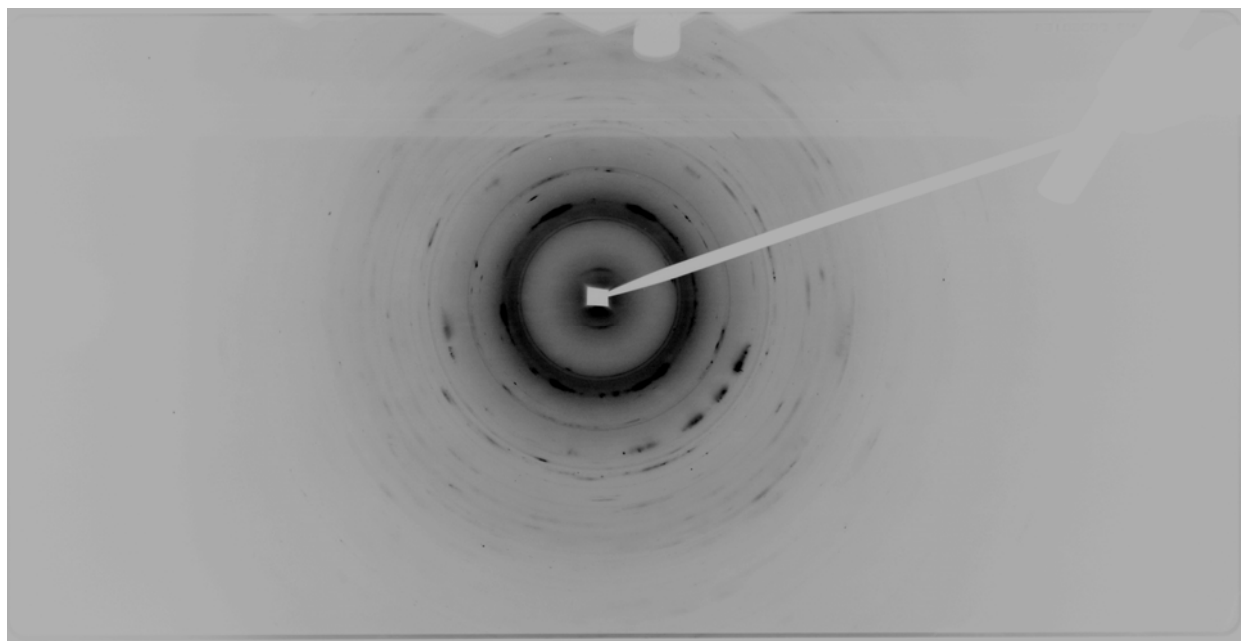
Figure A.8. µXRD 2D image (top) and 1D powder diffraction pattern (bottom) for spot 4 (Figure 27) (incoming wavelength of 0.7293 Å) collected from C106 Unleached

Figure A.9. μXRD 2D image (top) and 1D powder diffraction pattern (bottom) for spot 5 (Figure 28) (incoming wavelength of 0.7293 Å) collected from C106 Unleached

Figure A.10. µXRD 2D image (top) and 1D powder diffraction pattern (bottom) for spot 6 (Figure 28) (incoming wavelength of 0.7293 Å) collected from C106 Unleached
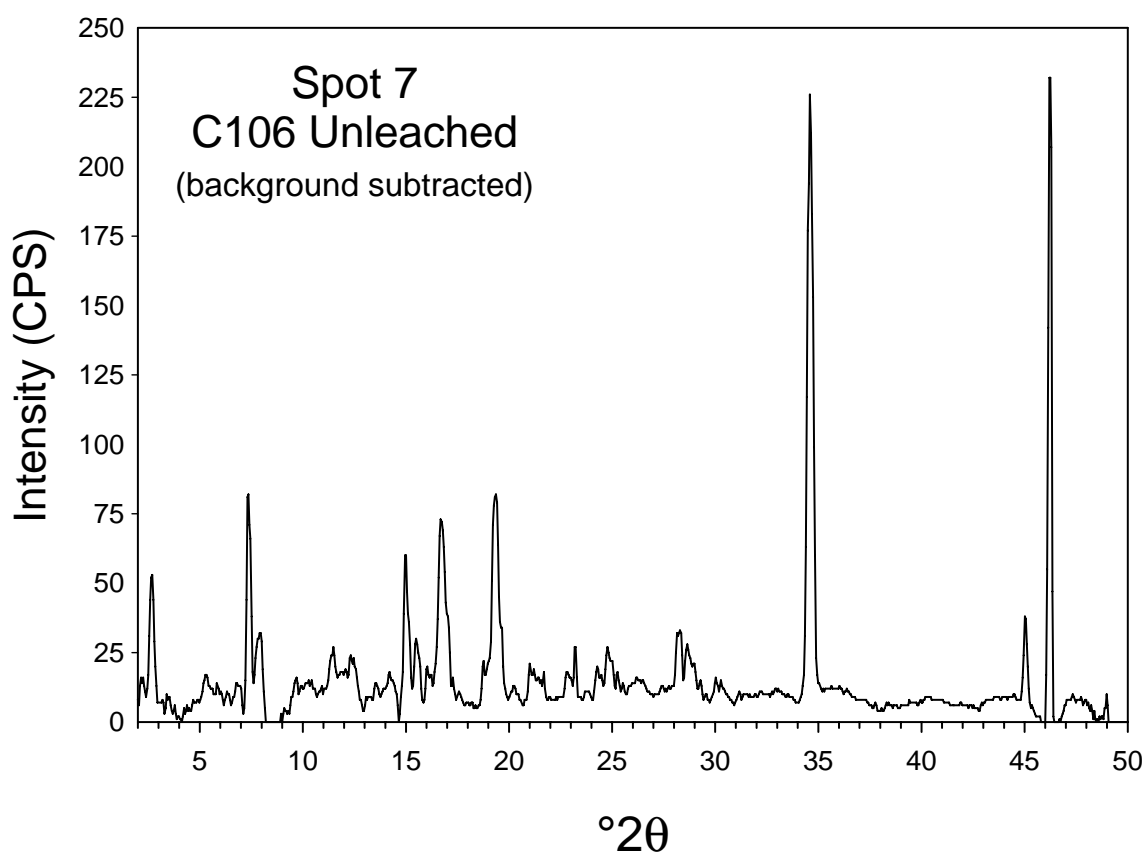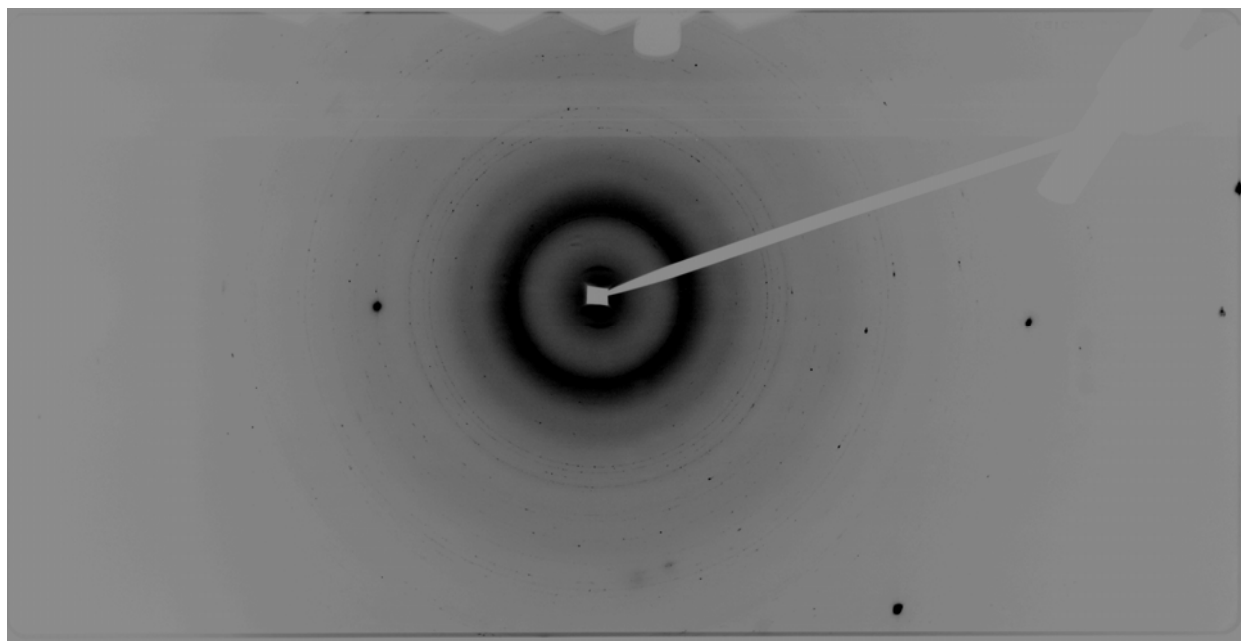
Figure A.11.   μXRD 2D image (top) and 1D powder diffraction pattern (bottom) for spot 7 (Figure 28) (incoming wavelength of 0.7293 Å) collected from C106 Unleached
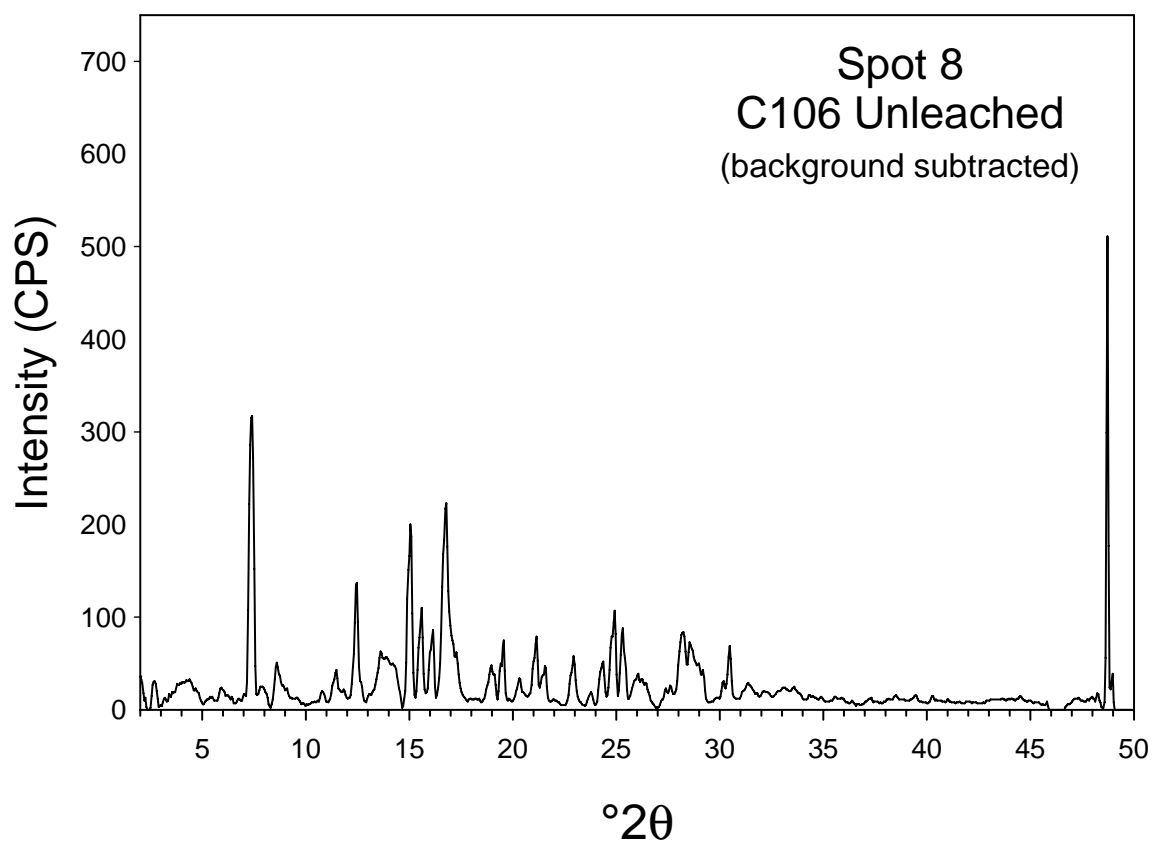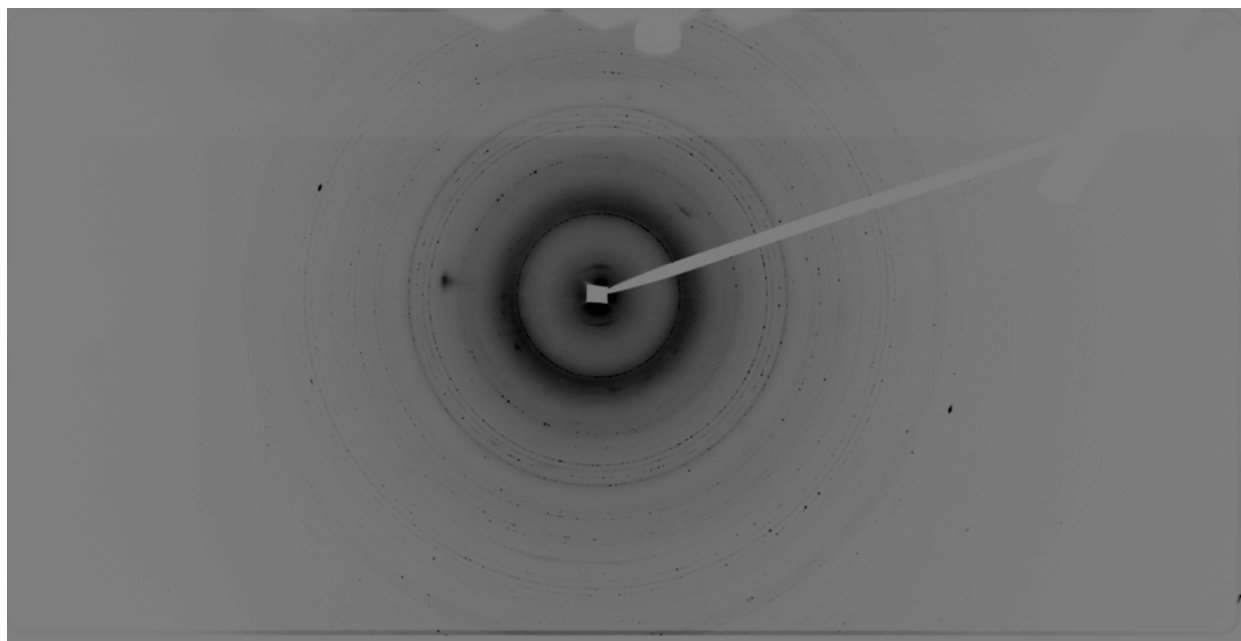
Figure A.12. µXRD 2D image (top) and 1D powder diffraction pattern (bottom) for spot 8 (Figure 29) (incoming wavelength of 0.7293 Å) collected from C106 Unleached

Distribution

No. of
Copies

OFFSITE

Steve Airhart
Freestone Environmental Services
1933 Jadwin Avenue
Richland, WA 99354

Dr. Harry Babad
2540 Cordoba Court
Richland, WA 99352-1609

Pat Brady
Geochemistry Department, 6118
Sandia National Laboratories
P.O. Box 5800
Albuquerque, NM 87185-0750

Charles R. Bryan
Sandia National Laboratories
4100 National Parks Highway
Carlsbad, NM 88220

Susan Carroll
Lawrence Livermore National Laboratory
MS L-219
Livermore, CA 94550

Jon Chorover
Associate Professor – Environmental
  Chemistry
Department of Soil, Water, and
  Environmental Science
Shantz 429, Building #38
University of Arizona
Tucson, AZ 85721-0038

Dave G. Coles
Coles Environmental Consulting
750 South Rosemont Road
West Linn, OR 97068

Mark Conrad
Department of Earth and Planetary Sciences
University of California, Berkeley
Berkeley, CA 94720

Dr. James A. Davis
U.S. Geological Survey
MS 465
345 Middlefield Road
Menlo Park, CA 94025

Donald J. DePaolo
Geology & Geophysics Dept. MC4767
University of California
Berkeley, CA 94720-4767

Dirk A. Dunning
Oregon Office of Energy
625 Mariona Street, N.E.
Salem, OR 97301-3742

Mark Ewanic
MSE Technology Applications, Inc.
200 Technology Way
Butte, MT 59701

Markus Flury
Department of Crop and Soil Sciences
Washington State University
Pullman, WA 99164

No. of
Copies

Amy P. Gamerdinger
2122 E. Hawthorne
Tucson, AZ 85719

Jim Harsh
Department of Crop & Soil Sciences
Washington State University
Johnson Hall, Room 249
Pullman, WA 99164-6420

Dr. Cliff Johnston
Soil Chemistry and Mineralogy
1150 Lily Hall
Purdue University
West Lafayette, IN 47907-1150

Dr. Daniel I. Kaplan
Westinghouse Savannah River Company
Building 774-43A, Room 215
Aiken, SC 29808

Dr. Jim Krumhansl
Sandia National Laboratory
P.O. Box 5800
Albuquerque, NM 87185-0750

Dr. Christine Langston
Westinghouse Savannah River Co.
Building 774-43A
Aiken, SC 29808

Dr. Peter C. Lichtner
Los Alamos National Laboratory
P.O. Box 1663
Los Alamos, NM 87545

Sandra Lilligren
Nez Perce
P.O. Box 365
Lapwai, ID 83540

No. of
Copies

Kate Maher
The Center for Isotope Geochemistry
301 McCone Hall
University of California, Berkeley
Berkeley, CA 94702-4746

Melaine A. Mayes
Environmental Sciences Division
Oak Ridge National Laboratory
P.O. Box 2008
[Bethel Valley Road for FedEX/UPS
  delivery]
Oak Ridge, TN 37831-6038

Dr. Kathryn L. Nagy
Department of Earth and Environmental
  Sciences
University of Illinois at Chicago (MC-186)
845 West Taylor Street
Chicago, IL 60607-7059

Heino Nitsche
Director, Center for Advanced
  Environmental and Nuclear Studies
Lawrence Berkeley National Laboratory
1 Cyclotron Road
MS 70A-1150
Berkeley, CA 94720

Phil Reed
U.S. Nuclear Regulatory Commission
Office of Nuclear Regulatory Research
Division of Systems Analysis and
  Regulatory Effectiveness
Radiation Protection, Env. Risk and Waste
  Management Branch
MS T9-F31
Washington, D.C. 20555-0001

No. of
Copies

Richard J. Reeder
Department of Geosciences
State University of New York at Stony
  Brook
Stony Brook, NY 11794-2100

Al Robinson
68705, E 715 PRNE
Richland, WA 99352

Phil Rogers
13 Mountain Oak
Littleton, CO 80127

Dr. Sherry Samson
Dept. EES
University of Illinois at Chicago (MC-186)
845 West Taylor St.
Chicago, IL 60607-7059

David Shafer
Desert Research Institute
University of Nevada
P.O. Box 19040
Las Vegas, NV 89132-0040

Dawn A. Shaughnessy
Glen T. Seaborg Center
Lawrence Berkeley National Laboratory
1 Cyclotron Road
MS 70A-1150
Berkeley, CA 94720

Doug Sherwood
Rivers Edge Environmental
1616 Riverside Drive
West Richland, WA 99353

No. of
Copies

David K. Shuh
Lawrence Berkeley National Laboratory
1 Cyclotron Road
MS 70A-1150
Berkeley, CA 94720

James "Buck" Sisson
Idaho National Engineering and
  Environmental Laboratory
P.O. Box 1625, MS 2107
Idaho Falls, ID 83415-2107

Carl I. Steefel
Lawrence Livermore National Laboratory
Earth & Environmental Sciences Directorate
MS L-204
P.O. Box 808
Livermore, CA 94551-9900

Dr. Samuel J. Traina, Director
Sierra Nevada Research Institute
University of California, Merced
P.O. Box 2039
Merced, CA 95344

Dan Tyler
Freestone Environmental Services
1933 Jadwin Ave.
Richland, WA 99354

Dr. T. T. Chuck Vandergraaf
Atomic Energy of Canada, Limited
Whiteshell Nuclear Research Establishment
Pinawa, Manitoba ROE 1LO
Canada

Dr. Jiamin Wan
Lawrence Berkeley National Laboratory
1 Cyclotron Road, MS 70-0127A
Berkeley, CA 94720

<table>
<tr><td colspan="2">No. of
<u>Copies</u></td><td colspan="2">No. of
<u>Copies</u></td></tr>
</table>

	Mr. Ronald G. Wilhelm	W. J. McMahon	E6-35
	Office of Radiation and Indoor Air	C. W. Miller	H9-03
	401 M Street, S.W.	D. A. Myers	E6-35
	Mail Code 6603J	D. M. Nguyen	R2-12
	Washington, D.C. 20460	T. L. Sams	H6-05

No. of
Copies

Mr. Ronald G. Wilhelm
Office of Radiation and Indoor Air
401 M Street, S.W.
Mail Code 6603J
Washington, D.C. 20460

W. Alexander Williams
U.S. Department of Energy
Office of Environmental Restoration
EM-33
19901 Germantown Road
Germantown, MD 20874-1290

ONSITE

3 **DOE Office of River Protection**

P. E. LaMont	H6-60
R. W. Lober	H6-60
R. B. Yasek	H6-60

8 **DOE Richland Operations Office**

B. L. Foley	A6-38
J. P. Hanson	A5-13
R. D. Hildebrand	A6-38
K. A. Kapsi	A5-13
J. G. Morse	A6-38
K. M. Thompson	A6-38
DOE Public Reading Room (2)	H2-53

15 **CH2M HILL Hanford Group, Inc.**

M. P. Connelly (5)	E6-35
M. E. Johnson	H6-19
T. E. Jones	E6-35
F. J. Anderson	E6-35
A. J. Knepp	H6-60
F. M. Mann	E6-35

No. of
Copies

W. J. McMahon	E6-35
C. W. Miller	H9-03
D. A. Myers	E6-35
D. M. Nguyen	R2-12
T. L. Sams	H6-05

3 **Duratek Federal Services, Inc., Northwest Operations**

M. G. Gardner	H1-11
K. D. Reynolds	H1-11
D. E. Skoglie	H1-11

3 **Environmental Protection Agency**

N. Ceto	B5-01
D. A. Faulk	B5-01
M. L. Goldstein	B5-01

2 **Fluor Federal Services**

R. Khaleel	E6-17
R. J. Puigh	E6-17

5 **Fluor Hanford, Inc.**

T. W. Fogwell	E6-35
B. H. Ford	E6-35
J. G. Hogan	H1-11
V. G. Johnson	E6-35
M. I. Wood	H8-44

Stoller

R. G. McCain	B2-62

5 **Washington State Department of Ecology**

S. Dahl	H0-57
J. A. Caggiano	H0-57
A. D. Huckaby	H0-57